Seismic Interpretation and Basin Modeling of the Svalbard Margin and Knipovich Ridge

Kjartan Refvik

Master of Science Thesis

Department of Earth Science
University of Bergen

December 2014

Acknowledgements

I am using this opportunity to extend my thanks and gratitude towards those who have supported me during the course of this MSc.

I would like to extend my thanks to my supervisor on this thesis, Professor Rolf Mjelde, for an interesting project, as well as his supervision and helpful insight during my time writing this thesis. With his continuous support and patience, this thesis was completed. A thank you to PhD Trond Kvarven, for his insight regarding the project and area. I am also grateful to Professor Emeritus Atle Austegard, for insights and discussions regarding programming in Matlab and insight into basin modeling.

Thank you to my fellow students and friends I have met over the years.

And finally, to Helene. Your patience, support and encouragement during this time, has meant the world to me.

_____

Bergen, December 2014

Kjartan Refvik

Table of Contents

1   Introduction

The Knipovich Ridge (Fig 1.1) is a 550km long system situated on the seafloor west of Svalbard in the Northern Atlantic Ocean. It is a relatively young divergent boundary and ridge in the Northern Mid-Atlantic Ridge system. It is classified as an ultra-slow spreading ridge (Dick et al., 1993).

In most cases the spreading direction at a divergent boundary is perpendicular to the ridge itself, but at the Knipovich ridge the direction is highly oblique. The bathymetry is also different from other ridge systems. Most ridges are symmetrical over a cross-section perpendicular to the rift axis, but the Knipovich ridge differs also on this point. The western part of the ridge has generally has a much higher relief compared to the eastern side of the rift basin. This could be related to the differences in sediment loading on each side of the ridge. Due to the large input of sediment during the last glacial periods, the sediment load is larger on the eastern flank of the ridge. The goal of this thesis is to interpret multi-channel seismic lines crossing the rift axis and subsequently model basement when the sedimentary units are back-stripped, in order to explore the possible correlation between sedimentary load and lack of symmetry. And, if no correlation is found, explore other solutions to the observations.
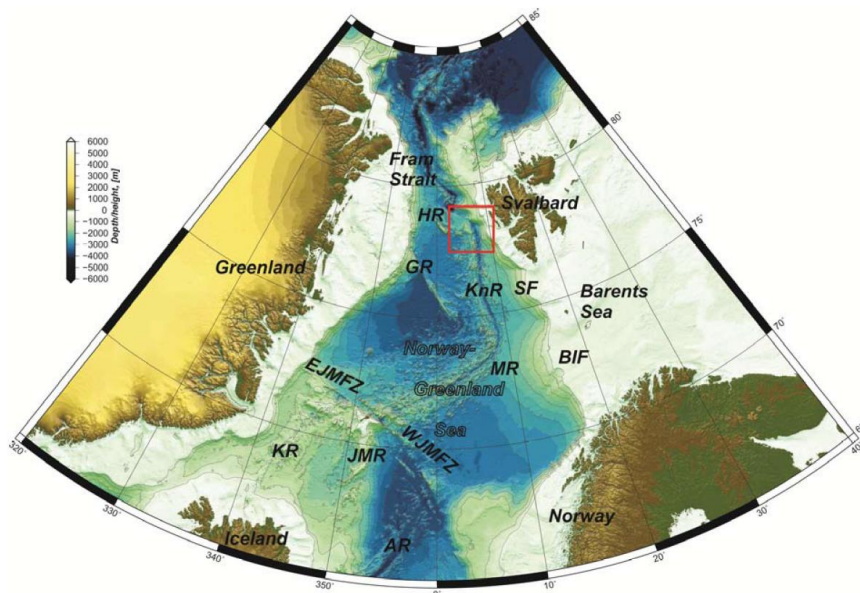

Figure 1.1: The Northern Mid-Atlantic Ridge system with the survey area marked in red. KR=Kolbeinsey Ridge, E/W-JMFZ=Eastern/Western Jan Mayen Fracture Zone, JMR=Jan Mayen Ridge, AR=Aegir Ridge, MR=Mohns Ridge, GR=Greenland Ridge,

2   Spreading Ridges and Geological Background

2.1   Location

The Knipovich Ridge is situated on the Northern Atlantic Ocean seafloor. It is located due west of Svalbard (Fig. 2.1).
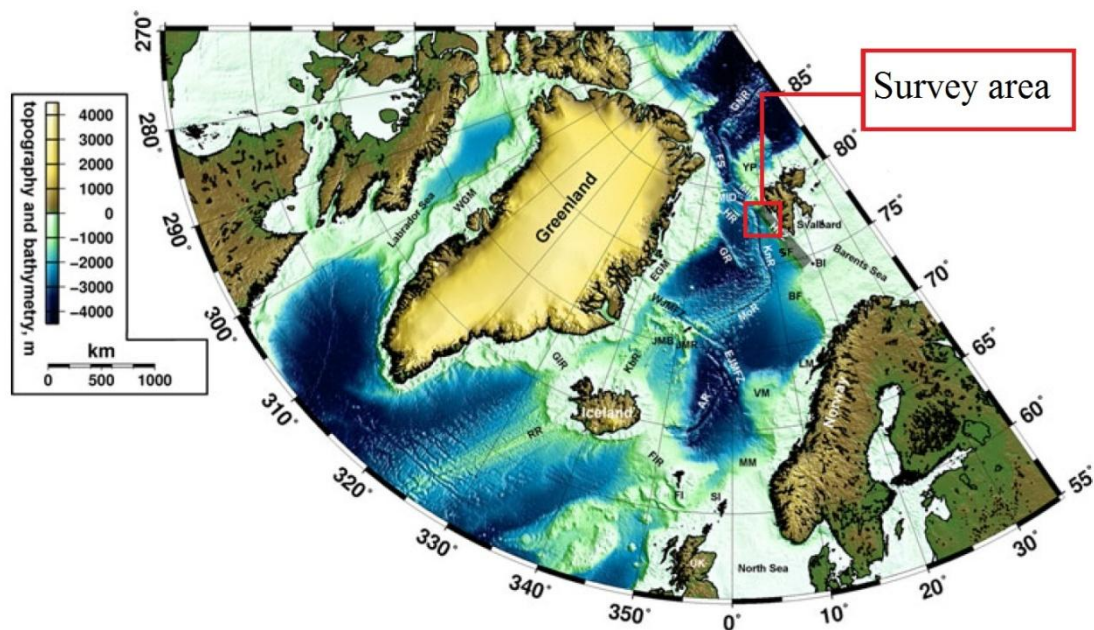
Figure 2.1: Bathymetric map of the Northern Atlantic Ocean showing the Survey Area. RR= Reykjanes Ridge, GIR=Greenland-Iceland Ridge, FIR=Faeroe-Iceland Ridge, FI=Faroe Islands, SI=Shetland Islands, MM=Møre Margin, VM=Vøring Margin, LM=Lofoten Margin, AR=Aegir Ridge, EJMFZ=East Jan Mayen Fracture Zone, WJMFZ=West Jan Mayen Fracture Zone, KbR=Kolbeinsey Ridge, JMB=Jan Mayen Basin, JMR=Jan Mayen Ridge, EGM=East Greenland Margin, WGM=West Greenland Margin, MoR=Mohns Ridge, BF=Bear Island Fan, BI=Bear Island, SF=Storfjorden Fan, GR=Greenland Ridge, HFZ=Hornsund Fault zone, HR=Hovgaard Ridge, KnR=Knipovich Ridge, MlD=Molloy Deep, MlR=Molloy Ridge, FS=Fram Strait, YP=Yeremak Plateu, GNR=Gakkel-Nansen Ridge. (Modified from Kandilarov, 2011).

The Northern Mid-Atlantic Ridge (NMAR) system extends from around 60^ON to 85^ON and consists of both active and extinct ridges. The active ridge system includes the southern Reykjanes Ridge and the Icelandic Hotspot to the Kolbeinsey Ridge, Mohns Ridge,

3

Knipovich Ridge, Molloy Ridge and the northernmost Fram Strait and Gakkel-Nansen Ridge. Several extinct ridges and features are also present in the area, such as the Ægir Ridge and the Spitsbergen and Hornsund Fracture Zones.

The Knipovich Ridge itself is a 550km long part of the NMAR located west of Svalbard. It stretches from 73° 30' N to 78°N, and is oriented straight N-S along a distance of 550 km.

2.2   Plate boundaries and plate tectonics

Plate tectonics in its current form is a fairly new concept within geoscience. Due to the belief that there were no natural forces able to move continents through oceanic crust, and with the lack of precise paleomagnetic measurements, all tectonic changes and continental creation was thought to be of magmatic origin, with continents "plowing" through the oceanic crust. The theory of seafloor spreading did not gain widespread recognition within the scientific community until Harry H. Hess published his paper in 1962 (Hess, 1962). He proposed in essence what today is an accepted theory.

In plate tectonics, three distinct types of plate boundaries are explained. Transcurrent, divergent and convergent. Transcurrent boundaries have a lateral motion with less terrain deformation compared to the other plate boundaries. Convergent plate boundaries either result in plate collision and a later creation of mountain ranges such as the former Caledonian mountain range, or subsea subduction zones and deep trenches of up to 11000 m water depth. The third of the boundaries is the divergent boundary. In the early stages of a divergent boundary, rifting in an existing continental plate occurs (Stanley, 2009). An example of this is present day East Africa and the Rift Valley. As rising magma melts the lower lithosphere and the movement of the astenosphere pulls the two plates apart, rising magma penetrates the now thinning crust. As the magma cools, it expands, further pushing the two plates apart. This continues as a cycle where magma penetrates the crust and cools eventually forming new seafloor. In later stages, the continued cooling of the crust causes subsidence. Over time, the rift is flooded by the sea. As one plate becomes two and the newly created oceanic plate cools and subsides, a new ocean is created.

Plate tectonics is a cycle, so as new crust is created in one location, the opposite happens at convergent boundaries. Older crust sinks or is thrust back into the mantle at

subduction zones, or is otherwise folded and compacted where continental plates collide, resulting in orogenesis.

Although not proven, it is assumed that cyclic motions within the mantle powers and maintains the movement and changes within plate structures according to the theory of Hess (1962), and refined by later studies (e.g. Stanley, 2009). . Hess (1962) proposed that convective cells of viscous mantle material is fueled by the temperature difference between the lithosphere and core boundaries, causing a rotational movement. Rising warm material is cooled as it flows under the lithosphere, before sinking back towards the core as a cooler mass. It is assumed that oceanic ridges form along the border between two cells with an upward flow motion (e.g. Stanley, 2009, Engelder 1993).

2.3   Spreading ridges

Unless rendered inactive, a divergent boundary will slowly transition from rifting to a seafloor spreading ridge. Over millennia, smaller bays and gulfs such as the Red Sea rift (with spreading rate 9,7mm/yr) may transform into large oceanic basins (DeMets et al., 2010). While small at first, the Atlantic Ocean once was non-existent and landmasses on opposite sides were joined as one (Marshak, 2005). As the rifting continues the continental crust will eventually break, and the process of oceanic crustal accretion will commence. This process will build subsea mountains on either side of the rift valley itself. This structure is called a mid-oceanic ridge or a spreading ridge. Several ten thousand kilometers of these ridges exist at present day on the seafloor.
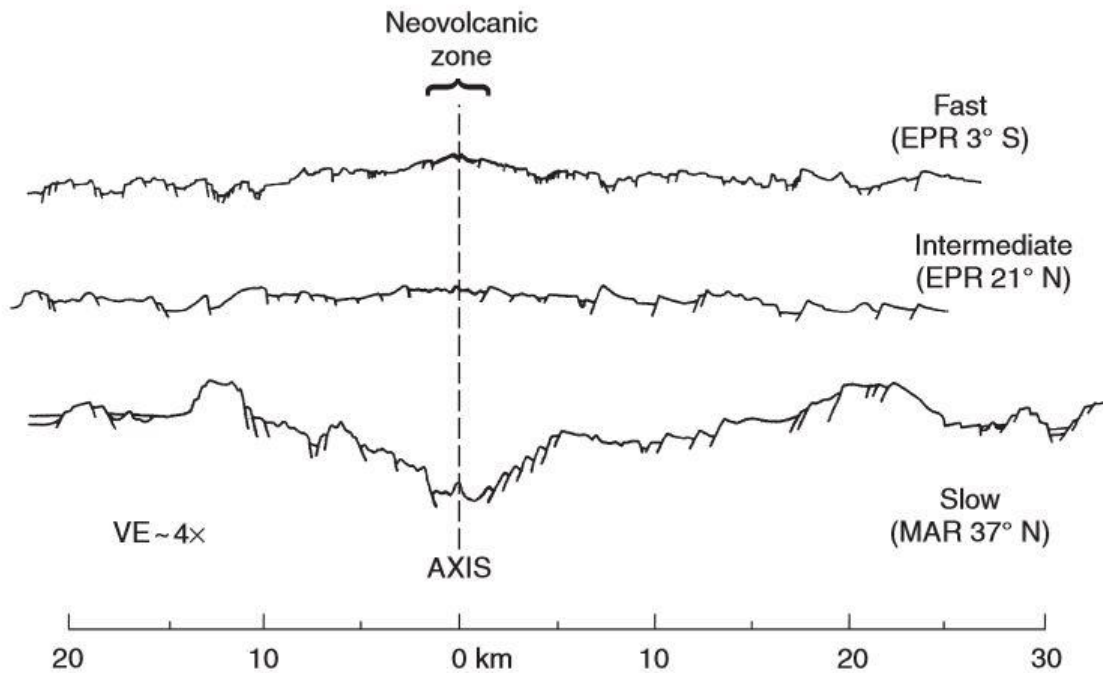
Figure 2.2: Ridge geometry (MacDonald 2001). EPR= East Pacific Rise, MAR=Mid-Atlatntic Ridge

However, there are differences between these ridges (Fig. 2.2). One of the most notable is the speed of spreading. The speed ranges from almost zero on the Gakkel ridge, to 5 cmyr^{-1} on the South-Atlantic ridge and ranging up to 15 cmyr^{-1} for the Pacific-Nazca plate (DeMets et al., 2010). The ridges are typically classified according to the speed of spreading. Dick et al. (2003) divides them into slow (<55 mmyr^{-1}), intermediate (55-70 mmyr^{-1}) and fast (70-180 mmyr^{-1}). Fast spreading ridges typically have a low relief with some small changes in topography, typically less than 400m (Fig. 2.2). The rift valley itself is not pronounced in height, and is also narrow, ranging in the few tens of kilometers. Slow spreading ridges, such as the Mid-Atlantic ridge, is a contrast to the flat and relatively low-relief of fast spreading ridges. These subsea mountains have a strongly varying relief from 400 to 2500m and the width of the rift itself is up to 40 km (MacDonald, 2001).

Observations reveal that mid-oceanic ridges are segmented by numerous discontinuities (MacDonald, 2001). This implies that the spreading axis is distorted and warped from a straight axial spreading line. These discontinuities seem to occur at local maxima along the axial depth profile of the spreading ridge (Fig 2.3). These segmentations are split in four tiers. First order segments are large transform faults or transcurrent boundaries. They are in the order of 300+ km in segment length and have a longevity in the range of millions of years or more. They are by far the most prominent of the segmentations,

6

as they are easily visible on bathymetric maps. Second order segments are smaller in size, up to around 300 km in length and have a smaller longevity compared to first order segments. They exist within the first order segments. They are typically overlapping spreading centers, and while not as prominent on bathymetric maps, they are visible as local areas with increased depth along the spreading axis. Third order segments are similar to second order segments, but has no off-axis trace. They are in the order of some tens of kilometers in length, and have less than 2 km in offset. Fourth order segments are the smallest defined at present date, and have lengths under 50 km and an offset of < 0,5 km. These rarely cause notable axial depth anomalies (MacDonald, 2001).
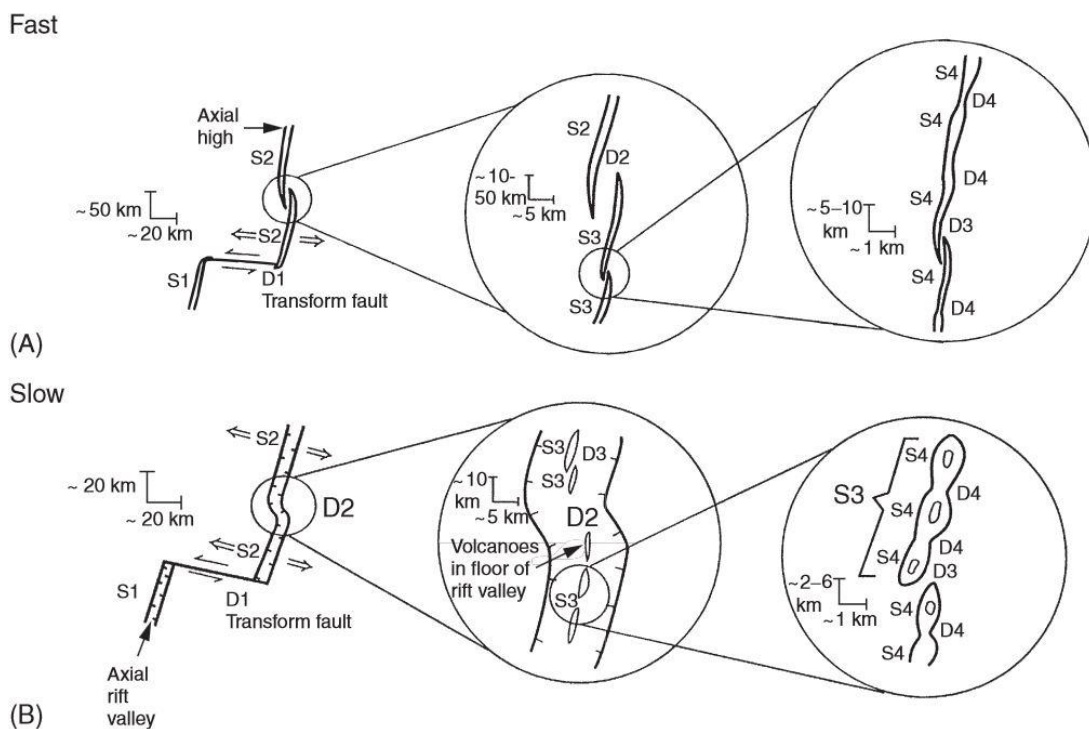
Figure 2.3: Spreading ridge internal segmentation. *D* notes discontinuities in order from 1-4, and *S* notes segmentation in order from 1-4. Both from larger to smaller (MacDonald 2001).

2.4   Oceanic crust

Studies of drill cores and ophiolites, sections of oceanic crust emplaced on land, show that oceanic crust has, when simplified in a model, several distinct sections. The commonly used model is named the Penrose Model, and has four distinct layers; 1, 2a, 2b and 3 in

succession from the seafloor downwards (fig. 2.4). Layer 1 consists of sediments, which are thickness, age and composition dependant on input sources, location and depth. Layers 2a and 2b are of magmatic origin (Dick et al., 2006). 2a consists of pillow basalt, created from extrusion of magma into seawater. Layer 2b is a segment of sheeted basaltic dikes and segment 3a consists of massive gabbro. The lowermost layer 3b is of crystalline origin, and consists of a cumulate of mafic rocks that first crystallized and settled on the bottom of the magma chamber (Van Der Plujim, Marshak, 2004).
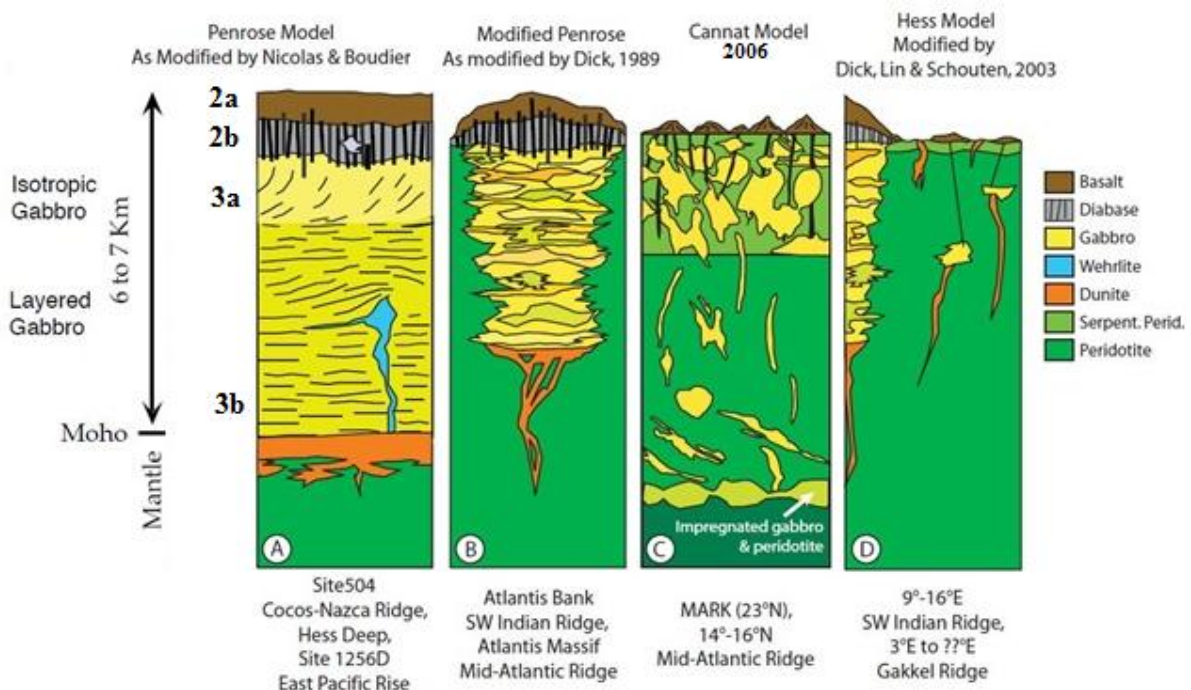
Figure 2.4: Differences in oceanic crust models (Modified from Dick et al., 2006).

This is, however, a simplified model, as confirmed by several ocean drilling programs such as ODP, DODP and IODP. However, these programs also confirmed the simplified validity of the Penrose Model for fast or super fast spreading ridges, such as the East Pacific Rise (EPR). After the transition to drilling in slow and ultraslow spreading ridges was conducted, the Penrose model no longer fit the results produced from the surveys. Cannat (2006) proposed an revised model (fig. 2.4) for slow and ultra-slow spreading ridges and relations to core complexes. The morphology of oceanic crust depend on several factors such as structure and thickness variations with spreading speed, hot spot proximity, ridge geometry

and mantle temperature and composition (Dick et al. 2006). Gabbro is a fundamental building block in the Penrose Model, but is found in varying abundance in other ocean-crust models, having a minor to negligible role (Dick et al. 2006). Below the oceanic crust is the mantle, and this distinct change in regime generally corresponds to the Moho. It is possible to find this transition on seismic images if the penetration depth is high, e.g. if refraction seismic is used. If a profile perpendicular to the axis of a spreading ridge is viewed, the crustal depth profile appears to be symmetrical with the axis as the reflective midpoint, and the rift flanks as bathymetrical profile highs. This is due to the progressive cooling of the crust. As the temperature drops, the density increases, causing the crust to sink slightly. Large underwater plains of cooled oceanic crust are known as abyssal plains. These pelagic sediment covered plains, with depth range 3-5 km, are the topographically most stable areas on Earth.

Oceanic crustal seismic thickness does not seem to depend on the spreading rate above about 20 mmyr^{-1}. Below that threshold it drops significantly, from the 6-7 km norm to 2-4 km in thickness (Dick et al. 2003).

2.5   Ultraslow spreading ridges

Dick et al. (2003) have proposed another classification of spreading ridge in terms of spreading rate. The class of ultraslow-spreading ridges is added, with a spreading rate of less than 12mmyr^{-1}. It is debated if spreading ridges with a spreading rate of up to 20 mmyr^{-1} should be included in this definition, as some share distinct features with the slowest spreading ridges, depending on mantle temperature and composition. Around 20.000 km of the global ridge system fall under this classification, around one third of the global total. Ultraslow spreading ridges are distinct from slow spreading ridges as there is a lack of transform faults separating the segments, as well as the occurrence of exhumed mantle in some areas (Dick et al. 2003).

These ultraslow-spreading segments consist of alternating magmatic and amagmatic accretionary ridge segments. Magmatic segments are second order segments linked together between first order segments; transform faults (MacDonald et al. 1993). These first order segments are not found at ultraslow spreading ridges. Magmatic segments are vital to understanding the regional morphology and spreading speed of mid-oceanic ridges.

Remnant magnetic directionality is locked in place as the magma cools to temperatures below the Curie-temperature, and large segments with the same directionality and strength can be defined to be of the same age. These segments are divided into numerous "Chrons", each with a specific age and traceable location. Magmatic segments form perpendicular to the least principal compressive stress within the rift valley and orthogonal to the spreading direction. They will morphologically consist of axial lows and highs in a linear fashion and express saddle points at the rift valley walls and segment centers, separated by successive normal faults. In the absence of transform faults these structures occur as sets of overlapping en echelon or non-transform discontinuities (Dick et al. 2003).

The amagmatic segments are of unknown origin, but assumptions have been made by e.g. Michael et al. (2003) and Dick et al. (2003). Amagmatic segments up to 80 km long replace the normally occurring magmatic segments and transform faulting. Faulting at these amagmatic segments exposes the crust, with a composition of mainly massive serpentinized peridotite. A thin or absent layer of volcanic origin was at times found. These amagmatic segments can assume any angle to the direction of spreading and link to the magmatic segments. Together they form the plate boundary (Dick et al. 2006). Serpentinized peridotite as amagmatic segments is thought by Michael et al. (2003) to be the mantle itself. As peridotite from the upper mantle is serpentinized by seawater propagating through fissures, faults and cracks in the crust, it is thrust upward and fills in the space created by the diverging plates.

2.6   The Knipovich Ridge

The Knipovich Ridge and surrounding basins, as well as the continental slope towards Svalbard, is the focus of this study. The ridge itself originates from the further northward propagation of the Mohns Ridge around chron 13, early Oligocene, at about 35 Ma. The relative plate motion changed at that time to a more east-westerly trend, causing the opening of the Greenland Sea. This occurred first as continental extension and rifting with a later transition to seafloor spreading along the Knipovich Ridge (Mosar et al. 2002).

Dick et al. (1993) explains:

"The Knipovich Ridge is a ~550 km long supersegment trending 41° to 55° from the spreading direction. The average ESRs (Effective Spreading Rate) of 11.2 and 12.3 $mmyr^{-1}$ in the north and south respectively, fall at or below the ultraslow-spreading ESR threshold at 16° E on the South-west Indian Ocean Ridge (SWIR). This supersegment contains no transforms"

Bathymetric data yield depths of over 3800 m in the center of the ridge valley, with ridge walls depths of around 1800m (Amundsen et al. 2011). While the western edge of the Ridge is situated close to the Greenland Basin, the northern parts of the ridge are situated close to the continental margin of Svalbard. As a consequence, the western ridge wall is a subsea seamount, while the eastern wall is covered by sediments, and the subsea topography shows an inclined slope upwards towards the continental margin of Svalbard. These sediments are massive in thickness and most are of glacial origin.
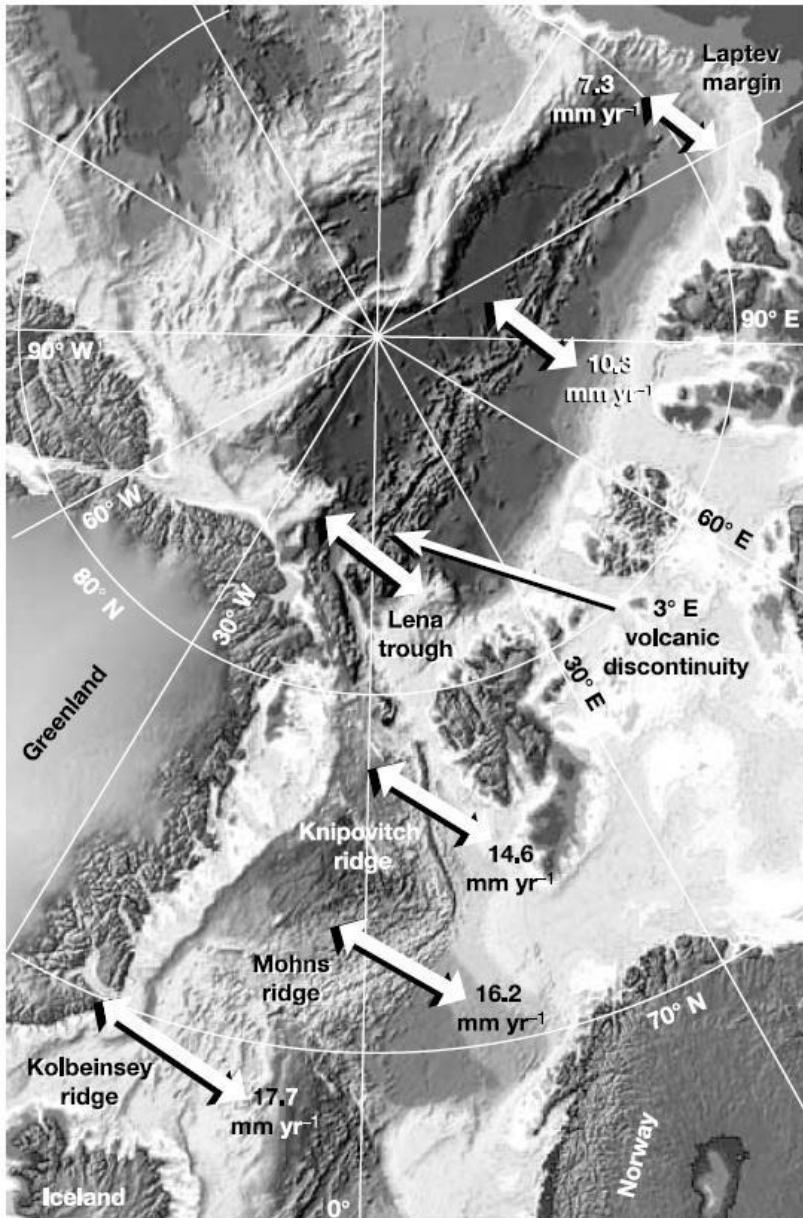
Figure 2.5: Bathymetric map of the North Atlantic Ridge with average spreading rates (Dick et al., 2003)

The spreading direction of the Knipovich Ridge (fig 2.5) is highly oblique to the rift axis itself. With an axis trending more or less directly in the N-S direction, the NNW-SSE spreading direction is far from the normally assumed W-E trend. Full spreading rates at present date are estimated in the north and south at 11.2 and 12.3 mmyr^{-1}, respectively (Dick et al. 1993). As the magnetic anomalies generated around the Knipovich Ridge are diffuse, it is difficult to make precise rate estimates. Engen et al. (2003) relates this to sediment loading and high heat flow.

2.7   Geological History
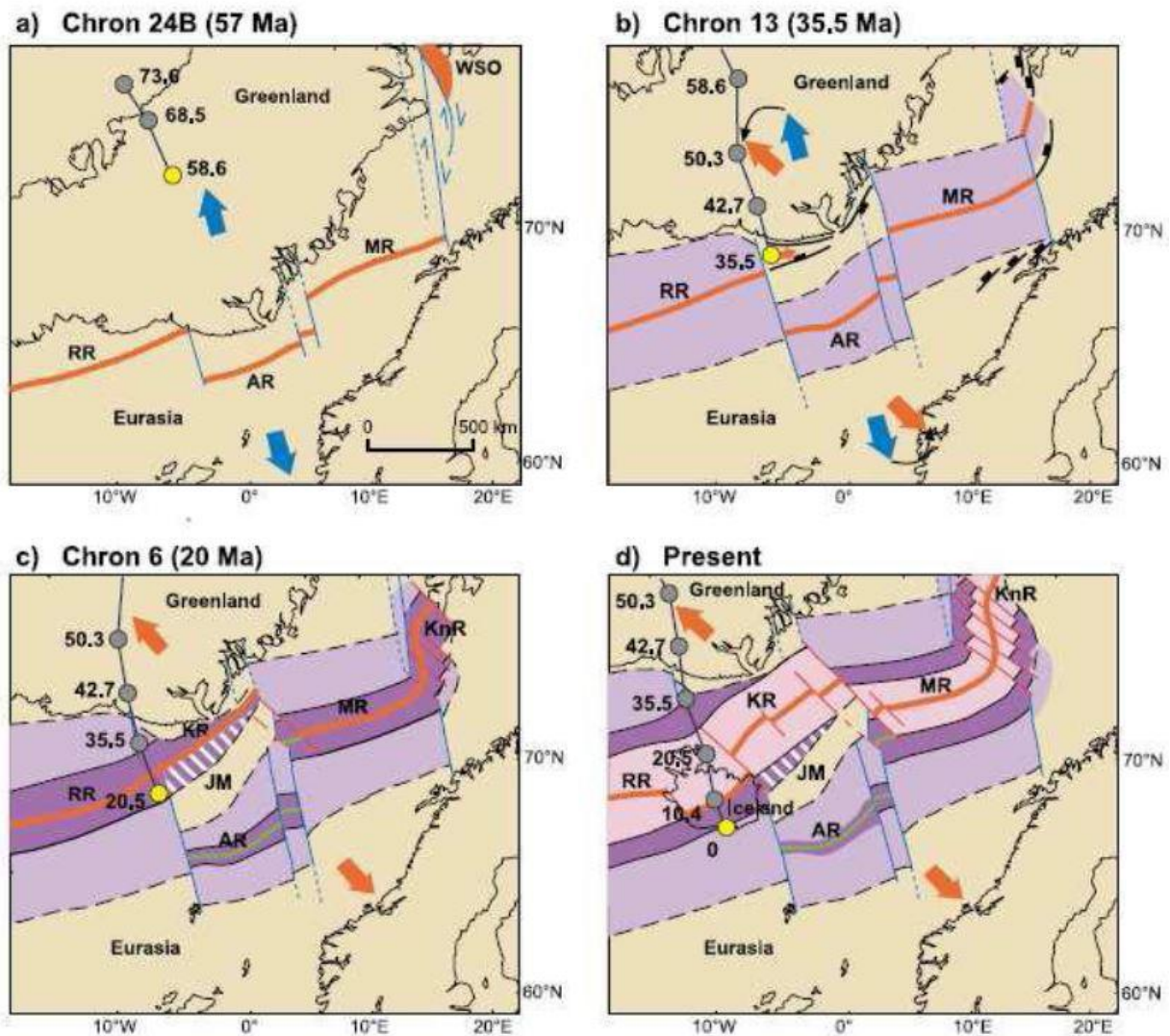
Figure 2.6: Opening of the North Atlantic at Chron 24B (a), Chron 13 (b). Chron 6 (c) and present date. From Lundin and Dore, 2002. RR=Reykjanes Ridge, AR=Aegir Ridge, MR=Mohns Ridge, KR=Kolbensey Ridge, JM=Jan Mayen Platform, KnR=Knipovich Ridge

The creation of the North Atlantic Ocean dates back as far as the Devonian era, after the breakup of the former supercontinent Pangaea. Opening of the Tethys ocean transitioned into the breakup between Gondwanaland and Euramerica at first, later splitting both supercontinents in two as the Atlantic Ocean opened. It gradually propagated northwards through remnant weaker zones in the Caledonian orogeny, creating Paleozoic and Mesozoic rift basins (Stanley, 2009). Seafloor spreading occurred as early as early Paleogene, at anomaly 24r-2, 53,7 Ma (Cande, Kent, 1995, Lundin, Doré, 2002).

13

At the Paleocene - Eocene transition, the opening of the northern North Atlantic Ocean changed from a three - plate configuration to a two - plate configuration (Fig 2.6a). Seafloor spreading in the Labrador Sea between Greenland and North America was halted, continuing exclusively between Greenland and Eurasia. At first, the region between Greenland and Svalbard did not open, but moved along a continent-continent mega-shear zone. This was a consequence of the relative motion between the two plates, having a NNW-SSE pattern. This relative motion and the lack of space between Greenland and Svalbard caused a small orogeny on western Svalbard, creating a large syncline, as well as the West Spitsbergen Shear Zone.

In early Oligocene, the relative plate motion changed, and the two landmasses moved apart, eventually creating the Knipovich Ridge (e.g. Mosar et al. 2002 and Fig 2.6b). Complete separation was not present at the start, but gradually propagated northwards over the cause of 20 Myr. The Ægir Ridge went extinct at Chron 6 (20 Ma, Fig 2.6c), as seafloor spreading was initiated at the Kolbeinsey Ridge (Lundin, Dore, 2002). This state of seafloor spreading has not changed since (Fig 2.6d).

3   Data and methods

3.1   Acquisition of data

As a base for this thesis, eleven lines of seismic data have been used. These data were acquired during two SVALEX cruises in 1999 and 2004 respectively (Mjelde and Johansen, 1999; Mjelde, 2004).
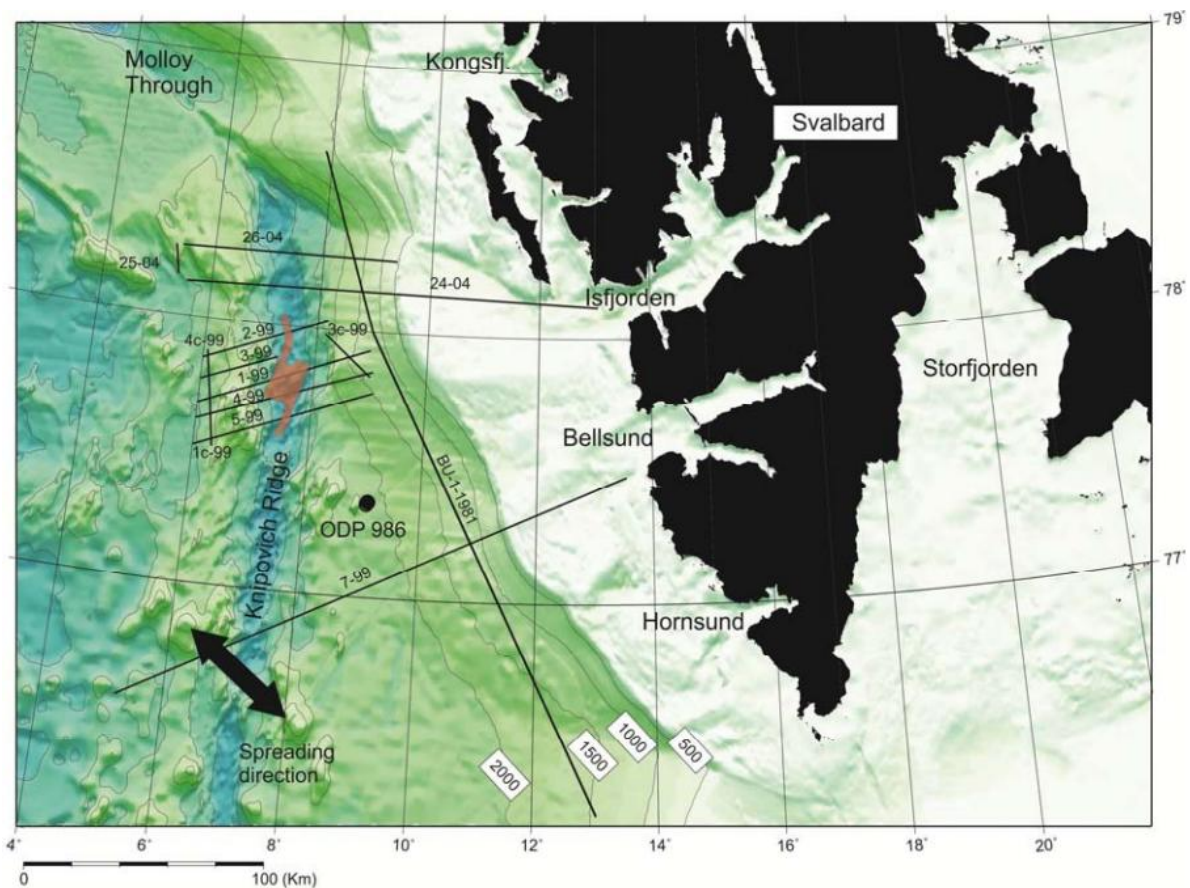
Figure 3.1: Lines acquired during the 1999 and 2004 surveys. Lines 7-99 and BU-1-1981 are not a part of this study.

During the 1999 SVALEX cruise, a total of eight lines were acquired from 22nd to 27th of September: Lines 1 - 5, 1c, 3c and 4c (Mjelde, Johansen, 1999; Fig 3.1). Lines 1-5 are parallel to each other trending in ENE/WSW direction, while lines 1c, 3c and 4c are intersecting lines, connecting lines 1 - 3, 3-4 and 4-5, respectively. The total length of all eight lines is 390,3 km. The data were originally acquired as a part of the student course GFJ294, but have been used for other scientific purposes as well.

15

Three lines were acquired during the 2004 SVALEX cruise from 4th to 6th of September: Lines 24, 25 and 26 (Mjelde, 2004, Fig 3.1). Lines 24 and 26 are parallel in ENE/WSW direction across the spreading axis, while line 25 was acquired perpendicular to the other lines. Unlike the data from 1999, it does not intersect with any other lines. The total length of the three lines acquired in 2004 is 273,8 km. The data were again acquired as a part of a student course, GEOL201.

In addition, bathymetrical data acquired by the University of Bergen during the 2004 SVALEX cruise have been used. These data cover most of the 2004 dataset, but only parts of the 1999 dataset.

Both cruises have been conducted on board University of Bergen vessels. The 1999 cruise was conducted by use of R/V Håkon Mosby, while R/V G.O. SARS was used during the 2004 cruise. An identical seismic source array was used, but with some differences in other acquisition equipment.

3.2   Data parameters

Data acquired during the 1999 SVALEX cruise have the following parameters:

Vessel:	R/V Håkon Mosby
Source:	Seven air guns consisting of two single 1200 cu.inch. and
	580 cu.inch. air guns combined with a centered five air gun string of 340/210/136/90/60 cu in. Total volume: 2616 cu.inch., fired at 138 bar pressure.
Receiver:	Analogue 3000 m streamer
Source depth:	10 m
Receiver depth:	7 m
Shot interval:	50 m
Group length:	25m
Channels:	120

Sampling length:	12 s
Sampling interval:	2 ms, 500Hz with the exception of line 2 which was sampled at 4 ms, 250 Hz
High-pass filter:	180 Hz at -72 dB/octave
Low-pass filter:	3 Hz at 18 dB/octave

Length of ENE/WSW lines across the spreading axis:

Line 1:	75,6 km
Line 2:	55,0 km
Line 3:	33,9 km
Line 4:	78,0 km
Line 5:	77,4 km

Intersecting lines:

Line 1c:	24,9 km
Line 3c:	26,4 km
Line 4c:	19,1 km

Line	Shots	UTM coordinates		Latitude			Longitude		
		Easting	Northing	Degrees	Minutes	Seconds	Degrees	Minutes	Seconds
01	300	0359714.1	08655729.4	77	55	45,48	8	59	24,36
01	1806	0286192.4	08637912.4	77	41	13,92	5	59	56,69
01c	300	0291298.2	08635078.0	77	40	08,76	6	13	42,31
01c	796	0291290.9	08659928.2	77	53	19,32	6	41	03,01
02	300	0289045.3	08926279.3	77	51	12,20	5	59	58,27
02	1400	0342430.6	08669608.9	78	02	08,88	8	11	14,03
03	300	0287619.1	08646770.9	77	46	03,00	6	00	05,11
03	977	0320515.6	08654954.4	77	52	53,76	7	19	57,32
03c	300	0341226.6	08664000.0	77	59	04,92	8	9	49,75
03c	828	0358607.3	08644128.7	77	49	30,36	8	59	37,57
04	300	0360585.3	08648544.2	77	51	58,32	9	32	09,74
04	1804	0284934.8	08629750.7	77	36	48,24	5	59	57,44
04c	300	0291293.6	08637078.0	77	41	12,12	6	12	56,66
04c	683	0291290.8	08617956.1	77	31	03,36	6	20	01,00
05	300	0283391.4	08619490.5	77	31	14,16	6	00	03,78
05	1846	0358460.3	08638137.1	77	46	17,76	9	04	08,46

Data acquired during the 2004 SVALEX cruise have the following parameters:

Vessel: R/V G.O. Sars

Source: Seven air guns consisting of two single 1200 cu.inch and 580 cu.inch. air guns combined with a centered five air gun string of 340/210/136/90/60 cu.inch. Total volume: 2616 cu.inch., fired at 138 bar pressure.

Receiver: Digital 2900 m streamer

Source depth: 6 m

Receiver depth: 8 m

Shot interval: 50 m

Group length: 12,5 m

Channels: 240

Sampling length: 12 s

Sampling interval: 2 ms, 500 Hz

High-pass filter: 180 Hz at -72 dB/octave

Low-pass filter: 3 Hz at 18 dB/octave

Length of ENE/WSW lines across the spreading axis:

    Line 24:   171,5 km

    Line 26:   89,9 km

Perpendicular line:

    Line 25:   12,4 km

Line	Shots	UTM coordinates		Latitude			Longitude		
		Easting	Northing	Degrees	Minutes	Seconds	Degrees	Minutes	Seconds
24	7	0454454.5	08673595.3	78	7	46,26	13	0	58,35
24	3436	0283917.0	08691255.6	78	8	16,54	5	32	28,61
25	11	0280540.5	08693478.8	78	9	9,60	5	22	59,30
25	258	0280295.3	08705933.5	78	15	44,36	5	16	58,10
26	6	0283302.0	08707169.8	78	16	39,60	5	24	16,08
26	1803	0372423.1	08695741.5	78	16	47,23	9	21	56,57

3.3   Data processing

Several steps of processing have been conducted by Sevmorgeo in St. Petersburg converting the raw data to the quality used in later interpretation. A short explanation of the

most important processing steps is presented below: (based on Sheriff and Geldart,1995 and Keary et al., 2002)

- **Geometric frame definition:** The distance between the GPS and seismic array is corrected before a reference frame containing source and receiver is established in a UTM coordinate system.

- **Muting:** The data are edited and muted to remove obvious errors. E.g. a malfunctioning group, or a trace with large amounts of noise or abnormally large amplitudes.

- **Gain recovery:** The signal strength of a seismic wave will decrease by an exponential factor due to factors like spherical spreading. This affects amplitude strength greatly and is compensated by amplifying the amplitude using a geometrical model.

- **Front muting:** The first arriving waves are muted to remove the direct wave.

- **Frequency band-pass filtering:** A trapezoid-shaped band-pass filter from a frequency of 6 - 10 Hz to a frequency of 60 - 70 Hz is applied. This removes unwanted frequencies and reduces ringing.

- **Deconvolution:** Or inverse filtering is used to improve seismic records by removing various filtering effects encountered by seismic waves during their passage through the ground. For instance, sea floor multiples are possible to attenuate by deconvolution as they are periodic and therefore predictive.

- **F-K filtering:** Instead of using frequency/distance as a reference, transforming a signal to the frequency and wavenumber domain, f - k, makes it possible to filter arrivals with different angle and velocity interfering in the standard f - x-domain.

- **Velocity analysis:** An analysis of move-out of common mid-point gathers is used to estimate the stacking velocity with depth.

- **Normal move-out correction:** As the distance between source and receiver progressively increases, so does the two-way travel time. Traces with a common mid-point (CMP) are possible to stack, but the increase in two-way travel time must be corrected first, by applying the stacking velocities. As this may cause problems when stacking shallow reflectors due to time stretching, the gathers are muted after NMO-correction.

- **Stacking:** NMO-corrected gathers are stacked to create a single trace with focus on constructive interference of reflective signals and destructive interference of noise and other unwanted signals.

- **Dip move-out:** Vital for correcting the effects of dipping layers after NMO correction. Post DMO-stacking will yield better results compared to pre-DMO-stacking of dipping layers.

- **Kirchoff migration:** This post-stack depth migration is used to reduce hyperbolic diffractions from e.g. faults or intrusions, and to move reflectors to their correct sub-surface position.

- **Trace mixing:** This is done to optimize visualization. Five neighboring traces are multiplied with each other using 1/2, 3/4, 1/1, 3/4 and 1/2 as weights.

- **Time-dependant band-pass filter:** Higher frequencies are more susceptible to absorption than lower frequencies. Over time, the higher parts of the frequency spectrum is thus dominated by noise. This filter removes the noise from these higher frequencies.

3.4   Data resolution

Seismic surveying uses body waves propagating through water, sediments and solid rock. Two types of body waves exist: P-waves and shear waves, or S-waves. P-waves propagate by compressional and dilatational uniaxial strain in the direction of wave propagation, while S-waves propagate by pure shear strain perpendicularly to the direction to wave propagation (Keary et al., 2002). Hydrophones used in both analogue and digital streamers register only P-waves. This is due to water having a shear modulus of zero, yielding a wave velocity of zero:

S-wave velocity:

$$v = \sqrt{\left[\frac{\mu}{\rho}\right]}$$

P-wave velocity:

$$v = \sqrt{\frac{K + {}^4/_3\mu}{\rho}}$$

Where κ is the incompressibility, μ the shear modulus and ρ density. Compressional waves travel faster than shear waves in the same medium, meaning that the first arriving waves will always be P-waves.

Whether an object is resolvable on seismic data depends on its size compared to the dominant seismic wavelenght λ at that location:

$$\lambda = \frac{v}{f}$$

The dominating frequency f will change at varying depths due to absorption. Over a certain distance, a high frequency will suffer larger total absorption compared to a lower frequency wave, as absorption is generally regarded as being a fixed proportion of the total energy for each oscillation of the rock particles involved. As a lower frequency propagates a larger distance per oscillation, the amplitude loss as a function of distance over time is lower. As such, the dominating frequency at shallow depths is around 40-50 Hz, while for deeper magmatic rocks the dominating frequency may be around 20 Hz. The velocity at which a seismic wave propagates will also change as the medium it propagates through is modified through e.g. compaction. Shallow sediments have V_p from 1,5 km/s to around 2,5 km/s, whereas the Vp in consolidated sedimentary rocks may exceed 5.5 km/s. Magmatic and metamorphic rocks forming the basement have larger V_p velocities ranging from 5,5 km/s to 7,0 km/s (Keary et al., 2002). Thusly, the seismic wave-length varies from around 30 - 60 m in shallow areas and 250 - 350 m in deeper parts.

Vertical resolution is defined as the ability to discern and recognize individual and closely spaced reflectors. It is defined by Sheriff and Geldardt (1995) to be between one-quarter and one-eight of the dominant wavelength of the pulse. Given an example from a shallow depth where the dominating frequency is 50 Hz and P-wave velocity is 2,0 km/s, the wavelength would be 40 m and the resolution about 10 m. Compared to a deeper example with a dominating frequency of 20 Hz and a P-wave velocity of 6,0 km/s, the wavelength is 300 m yielding a theoretical maximum vertical resolution of about 75 m. Vertical resolution is thus decreasing as a function of depth. It is however possible to enhance vertical resolution by using inverse filtering (Keary et al., 2002).

Horizontal resolution is determined by two main factors. The first is detector spacing. For a flat bed, the direct resolution will be half of the detector spacing. The second factor is

best described by an infinite point of point scatters, each contributing energy to the reflected signal. The reflected pulse is visualized as an infinite number of backscattered rays. Energy reflected back to a detector within half a wave-length will constructively build the reflected signal. This part of the interface is known as the first Fresnel Zone, or simply the Fresnel Zone as higher order Fresnel Zones are largely disregarded (Keary et al., 2002). Around this Fresnel Zone are a series of zones where the reflected energy tend to interfere destructively. The Fresnel zone is a representation of the absolute limit for which horizontal details can be distinguished. The width of the Fresnel Zone is calculated from the depth and wavelength when $z \gg \lambda$:

$$w = \sqrt{2z\lambda}$$

Again, the resolution decreases as a factor of depth, as the dominant wave-length increases. It is, however, possible to reduce the area of the Fresnel Zone by use of migration. For 2D seismic data the circular shape of the Fresnel Zone is migrated to an ellipse by focusing the energy from several traces, increasing the resolution to one-quarter of a wave-length in the shooting direction, while migration of 3D seismic data will further reduce the zone to one-quarter of a wave-length for all azimuths (Sheriff and Geldart, 1995).

4 Seismic Interpretation and Basin Modelling Methods

4.1 General

To record an object, surface or horizon in a seismic dataset, two requirements must be fulfilled. The object must be larger than the minimum vertical resolution given by the sources and geological features of the area (discussed in Chapter 3.4), and the interface between two layers must yield an acoustic impedance large enough for significant sonic wave reflection. The acoustic impedance is the product of speed (v) and density (ρ).

Using seismic interpretation as means to conduct geoscientific resesearch has its flaws. As most of the data collected are acquired from oceanic or land surfaces, results are acquired indirectly. In many cases, well logs or outcrops with the same geological features are tied to seismic surveys to yield a better understanding of the geology and geophysical properties. In this area of the North Atlantic there are no sources available to further determine the geology, nature of lithological boundaries and exact seismic velocities. Furthermore, these 2D seismic datasets have several sources of noise partially or completely distorting parts of the data. Steeply inclined seafloor, dipping surfaces, multiples and diffractions cause most of the noise. Despite this, the majority of the data is of good quality. In this 2D dataset, two-way travel-time (TWT) is used as a measure of depth instead of meters. This is a standard procedure, and TWT may be converted to real depth using one or more of the additional resources mentioned above. I.e. in petroleum surveys, well logs are often used, and sonic logging is perhaps the most accurate way of determining exact depth. It is possible to use standard values of velocity for a sonic wave propagating through a formation at a given depth and create a depth model. As the area has numerous fault systems, dipping layers, high relief, cracking, complex basement and gas hydrate occurrences, this method is far from accurate, but a viable option.

Modeling the basin when this is taken into account provides an estimate of subsidence. The modeling itself is based on the basement location at present time and does not reconstruct the basement to the time before sedimentary deposition. As such, any faults present and lengthening due to oceanic spreading is not calculated and remodeled. The oceanic crust is viewed as a complete body. This is due to the complex geological history and the aim with the present thesis is not to perform a complete reconstruction.

4.2   Seismic Interpretation

The 2D seismic profiles in this thesis have been interpreted in PETREL 2013 (Schlumberger). The data are displayed as interpolated density, where the changes in acoustic impedance are displayed as colour variations. Several options are available, where red/blue and standard seismic colour tables of black/yellow/red are the most common. The saturation and intensity of the colour display the amplitude of the reflected signal, and point to the value of change in acoustic impedance from the interface encountered. Here, AI is acoustic impedance v is velocity and ρ is the density of the medium.

$$AI = v\rho$$

And the amount of energy reflected by the interface is given by the Coefficient of Reflection R_c:

$$R_c = \frac{AI_2 + AI_1}{AI_2 - AI_1}$$

The change in acoustic impedance can have both positive and negative values. The two possibilities are found by identifying the peaks and troughs in the seismic. As the transition from water to sediments usually gives off a large increase in acoustic impedance, the seafloor reflector is used to determine if either a peak or trough indicates an increase in acoustic impedance. The use of both is widespread, where peaks as a standard is widely used by American petroleum companies and scientists, while troughs are more widespread as a European standard. By using wiggle traces, one can identify the standard used As the data used in thesis give a peak as the transition from sea to sediments, the profiles in this thesis use the American standard.

The data used in this thesis have previously been used in a former thesis by Kvarven (2009), and some of his results has been used to enhance the results produced here. Some additional lines have been interpreted to produce the final basis for use in basin modelling.

Seismic interpretation focuses on identifying key elements in the geology beneath the surface. Identifying a variety of geometrical signatures is vital to displaying an accurate mapping of the subsurface. The deposition of sediments leads to a variety of shapes and forms. Looking at the sedimentary basins, key factors include identifying the boundaries

between two structures, both top and bottom. These include erosional, concordant and toplap for the upper boundary, concordant, onlap and downlap for the lower boundary, as well as disconformity, noncomformity and angular unconformity as the common erosional contacts. Bradley (1985) suggested studying the amplitude, polarity and continuity of the seismic signals. This to better understand the larger change in coefficient of reflection when the sonic waves transmit to a medium with significantly higher acoustic impedance, from porous to solid mediums, or as the lateral and vertical continuity of the sedimentary infill. Sedimentary infill may have one of several internal reflection patterns.

Finally, the basin itself is shaped depending on the direction of sedimentary transport, the sedimentary process and amount of sediments fed to the basin.

4.3   Basin Modelling

As the present day geology and stratigraphical thicknesses of sedimentary layers in basins are products of the cumulative changes to rock volume and tectonics, decompaction and basin modeling are used to display a historical analysis of the sedimentary basin. The Knipovich Ridge is of interest here, as the ridge structure is vastly different on either side of the central spreading ridge. Being an asymmetric ridge system associated with large variations in sedimentary thickness, modelling might reveal to what extent differences in sedimentary deposition has caused the asymmetrical system.

Decompaction requires knowledge of the variation of porosity with depth, as a linear relation does not hold at greater depths. At large depths, the porosity would eventually become negative using these means of calculation. Normally, sedimentary infill follows a negative exponential relationship:

$$\phi = \phi_0{}^{-cy}$$

Where ϕ is the porosity at any depth y, ϕ_0 is the surface porosity and c is a coefficient depending on the sedimentary structure and lithology (Allen and Allen, 2013).
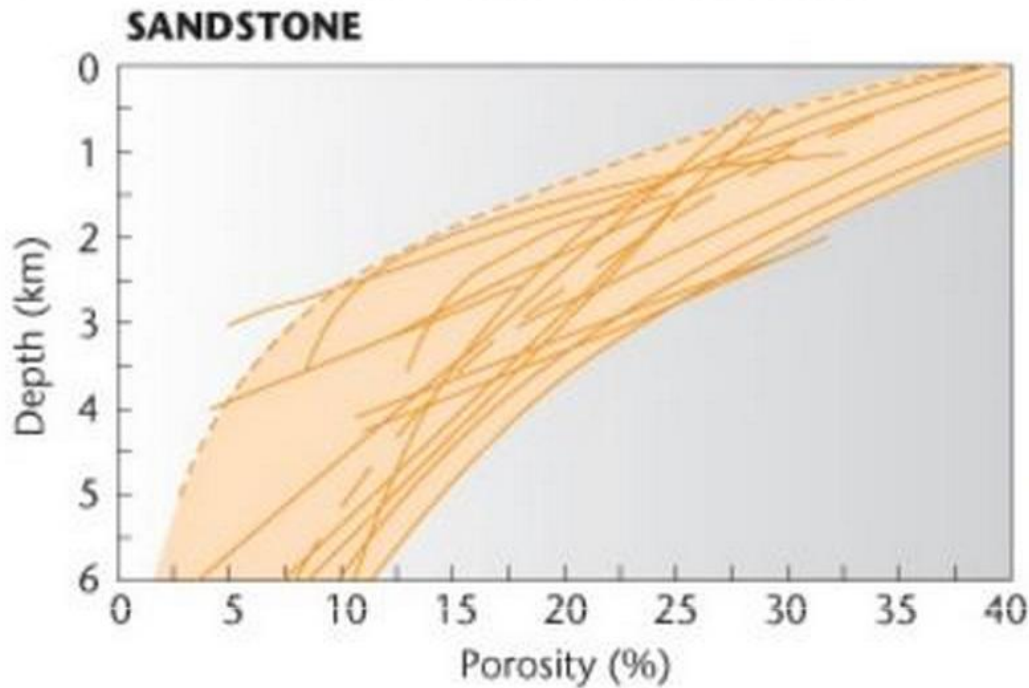
Figure 4.1: Porosity-depth curve for sandstone (Allen and Allen, 2013)

As sediments are buried to a given depth, the grain-to-grain contact force increases, and the lithostatic stress expels water from the matrix (Figure 4.1). While a decompacted sequence of sediment in a column is taller than in the original column, both columns in a water-filled basin has the same mass. The density of the sediments increases, but the water column is larger, as the expelled water mainly migrates upwards, thus replacing parts of the column previously occupied by sediments. No mass is gained or lost while decompacting, but the distribution of mass changes. It is possible to decompact a basin with great accuracy if data containing the age of sediments is available, i.e. from borehole data.

Backstripping is the exercise of partitioning the subsidence due to tectonics and that due to sediment loading (Allen and Allen, 2013). Locally, if the lithosphere is in Airy isostacy, the sediment loading can simply be used to calculate the tectonic component. The first step in 1D backstripping is to decompact the sediment column and reconstruct it to its depositional thickness. Using exponential curves for porosity/depth values as above, or power-law curves, is common when empirical data is not present. Using this, the decompacted thickness (S^*) as well as average density ($\bar{\rho}_s$) of a given sedimentary layer is expressed by the present day sedimentary thickness (S), as well as porosities of the present day (ϕ_s) and decompacted layer (ϕ_s^*), using the densities of water (ρ_w) and the sedimentary grains (ρ_g).

27

$$S^* = S\frac{1 - \phi_s}{1 - \phi_s^*}$$

$$\bar{\rho}_s = \rho_w \phi_s^* + \rho_g(1 - \phi_s^*)$$

Balancing the pressures at the base of both the decompacted and backstripped colums (Fig 4.2, a and b) will yield the basement depth, using the average gravity (g), the average density of the lithosphere (ρ_m) and water depth at the time of deposition (W_d), producing the recovered tectonic subsidence (TC) (Steckler and Watts, 1978).

$$\rho_w g W_d + \bar{\rho}_s g S^* + t_c \rho_c g = TC\rho_w g + \rho_m g Z_m + t_c \rho_c g$$

Solving Z_m from figure 4.2, the portion of the mantle above the compensation depth is, with Δ_{sl} being the mean sea level height correlated to present day values:

$$Z_m = W_d + S^* + t_c - (TS + \Delta_{sl} + t_c)$$

Rearranging, substituting and solving the equation for TC (Steckler and Watts, 1978), the above equation yields the following:

$$TC = S^*\left(\frac{\rho_m - \bar{\rho}_s}{\rho_m - \rho_w}\right) + W_d - \Delta_{sl}\left(\frac{\rho_m}{\rho_m - \rho_w}\right)$$
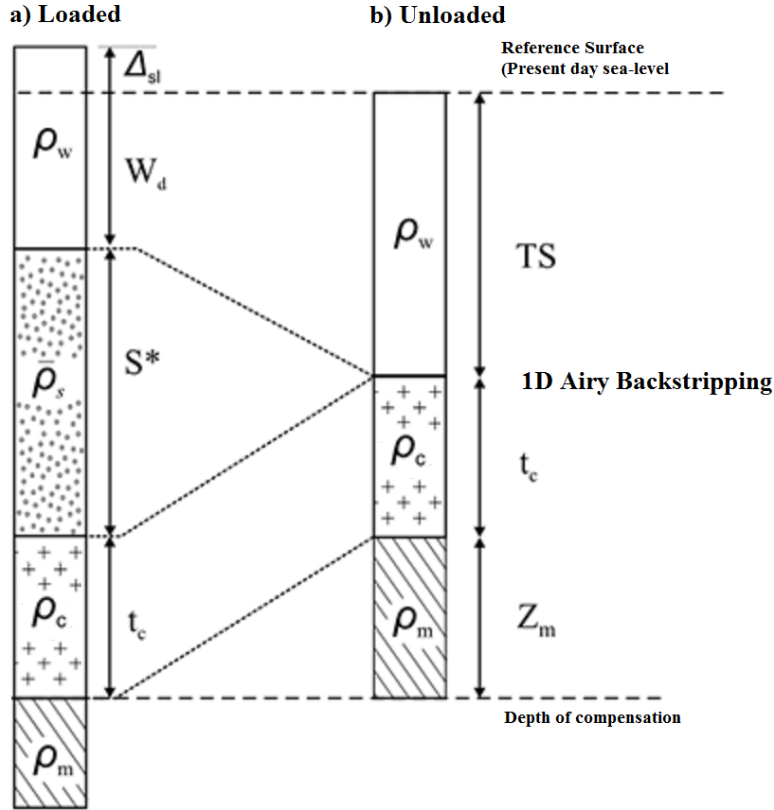
Fig 4.2: Single-dimension Airy backstripping (Modified from Allen and Allen, 2013; Steckler and Watts, 1978).

The above equation calculates isostatic rebound from three parts. In order, they are the sediment loading, water depth and eustatic changes, respectively. However, as a sedimentary basin in reality represents a set of sedimentary accumulations, it is necessary to perform several iterations of the equation to fully calculate the total isostatic rebound of the oceanic crust. Thus, calculating *TS* by backstripping must be done for each sedimentary layer at a given time during the evolution of the basin. Following this, recalculating the porosities and thicknesses of all sedimentary layers must be done as well. As a layer is removed, the initially calculated average density $\bar{\rho}_s$ no longer holds, and it must hence be recalculated. Given that when i is the ith layer and n the number of layers at a given timestep, recalculation is done to the basement elevation (Watts, 2001):

$$\bar{\rho}_s = \frac{\sum_{i=1}^{n}[\rho_w \phi_{si}^* + \rho_g i(1 - \phi_{si}^*)]S_i^*}{S^*}$$

29

This is one of two ways to perform backstripping, however only yielding a point reference. This method of calculating backstripping is typically performed using borehole data, such as sonic and density logs, rock and sediment samples, accurate depth and lithology data as well as porosity. Using these data parameters, a complete subsidence history is created (Steckler and Watts, 1978). As these data usually are available only onshore or from continental shelves, deeper or remote surveys do not benefit from the additional data. Often, these wells are found in relation to the petroleum industry.

However, if the sediment load is supported by a regional flexure of the lithosphere, both the spatial load and elastic thickness T_e or flexural rigidity D of the lithosphere must be known. A 2D or 3D flexural backstripping technique provides access to the subsidence history of larger basins (Watts and Torné, 1992), but lack the detailed stratigraphy and paleo-environmental information of 1D borehole backstripping. When possible, these two techniques should be used in conjunction, providing a combined image of the geological history (Stewart *et al*, 2000).

When basin modelling is applied to determine the deformation of the lithosphere associated with long-term loading in 2D, e.g. a sedimentary basin such as a foreland basin or rift basin, it is viewed as a thin elastic plate with a thickness much smaller than length overlaying an inviscid substrata with no resistance to deformation that acts at every point along the plate (Watts, 2001). The force applied to the overlaying elastic plate is proportional to the deflection produced by the load applied to the plate. Elastic thickness T_e is widely used as the thickness of the elastic plate itself, where the flexural rigidity D of the plate is given as a result by this formula, where E and v are Young's Modulus and Poisson's Ratio respectively:

$$D = \frac{ET_e^3}{12(1-v)}$$

Also, it assumes that only the stresses in the plane of the plate are significant, so that linear elasticity can be applied. This yields the following equation (Timoshenko and Woinowsky-Krieger, 1959):

$$D\nabla\nabla w + 2\frac{\partial D}{\partial x}\frac{\partial}{\partial x}\nabla w + 2\frac{\partial D}{\partial y}\frac{\partial}{\partial y}\nabla w + \nabla D\nabla w$$

$$- (1-v)\left[\frac{\partial^2 D}{\partial x^2}\frac{\partial^2 w}{\partial y^2} - 2\frac{\partial^2 D}{\partial x \partial y}\frac{\partial^2 w}{\partial x \partial y} + \frac{\partial^2 D}{\partial y^2}\frac{\partial^2 w}{\partial x^2}\right] + p = q$$

Where the spatial positioning *x* and *y* yield *p* and *q* as the vectors representing the force distribution due to loading and in respect to that, the force exerted by the substrata respectively.

When viewing a plate under deformation from a sedimentary load, the amplitude of the load *h(x,y)* itself is given by:

$$q(x,y) = (\rho_s - \rho_w) * g * h(x,y)$$

And the flexural deformation *w(x,y)* based on the density of the mantle and sedimentary infill:

$$P(x,y) = \left(\rho_m - \rho_{innfill}\right) * g * w(x,y)$$

If it is assumed above that force is only exerted in the vertical direction *x* and not perpendicular to the plane itself, and in addition one assumes uniform elastic thickness T_e and infinite extent of the plate, one can draw the partial derivatives from the equation above and substitute the forces exerted on it, yielding (Watts, 2001):

$$D\frac{d^4 w}{dx^4} + \left(\rho_m - \rho_{infill}\right) * g * w(x) = (\rho_s - \rho_w) * g * h(x)$$

This equation is easier to compute in the frequency domain. Bold uppercase letters are Fourier transformations of lower case variables with same denotations:

$$D * k^4 * \mathbf{W}(k) + \left(\rho_m - \rho_{infill}\right) * g * \mathbf{W}(k) = (\rho_s - \rho_w) * g * \mathbf{H}(k)$$

The wavenumber in the x-direction k is given by $k = 2\pi/\lambda$ where λ is the wavelength. The wavelength is dependant on the length of the profile, as well as the intervals between each calculated iteration of load and flexure (Watts, 2001).

The final equation calculating flexural deflection of a thin elastic plate is acquired by rearranging the above equation (Watts, 2001):

$$\boldsymbol{W}(k) = \left(1 + \frac{Dk^4}{(\rho_m - \rho_{infill})g}\right)^{-1} * \frac{(\rho_s - \rho_w)}{(\rho_m - \rho_{infill})}\boldsymbol{H}(k)$$

To acquire the resulting deflection *w(k)*, the Inverse Fourier Transformation is applied to the above equation (Watts, 2001). In Matlab, Fast Fourier Transformation (fft) and its inverse (ifft) are used respectively to perform these calculations.

5 Seismic Interpretation and Basin Modeling

5.1 General remarks

All seismic lines shown in Fig. 5.1 have been interpreted, but basin modelling has not been performed on the tie-in lines (1c, 3c, 4c and 25) and lines 26 and 6. Line 6 has not been modelled due to its location in Isfjorden, line 26 due to the high magnitude of noise, mainly caused by multiples present in the data, and the tie-in lines due to their short length. They have been used to tie profiles together in PETREL and are used as a tool in the seismic interpretation only. Modelling them would yield a relatively flat surface post-modeling.
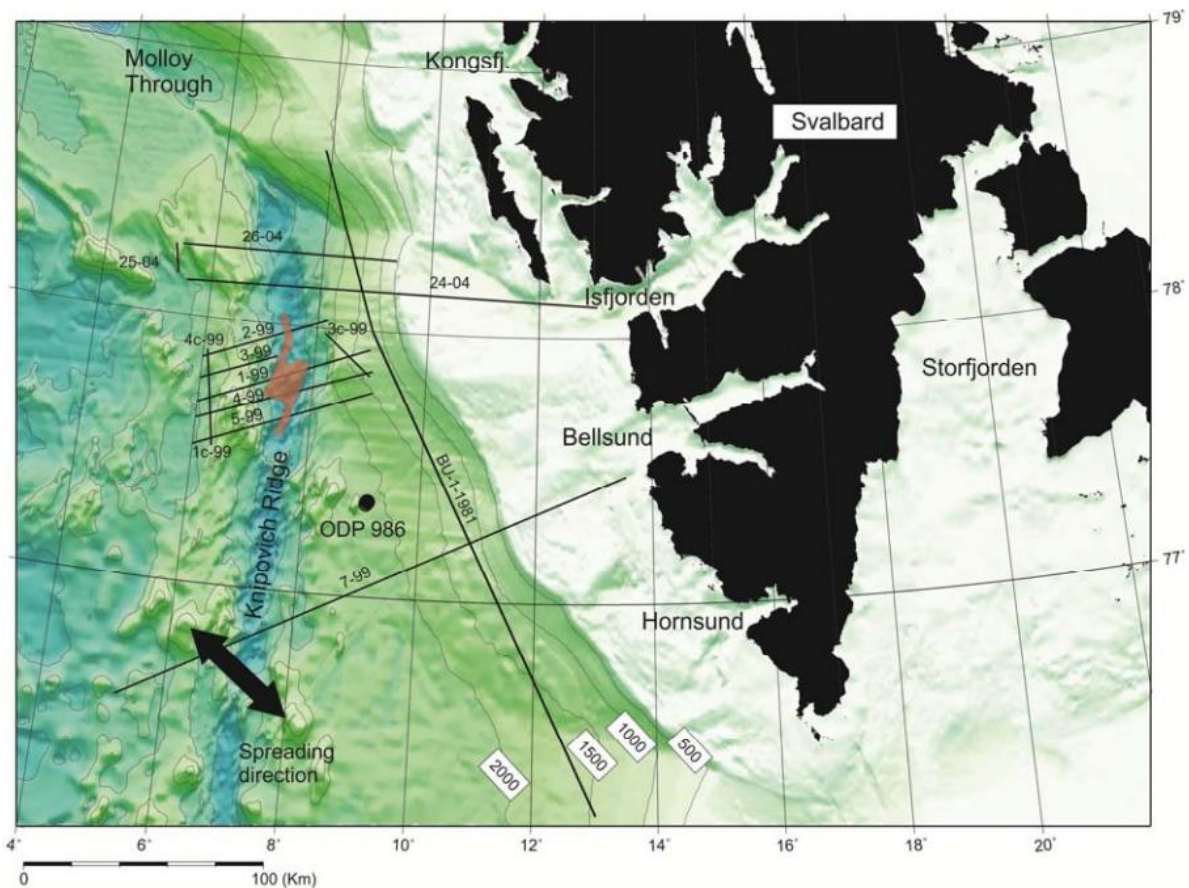
Figure 5.1: Map of the survey area and acquired seismic lines during the 1999 and 2004 surveys. Line BU-1-1981 is not a part of this study.

The data used in this thesis have been used in a previous study (Kvarven, 2009), but has been reworked in great detail. All sedimentary horizons have been reviewed and adjusted, basement and seafloor reworked and completed as horizons, as well as the addition, reworking and removal of a number of faults.

33

The processed data contain some unwanted arrivals, such as water multiples, peg-leg multiples, diffractions due to faults and fractures, as well as side-sweeps (Dergrunov et al., 2004).

The sedimentary distribution across the Knipovich Ridge is mainly related to the proximity to Svalbard. During the glacial periods the last 2.7 myr, sediments were deposited on the continental shelf, and due to the large input of sediments, extending it. In some areas, the shelf itself is as narrow as 30 km, causing glacial sediments to be deposited in the ridge valley itself (Faleide *et al,* 1996). The valley is flanked on both sides by tall basement ridges, and according to Austegard and Sundvor (1991), as well as Crane *et al.* (1998), there are thick accumulations of sediments on the western flank of the rift valley.

The data extracted from PETREL for line 24 is found in the appendix. Other lines were not included in the appendix due to the length of these datasets.

5.2   1999 – Data

5.2.1   Line 1

Line 1 is the third ESE-WNW-trending line counting from north to south (Fig 5.1).
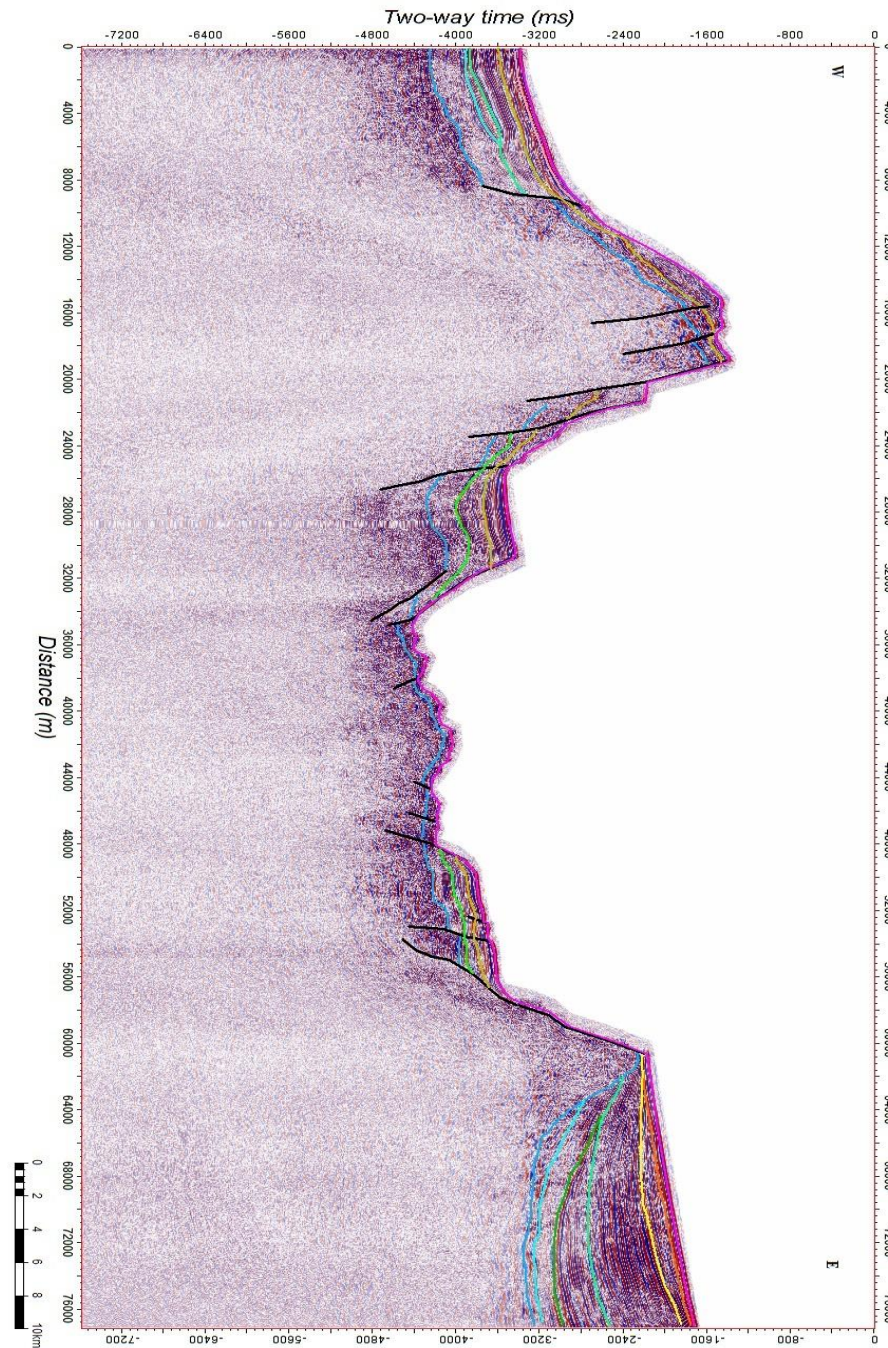

Figure 5.2: Line 1 from the 1999-dataset. See fig. 5.1. for location. Blue reflector: top magmatic crust basement

Sediment accumulation and seismic interpretation

The western flank basin (Fig. 5.2) contains around 900ms of sediments above the interpreted basement. The basement itself slopes upwards towards east from 4200ms to around 3600ms. Kvarven (2009) interprets the sedimentary segments to be divided into four units, of which the upper three are laminated and the bottom segment mainly consists of distorted and chaotic reflectors. This may be due to gravitational movements or tectonic events. Segment three from the bottom is interpreted by Kvarven (2009) to be a contourite deposit, although it could possibly also represent depositions from gravitational flows from the ridge. Segment two is well laminated, and it has about the same thickness throughout the basin. All segments onlap the ridge to the east of the basin. Here a large fault with 800ms offset marks the eastern limit of the western flank basin.

The western ridge crest itself shows a decrease in seafloor reflector depth from 3000ms to 1300ms at the top. A conversion from TWT to actual depth, using a water velocity of 1.5 km/s, gives depths of around 2.5 km in the western sedimentary basin and 1.1 km at the western ridge summit. There are sediment accumulations present on the ridge, estimated to be around 300-400ms in thickness. The reflectors are chaotic and yield little information about the internal structures of the sediments. Multiple faults are found on the top of the ridge, all trending towards east. Several larger normal faults create the ridge slope into the rift basin itself. As with the sediments on the top of the ridge, the sediments on the slope towards the rift basin are chaotic and contain no significant reflectors. A small ramp of around 6km lateral extent is found at 3500ms depth before reaching the rift basin. This ramp contains several sedimentary packages similar to those found in the western basin. The total thickness of these sediments is 900ms. The two upper strata are well laminated and assumed to be of glacimarine origins, while the bottom strata are chaotic. Kvarven (2009) deducts that these sediments have undergone post-depositional rotation.

The rift valley itself contains little or no sedimentary deposits. Multiple normal faults are interpreted, and a higher number than interpreted might be present. This is due to the chaotic nature of the seismics data, making it difficult to identify all larger faults.

On the eastern flank of the rift valley, thicker sedimentary accumulations are present. This area has sediments with similar characteristics to that of the ramp on the western flank of the rift valley. Kvarven (2009) find similarities between these two sedimentary accumulations, stating that they at one time may have been joined before rifting occurred.

This observation is supported by the present interpretation, but some faults have either been moved, added or redrawn to provide a better picture.

The continental slope to the east of the ridge contains a much larger sedimentary accumulation. Closer to the main fault separating the rift valley from the shelf the thickness accumulates to around 100ms. However, all sedimentary packages pinch out and drape onto the interpreted basement, and increase in thickness closer to Svalbard. The maximum thickness is close to 1800ms. The majority of these sediments have distinct layering and lamination, and it is assumed that their origins are related to the last major glacial periods.

Basin Modelling
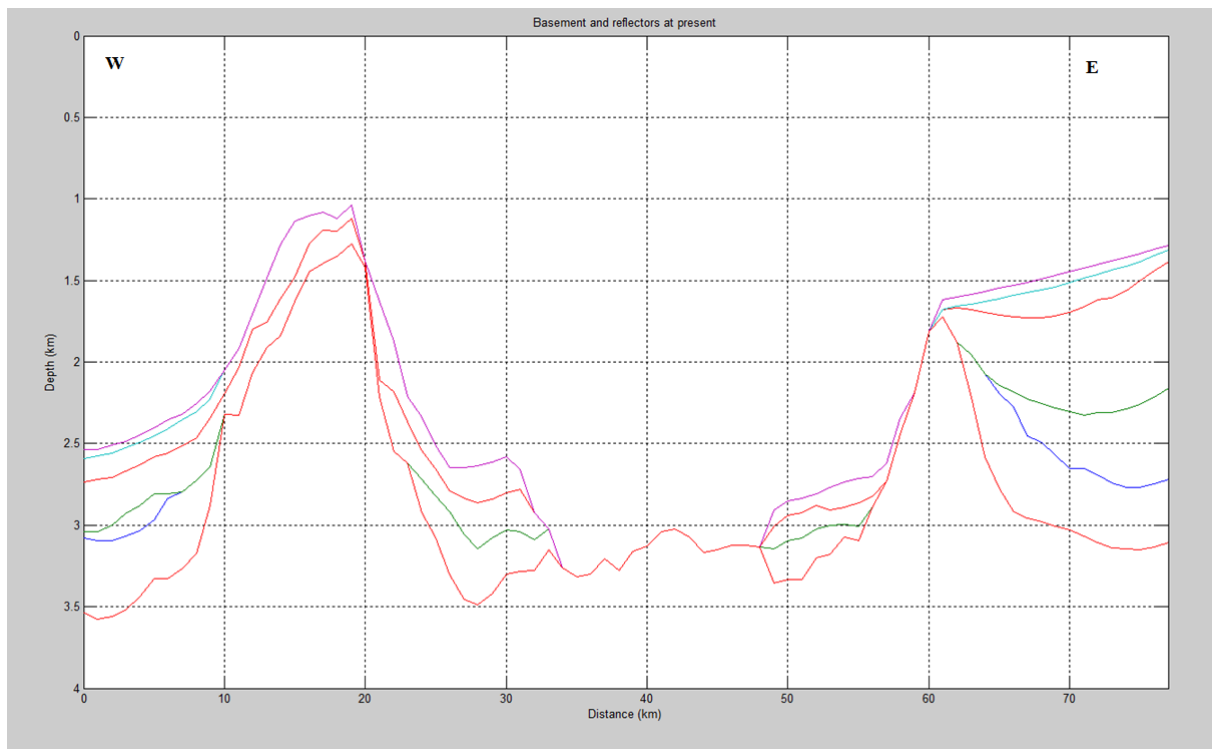
Figure 5.3: Depth converted from TWT line 1 picked with 1km intervals. Velocities are taken from Faleide et al. (1996), Ljones et al. (2004) and Kandilarov et al. (2008).
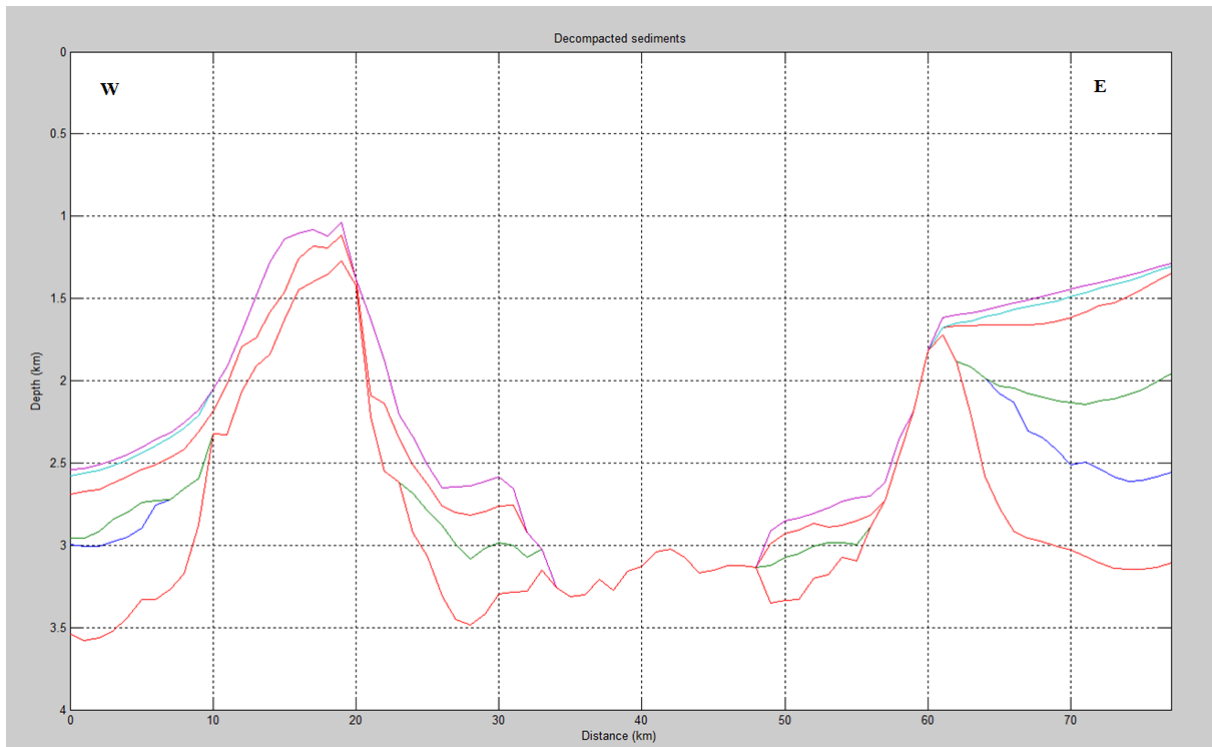
Figure 5.4: Line 1 with all sedimentary units decompacted
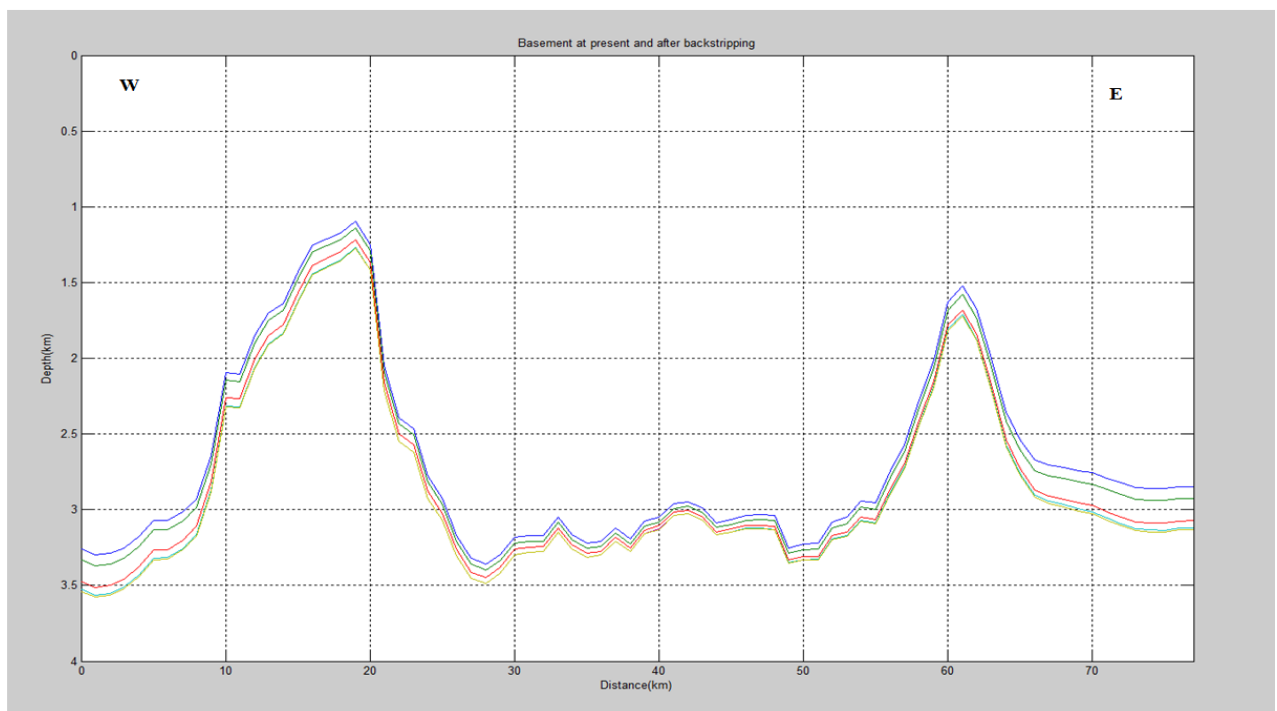
Figure 5.5: Basement modeled after removal of successive sedimentary units for line 1. The bottom, yellow line is the original basement depth, lime green is basement depth with the first sedimentary unit backstripped, red is basement depth with the second sedimentary unit backstripped, dark green is basement with the third unit backstripped and the blue line is the final basement depth with all sedimentary units backstripped
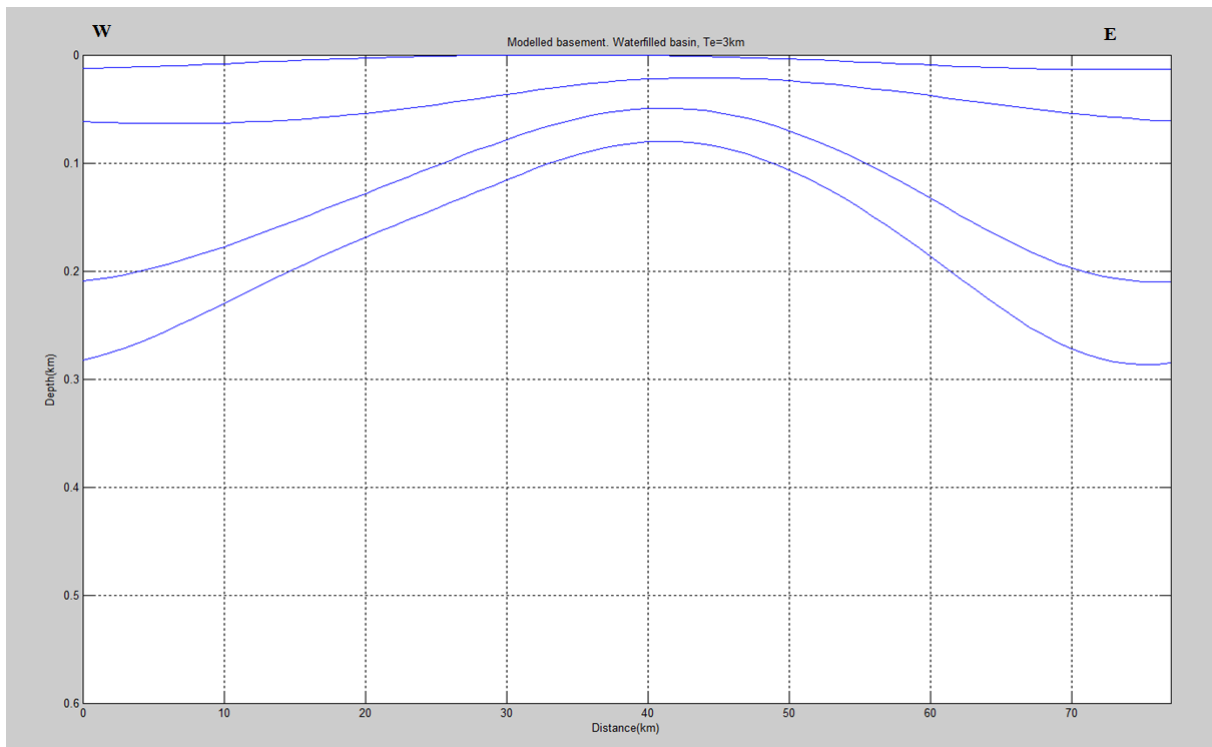
Figure 5.6: Modeled basement depth Δd, cumulative changes in basement depth after backstripping for line 1. The upper line is the change in basement depth with one sedimentary unit backstripped, the second and third lines show the change in basement with two and three units backstripped respectively. The lowermost line is the total change in basement depth with all sedimentary units backstripped

Using the PETREL-data, twt-traveltimes are extracted and compiled into a datasheet. These times are converted to depth (Fig. 5.3) using the average seismic P-wave velocity compiled in previous studies (Faleide et al., 1996, Ljones et al., 2004 and Kandilarov et al., 2008). The data are then modeled to yield a modeled basement with no sediment cover. Faults are treated as static basement.

The depth converted line 1 yields a thick sedimentary cover on both the eastern and western flanks (Fig. 5.3). The units interpreted in PETREL have been compiled into five separate units when modeled. These are divided into the four mega-sequences G0-III, and GIII has been divided into two where required. The western flank basin has a sediment thickness of up to 1200m with all mega-sequences present. Mega-sequences G0, GI and GII are substantially thicker than GIII, which is assumed to be due to the large sediment input during and before the large glacial periods initiated at 2.3Ma (Faleide et al., 1996). The rift basin itself has a very thin sedimentary cover. The axial high 40km into the profile is interpreted as an active ridge with ongoing seafloor spreading, and the bathymetric data suggest the presence of small sedimentary basins both north and south of this line. This is

39

reflected in other profiles. On the eastern flank, the sediment thickness is determined to be up to 2000m. Here, all mega-sequences are present, where mega-sequence GI and GII account for the majority of the sedimentary cover.

When the sedimentary units are decompacted, both the thickness and burial depth are taken into account (Fig. 5.4). The older mega-sequences G0 and GI are buried beneath up to 1000m of sediments, yielding a better image of their original thickness when modeled. Note that while the modeled thickness is representative of the time of deposition, tectonic activity has shaped the profiles as well. This is not accounted for in the modeling process. Unit 1, mega-sequence G0, is at the eastern end of the profile 300m thick. When decompacted to its original depth after deposition, it has a thickness of 540m (Fig. 5.4). Unit 2, mega-sequence GI, has a thickness of 570m, and is modeled to have an original thickness of 700m. Unit 2 has a substantially thinner burial depth at present and is modeled from its present thickness of 760m to 800m when originally deposited. The results are similar for the western flank basin. Unit 1, the thickest unit, is modeled to be 570m thick when originally deposited, compared to 480m at present date. Other units show minor changes, either due to lower burial depths or thinner depositions.

The modeled basement (Fig. 5.5) is shown after successive back-stripping of each sedimentary unit. An elastic thickness of 3km is used (Austegard, 2014; pers.comm). The lowermost interface is the basement at present day, while the interfaces above show changes to basement depth when sedimentary units are successively removed. The total isostatic rebound is shown in Figure 5.6. The changes in isostatic rebound are higher at the eastern and western ends of the profile. Back-stripping unit 5 and 4, mega-sequence GIII, yields minor changes in basement depth. Across the profile, the change is less than 15m, and lowest in the rift basin. This is due to the low thickness of this unit. Back-stripping unit 3, mega-sequence GII, yields an isostatic rebound of 60m at both the western and eastern ends of the profile. The isostatic rebound gradually decreases towards the rift basin. Here, the isostatic rebound is 20m. When unit 2 is back-stripped, the isostatic rebound is more substantial. The thicker sedimentary unit causes an isostatic rebound of 210m at both ends of the profile. This gradually decreases towards the rift basin, where the isostatic rebound is 50m. To the west of the rift basin, the change in isostatic rebound is close to linear and gradually decreases from the edge of the profile towards the rift basin over a distance of 45km. This marks a difference to the eastern part of the profile. The isostatic rebound changes drastically over the next 30km of the profile. This is due to the thicker sediment cover on the eastern flank, as well as the

units' confinement to the flank basin. Back-stripping the last unit yields changes similar to that of removing unit 2. Isostatic rebound is around 280m in both the eastern and western part of the profile with a lower change within the rift basin.
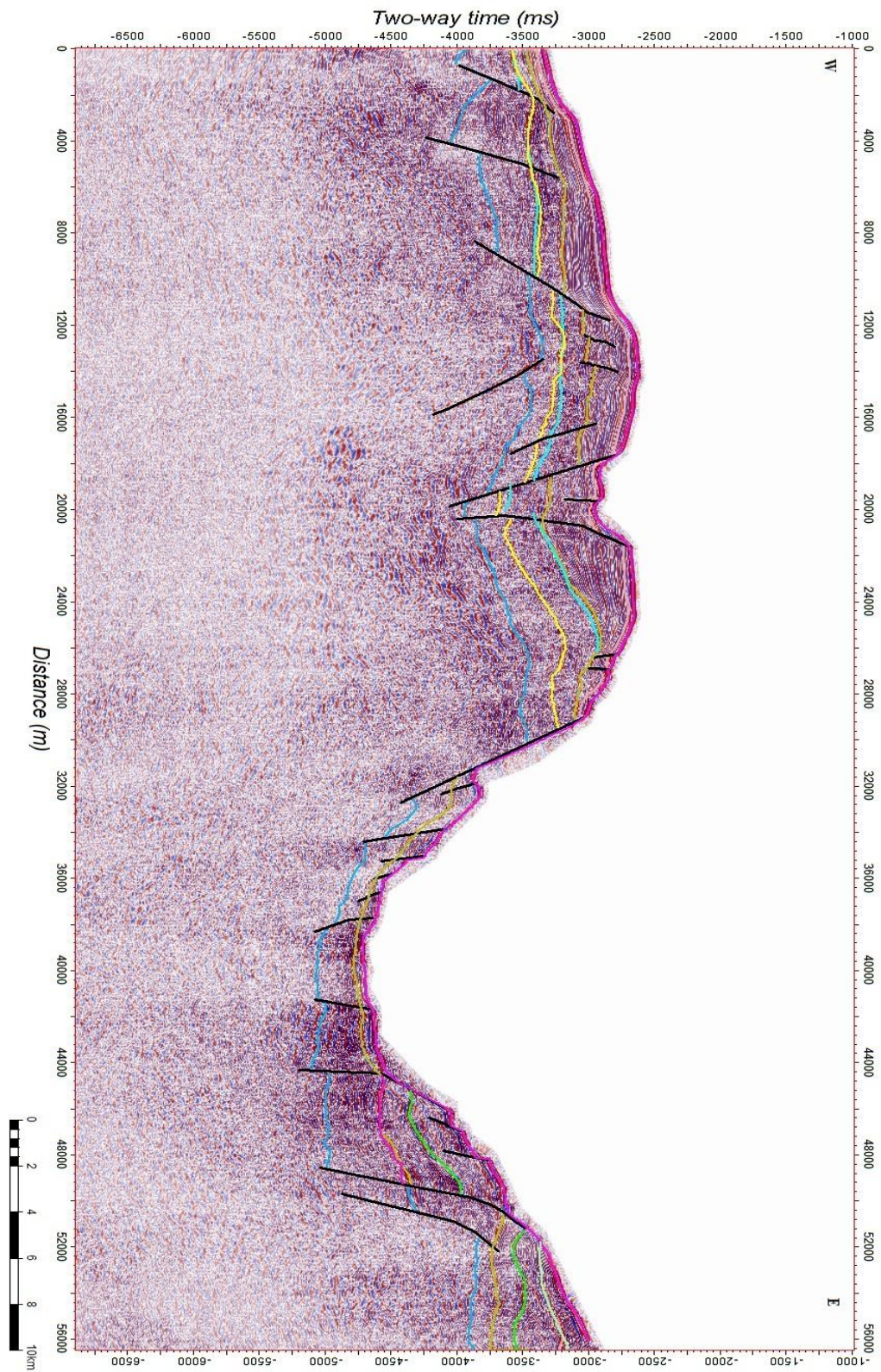
5.2.2 Line 2

Figure 5.7: Line 2 interpretation from Petrel

Line 2 is the southernmost of the ESE-WNW – trending lines of the 1999-data.

Sediment accumulation and seismic interpretation

The structural geology of Line 2 (Fig. 5.7) is significantly different from the three northernmost lines, but it has similar structures to that of Line 3. There is no large western ridge crest, so the profile has a more symmetrical appearance. The western part of the profile from 0 to 30 km appears to have a relatively uniform distribution of sediments of the same origin. This part of the profile has also multiple normal faults, where those east of the small graben located at 20km into the profile trend towards the east.

Basement is interpreted to be at 3850ms at the start of the profile, trending upwards towards 3500ms at about 15 km into the profile. It maintains this level of depth along this horst, before sloping downwards and being cut by faults into a smaller graben. At the western edge of the rift basin edge, the basement climbs to a height of around 3250ms, before being cut by large faults into the rift basin. The sediments covering the western flank of the profile are uniformly around 600-800ms thick. The upper 500ms are well laminated and divided into two layers by Kvarven (2009). The bottom layer is composed of more distorted sediments and sub-parallel layering.

The rift valley has 400ms of sediments covering the basement. These sediments have traces of parallel structures and have relatively large amplitude variations.

To the east of the rift basin, the interpretations is much more difficult. This is partly due to the distorted signals at 52km, and partly due to generally noisy seismic. Three large faults displace the basement from 5000ms to 3800ms at the top of the western ridge.

Basin Modeling
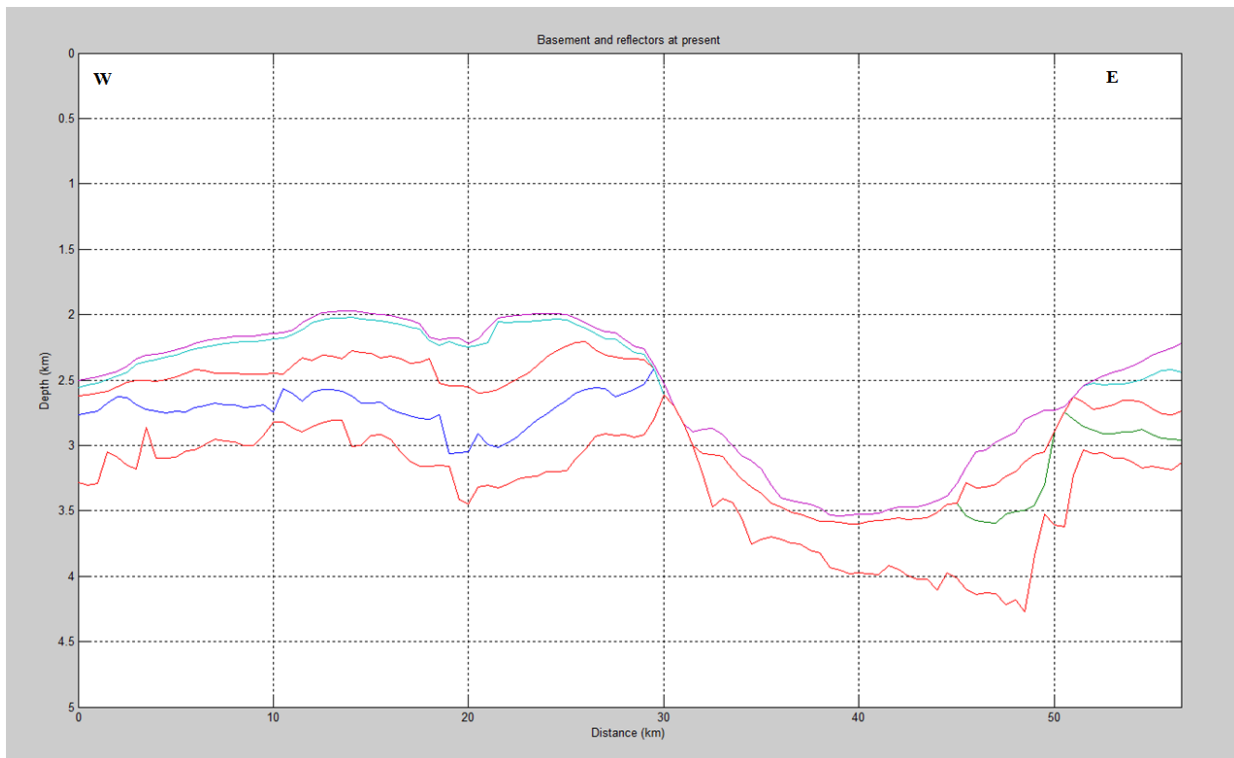
Figure 5.8: Line 2 depth-converted. Picked at 0,5km intervals. Velocities are taken from Faleide et al. (1996), Ljones et al. (2004) and Kandilarov et al. (2008).
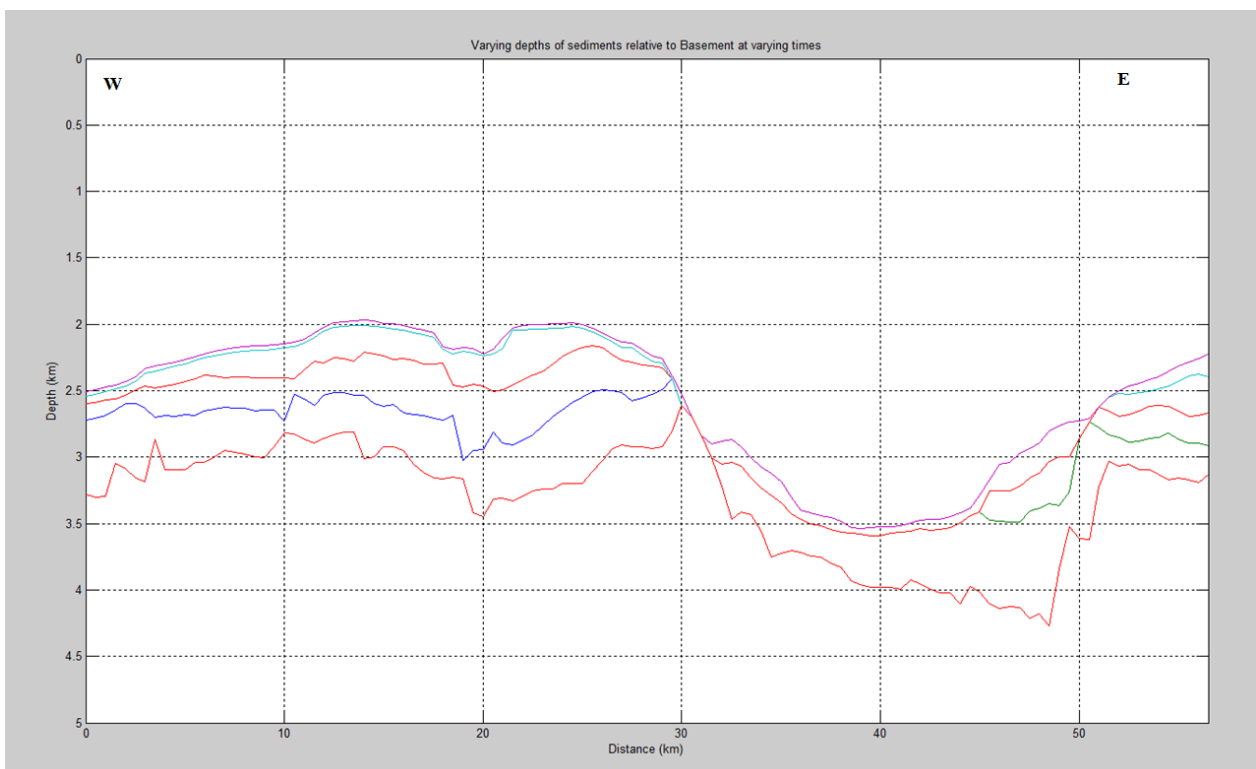
Figure 5.9: Decompacted sediment units from line 2

44
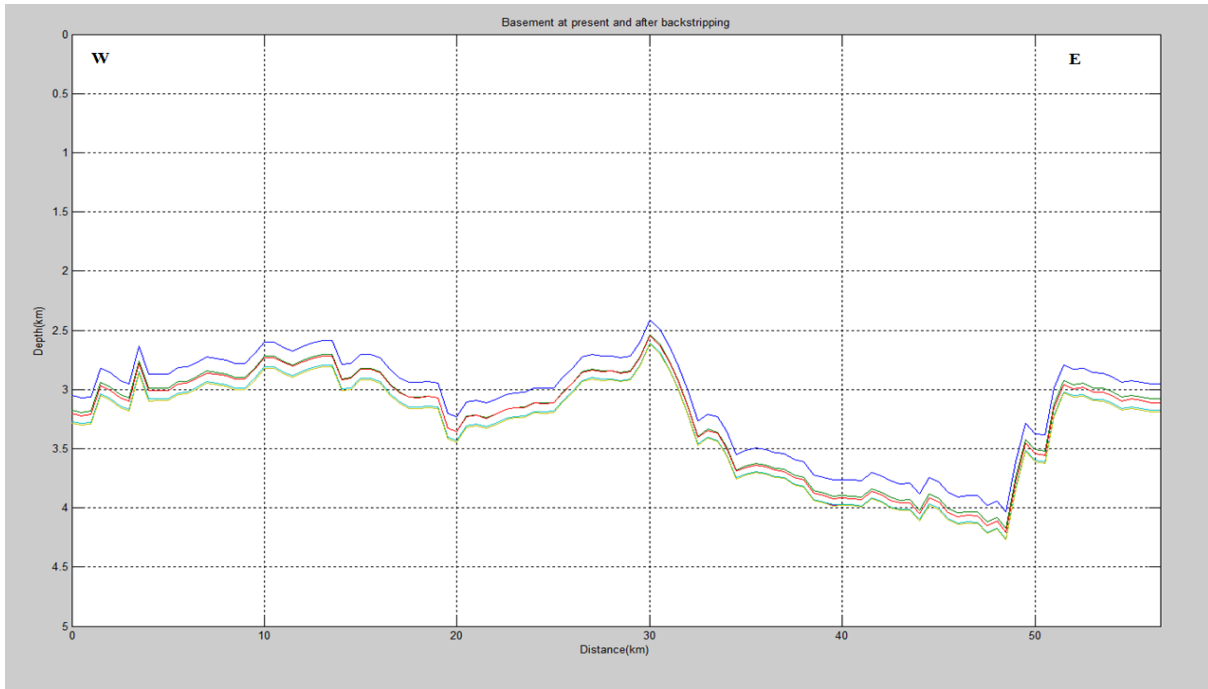
Figure 5.10: Basement modeled after removal of successive sedimentary units for line 2. The bottom, yellow line is the original basement depth, lime green is basement depth with the first sedimentary unit backstripped, red is basement depth with the second sedimentary unit backstripped, dark green is basement with the third unit backstripped and the blue line is the final basement depth with all sedimentary units backstripped.
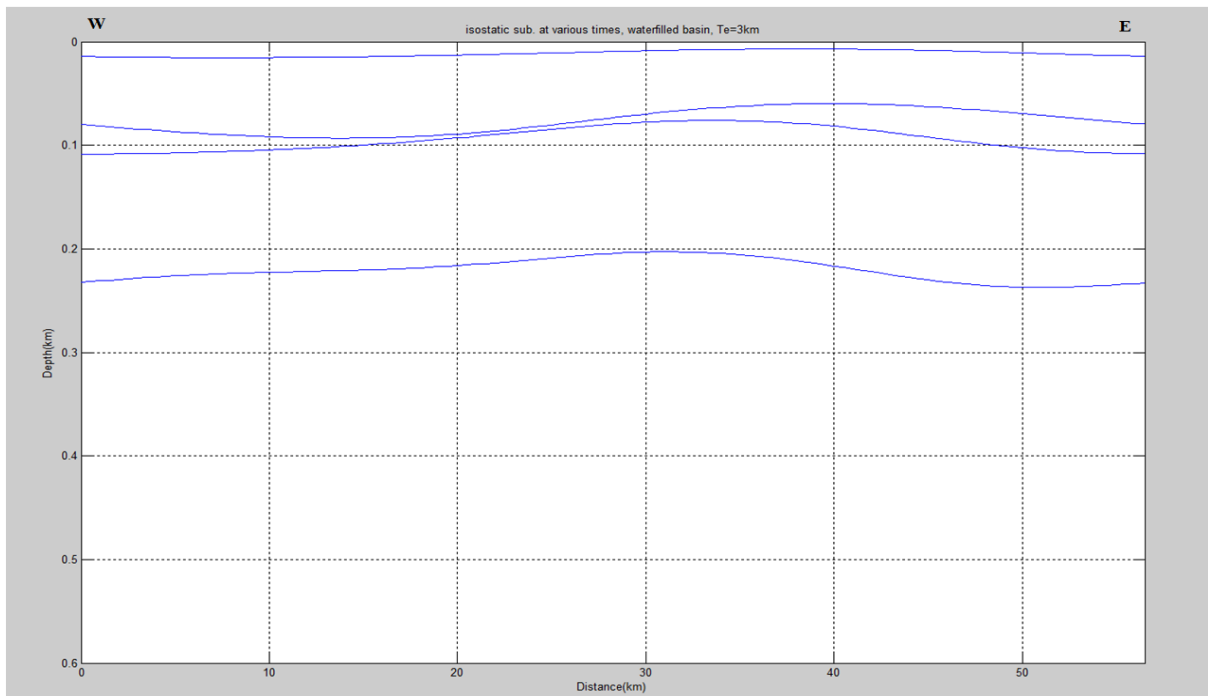
Figure 5.11: Modeled basement depth Δd, cumulative changes in basement depth after backstripping for line 2. The upper line is the change in basement depth with one sedimentary unit backstripped, the second and third lines show the change in basement with two and three units backstripped respectively. The lowermost line is the total change in basement depth with all sedimentary units backstripped.

45

Using the PETREL-data, twt-traveltimes are extracted and compiled into a datasheet. These times are converted to depth (Fig. 5.8) using the average seismic P-wave velocity compiled in previous studies (Faleide et al., 1996, Ljones et al., 2004 and Kandilarov et al., 2008). The data are then modeled to yield a modeled basement with no sediment cover. Faults are treated as static basement.

The depth-converted line 2 has a thick sedimentary cover throughout the profile (Fig. 5.8). The units interpreted in PETREL have been compiled into five separate units when modeled. These are divided into the four mega-sequences G0-III, and GIII has been divided into two on the eastern flank. The western flank basin has a sediment thickness ranging from 800m to 1300m with all mega-sequences present. Mega-sequences G0, GI and GII are substantially thicker than GIII, which is assumed to be due to the large sediment input during and before the large glacial periods initiated at 2.3Ma. Within the rift basin, the sediment thickness ranges from 400m to 1350m in thickness, where the western part of the rift basin has a substantially thinner sedimentary cover compared to the eastern part of the rift basin. The thicker units on the eastern part of the rift basin is related to the large input from the glacial era. As only a small portion of the eastern flank is visible on the profile, no apparent traces of the lowermost megasequence G0 have been found, although it is most likely present further east. On the eastern flank, the sediment thickness has a steady increase from 500m to 1000m at the eastern edge of the profile.

When decompacted (Fig 5.9), both burial depth and thickness affect the post-decompaction placement of the units. The two lowermost units interpreted as G0 and GI are modeled to have a original depositional upper boundary up to 150m higher on the western flank, as well as select locations on the eastern flank. Where the units above are substantially thinner, these changes are low or close to none.

Using the figures from the modeled basin (Fig 5.10) as well as the cumulative changes in isostatic rebound (Fig 5.11), it is clear that the basement depth changes are different from line 1. Backstripping the first unit yields very small changes, around 20 m across the entire profile. As this unit is thin across the profile, the isostatic changes are small. Backstripping unit 2 yields larger isostatic changes to the basement. The isostatic rebound is larger below the western flank, as the unit is at its thickest in this area. It ranges from a minimum of 75m, peaking at 90m 16km into the profile. Within the rift basin, the isostatic rebound is around

60m, increasing to 75m at the eastern edge of the profile (Fig 5.10). The sinusoid curve resulting from backstripping unit 3 has a much flatter profile. At both ends of the profile, the isostatic rebound is 105m with a gradual decrease towards the lowest calculated rebound at 36km into the profile, modeled to be 75m. Backstripping the final unit, interpretated as megasequence G0, yields much larger changes in isostatic rebound. While it varies slightly, it fluctuates between 230m at both the western and eastern edge of the profile, and 200m at 30km into the profile (Fig 5.11).
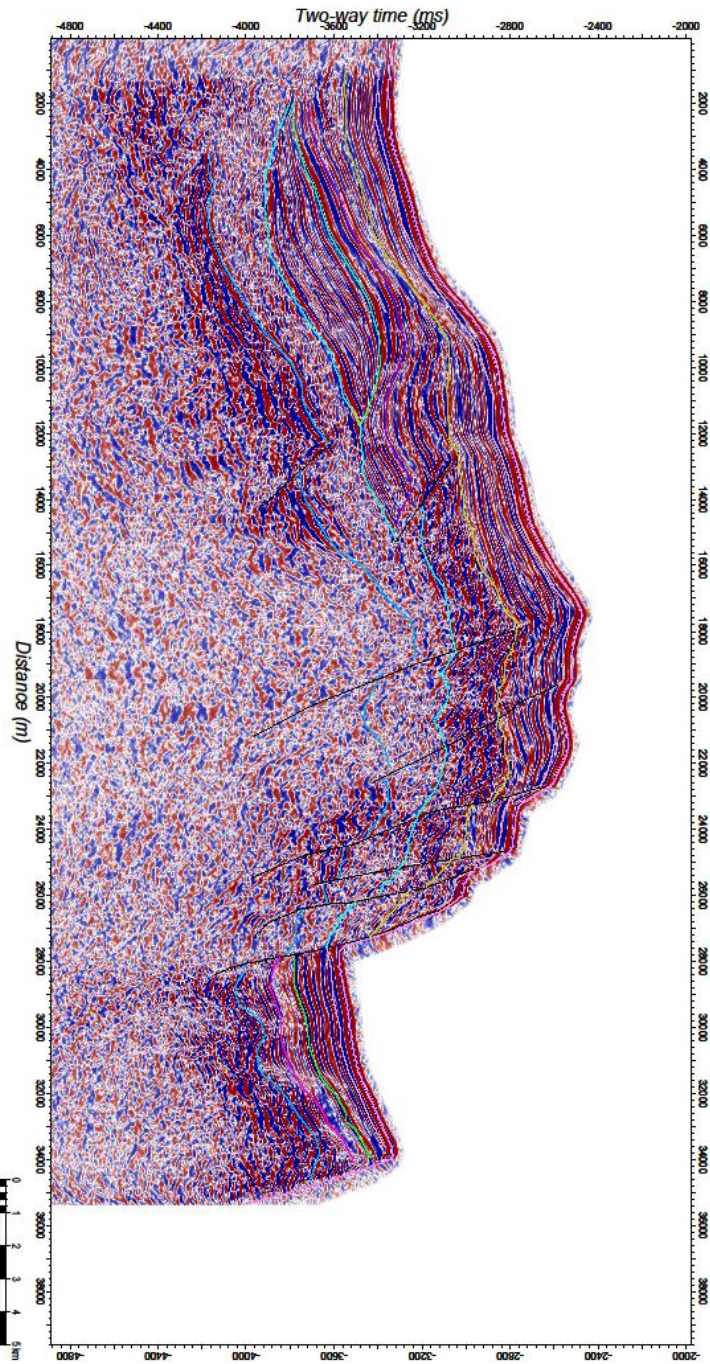
5.2.3 Line 3

Figure 5.12: Line 3 profile from PETREL

Line 3 is the second northernmost of the ESE-WNW – trending lines of the 1999-data. This line only covers the western flank, as well as the ridge crest and a smaller terrace located above and to the west of the rift valley.

Sediment accumulation and seismic interpretation

The structural key aspects of this line (Fig. 5.12) show many comparable features to that of line 2. There is no apparent rift basin ridge with major bathymetrical differences to that of the flank and rift basin. The seafloor has a gradual rise from 3300ms at the western edge of the profile, to around 2500ms at about 17km into the profile. This marks the top of the western ridge. Faulting appears to be generally trending west-east, a difference to that of Line 2.

A total of around 1000ms of sediment accumulations are found on the western flank. These accumulations have been divided into four distinct units. The lowermost unit is mainly chaotic in nature and has a uniform thickness of around 250ms across the western flank. The second lowermost unit is restricted to the western part of the profile. It is shaped as a clinoform, contains well laminated sediments and it is up to 300ms thick. It only has a lateral extent of 10 km, and is by Kvarven (2009) described as a contourite. Unit 3 extends across the entire western flank, but has unlike unit 1 a more variable thickness. Where unit 1 is cut by faults, unit 3 drape across the fault-zones, suggesting that it was deposited either after faulting, or syn-faulting. The unit has a maximum thickness of around 500ms, and it appears well laminated, although it appears more chaotic towards the eastern part of the flank. There, signs of internal faulting or slight rotation of the sediments are present. The upper unit drapes onto of the underlying sediments. It is generally well laminated and has higher amplitude variations. It varies slightly in thickness, from 200ms at the eastern part of the flank to around 400ms at the top of the western ridge.

As for line 2, there is a small terrace above the rift valley. It extends 7 km laterally from the ridge, and has a slight increase in seafloor depth towards the rift basin. 400ms of well laminated sediments cover this part of the profile.

Basin modeling

Unfortunately, modeling line 3 proved non-viable results, as the length of the profile is too short.
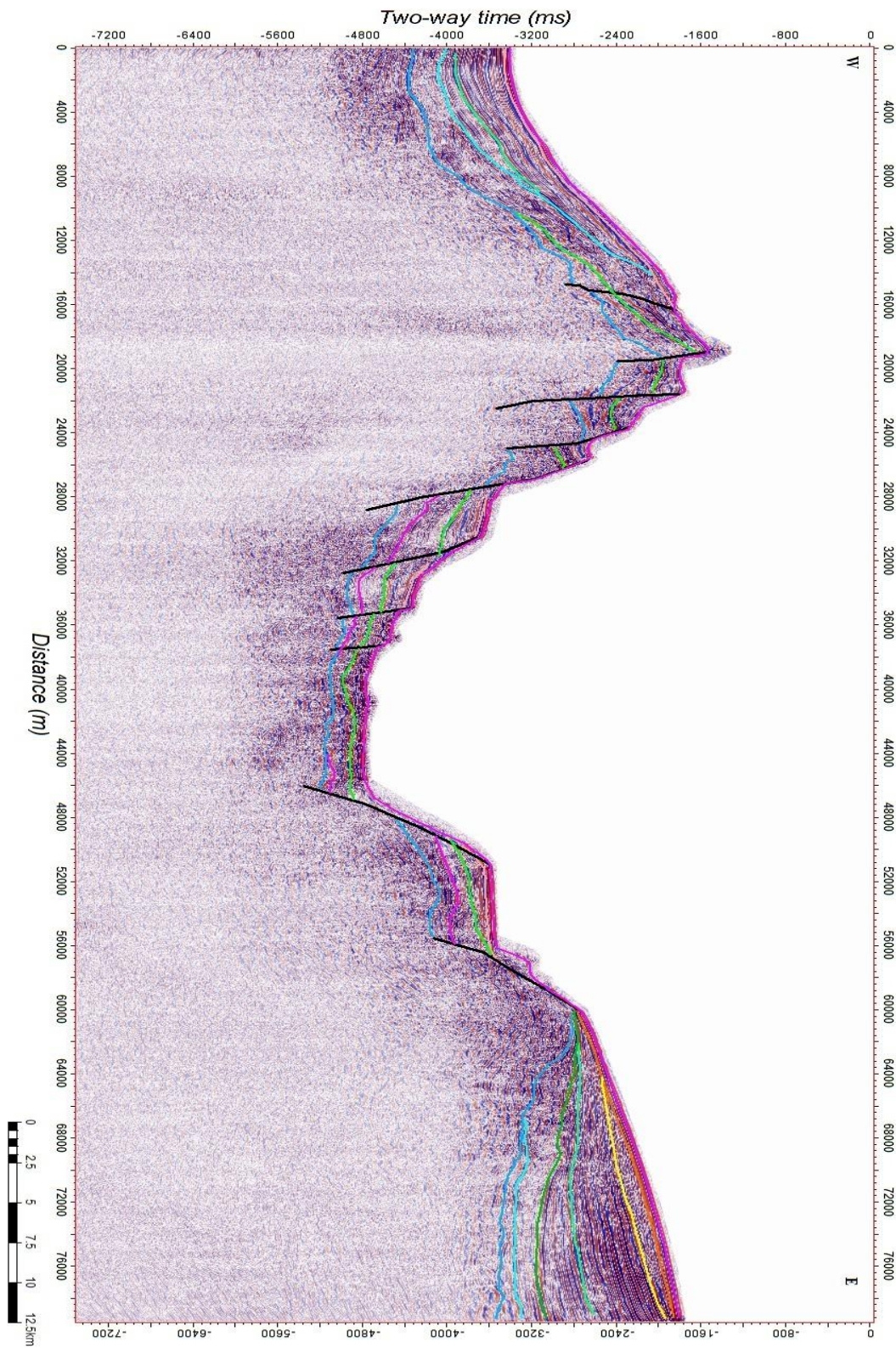
5.2.4 Line 4

Figure 5.13: Line 4 profile from PETREL interpretations

Line 4 is located fourth from north to south of the five ESE-WNW – trending lines from the 1999-data.

Sediment accumulation and seismic interpretation

Line 4 (Fig 5.13) has a distinct ridge crest, giving a rise in bathymetry from 3300ms on the western flank to 1500ms at the ridge apex, 17km into the profile. Several normal faults are found on both sides of this ridge, trending away from the apex. The rift valley seafloor is located at 4700ms, marking a significant change in depth from the western ridge apex. Two normal faults with an offset of 700 and 1500ms are present to the east of the rift valley, creating a small terrace of 5km length, as well as a crest onto which the sediments on the western flank drape onto.

The sediments on the western flank are 1000ms at their thickest. The thickness decreases gradually towards the ridge. Four sedimentary units are found here, where the bottom unit 1 is in majority chaotic and without identifiable reflectors, however with some traces of layering towards the ridge. This unit is uniformly around 400ms thick on the western flank. Units 2-4 all appear well laminated and with similar structures, and pinch out towards the ridge.

The western ridge has around 400ms of sediment cover of similar characteristics to that of unit 1. The sediments are highly distorted with discontinuous reflectors present. This may be due to the tectonic activity in the area, promoting gravity flows.

On the western edge of the rift basin, there are several smaller terraces, faulted downwards. A total of five terraces are found, separated by large offset normal faults, of which the upper three has sediments with characteristics to that of the ridge apex sediment cover; i.e. no form of division into units is possible. The lower two terraces are different from the upper three. Three distinct units are interpreted here. As with the other seismic lines crossing the rift valley, these units have large resemblance to those on the terrace on the eastern side of the rift basin. The lowermost unit has undulating reflectors with large variations in amplitude. Above is a unit with no apparent reflectors present. This transparent unit has very low amplitude levels, pointing to low variations in acoustic impedance. The upper unit has more distinct layering, and has variations in thickness from 400ms to 50ms.

The rift basin itself has only high-amplitude reflectors present. Deciphering the basement reflector is difficult, but it is assumed that the sediment cover is around 500ms.

The eastern flank has sediment cover with characteristics to that of the other lines. Basement is interpreted to be at 2750ms at the edge of the flank shelf, forming a half-parabolic shape further to the east. This leads to a large variation in sediment thickness. At the shelf edge, this thickness is only 50ms, growing thicker closer to the edge of the profile, where the sediment thickness is 1900ms. The two lowermost of the six units interpreted here are chaotic or transparent. These are suggested by Kvarven (2009) to be of pre-glacial or gravity driven origins. The uppermost four units all have well defined layering, with the exception of the second uppermost layer, which has slightly more chaotic characteristics. Units 1, 3 and 4 are assumed to be of glacial marine and hemi-pelagic origins, while unit 2 with more chaotic structures could be of gravity driven origins, such as turbidites and subsea slides or slumping.

Basin Modelling
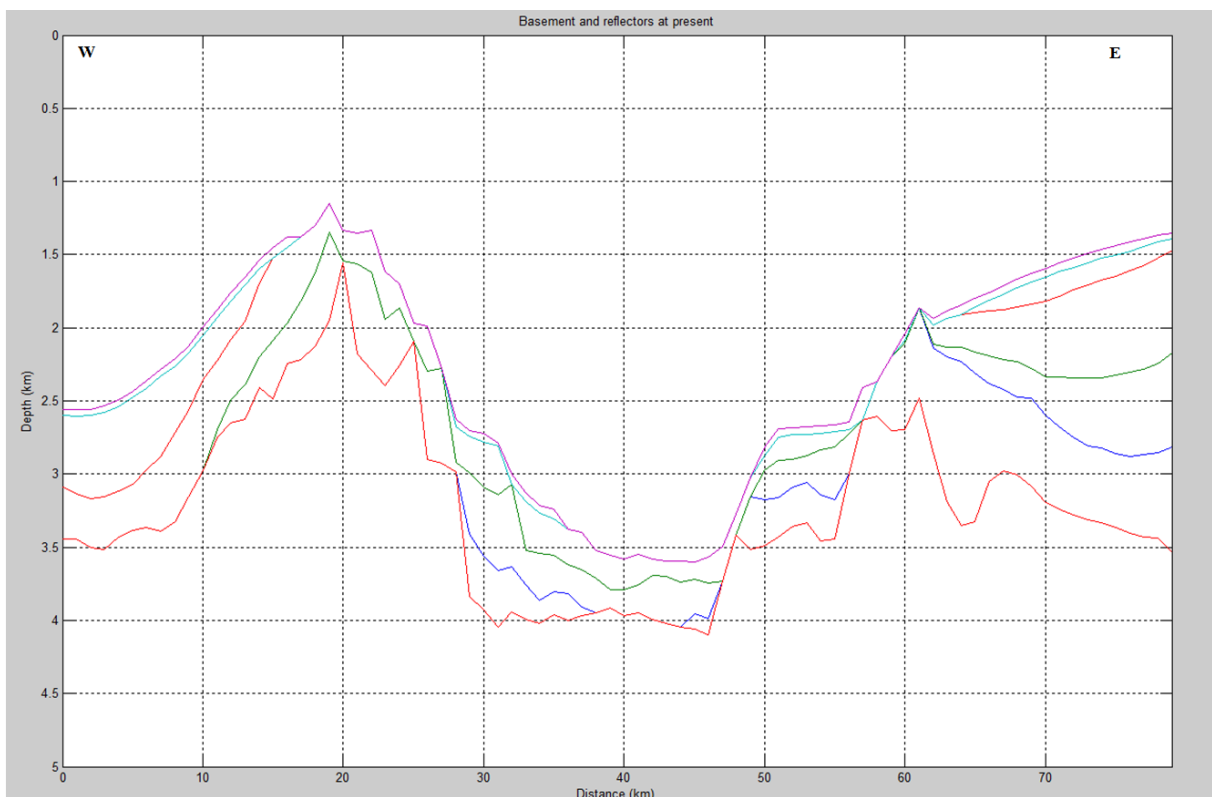
Figure 5.14: Line 4 depth-converted from TWT. Picked at 1km intervals. Velocities are taken from Faleide et al. (1996), Ljones et al. (2004) and Kandilarov et al. (2008).
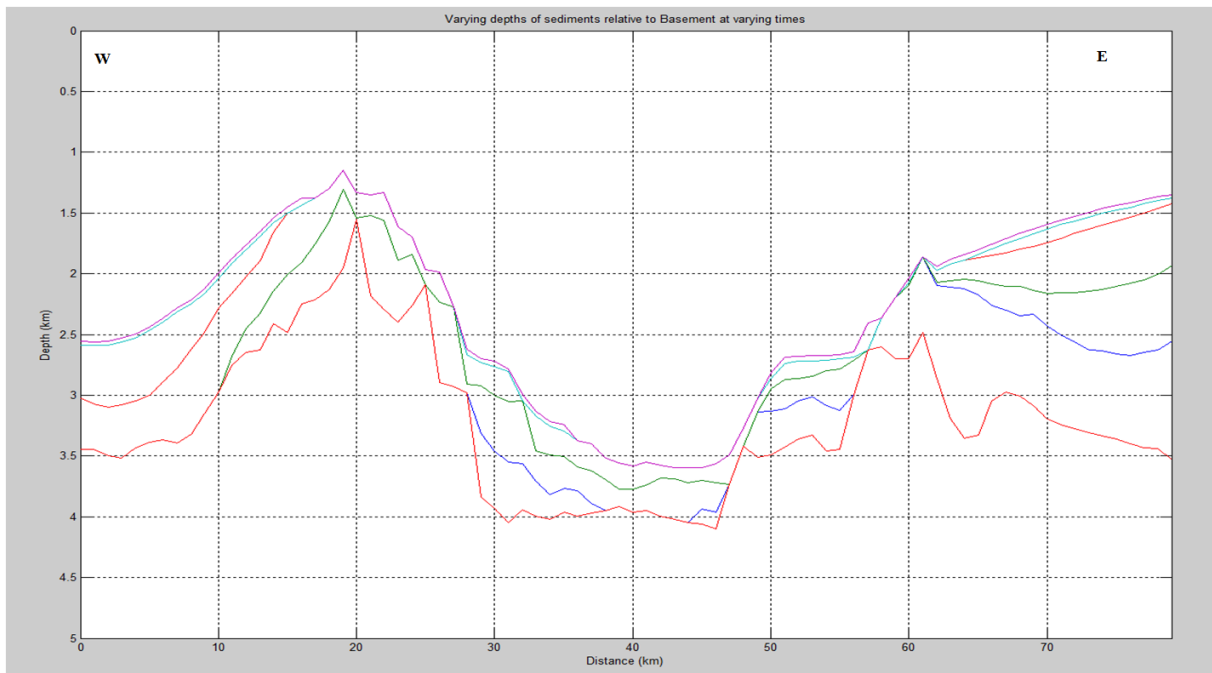
Figure 5.15: Decompacted sediment units from line 4
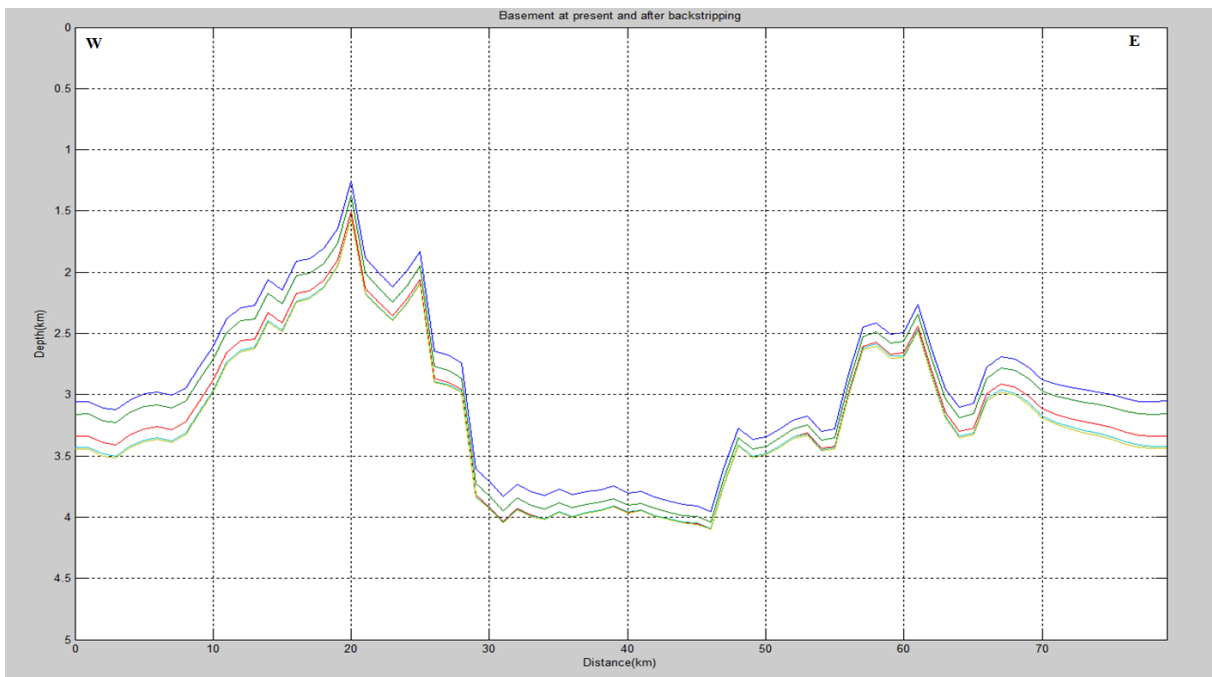
Figure 5.16: Basement modeled after removal of successive sedimentary units for line 4. The bottom, yellow line is the original basement depth, lime green is basement depth with the first sedimentary unit backstripped, red is basement depth with the second sedimentary unit backstripped, dark green is basement with the third unit backstripped and the blue line is the final basement depth with all sedimentary units backstripped.
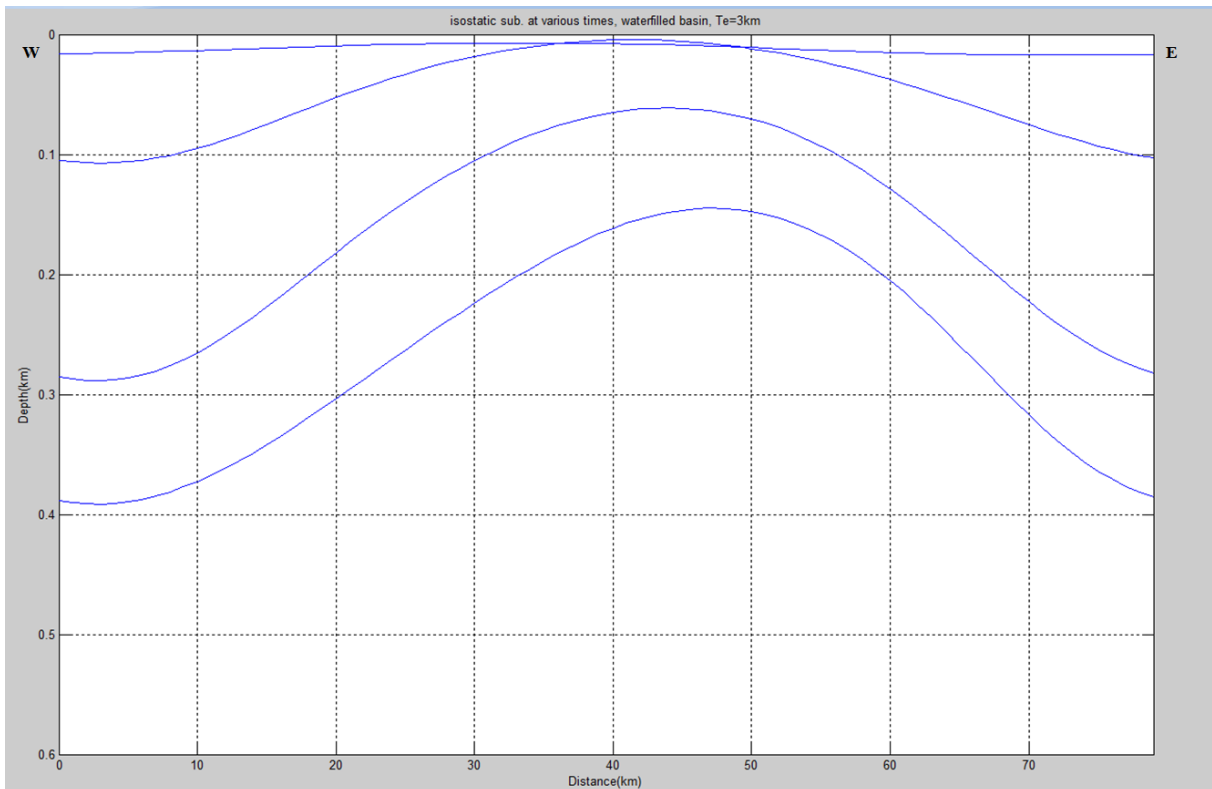
Figure 5.17: Modeled basement depth Δd, cumulative changes in basement depth after backstripping for line 4. The upper line is the change in basement depth with one sedimentary unit backstripped, the second and third lines show the change in basement with two and three units backstripped respectively. The lowermost line is the total change in basement depth with all sedimentary units backstripped.

Using the PETREL-data, twt-traveltimes are extracted and compiled into a datasheet. These times are converted to depth (Fig. 5.14) using the average seismic P-wave velocity compiled in previous studies. The data are then processed in Matlab to yield a modeled basement with no sediment cover. Faults are treated as static basement.

On this profile (Fig 5.14), the sedimentary cover is divided into five units. A fit to the megasequences has been attempted. The sedimentary cover is thick on both the western and eastern flanks of the pofile. On the western flank, the thickness of sediments is between 800m and 1000m, where the older megasequences are substantially thicker than the younger. At the ridge apex, the sediment thickness is estimated to be around 400m increasing to 1200m in the western slope of the rift basin. Towards the eastern part of the rift basin, the sedimentary thickness decreases to between 400-500m. As noted in the models, a large wedge-shaped unit is present within the rift basin. This is likely debris from gravitational mass movements from the western ridge.

55

After decompacting all units (Fig. 5.15), the model shows that the deeper buried older units have larger changes in original deposited depth. Units modeled as the oldest megasequences G0 and GI show changes of up to 100m shallower original depositional depth on the western flank and 200m on the eastern flank towards the edge of the profile. As with the younger units, buried under little or no sedimentary load, the compaction of these are to a lesser extent, and so the current thickness is comparable to the original depositional thickness and depth.

The modeled basement (Fig. 5.16) is shown after successive back-stripping of each sedimentary unit, using an elastic thickness of 3km. The lowermost interface is the basement at present day, while the interfaces above show changes to basement depth when sedimentary units are successively removed. Figure 5.17 contains the total isostatic rebound when a sedimentary unit is backstripped. Backstripping the first unit yields small changes to the basement depth. The isostatic rebound is around 20m throughout the profile. However, when backstripping unit 2, an estimation of megasequence GII, the isostatic rebound is up to 100m at both the western and eastern ends of the profile. This also has a negative effect to the backstripping of the first unit. This is likely due to the flexure of the oceanic crust and the removal of loads on each rift flank basin. A sinusoid shaped curve is the result of the total isostatic rebound thus far. Within the rift basin, this rebound is negative compared to backstripping the first unit and is now less than 10m. Backstripping the third unit, comparable to megasequence GI, yields a curve similar to that of the former backstripped unit, although with a larger rate of isostatic rebound. At both ends of the profile, this rebound is close to 280m. Within the rift basin, a smaller value is calculated at 65m. Backstripping the final unit yields a further isostatic rebound, modeled to be 380m at both the western and eastern edge of the profile. The variations in isostatic rebond is shaped like a sinusoid curve, with peaks at the edges of the profile, and a lower calculated rebound at 47km into the profile. This is in the middle of the rift basin. This is related to the thinner deposits within the rift basin.

5.2.5 Line 5
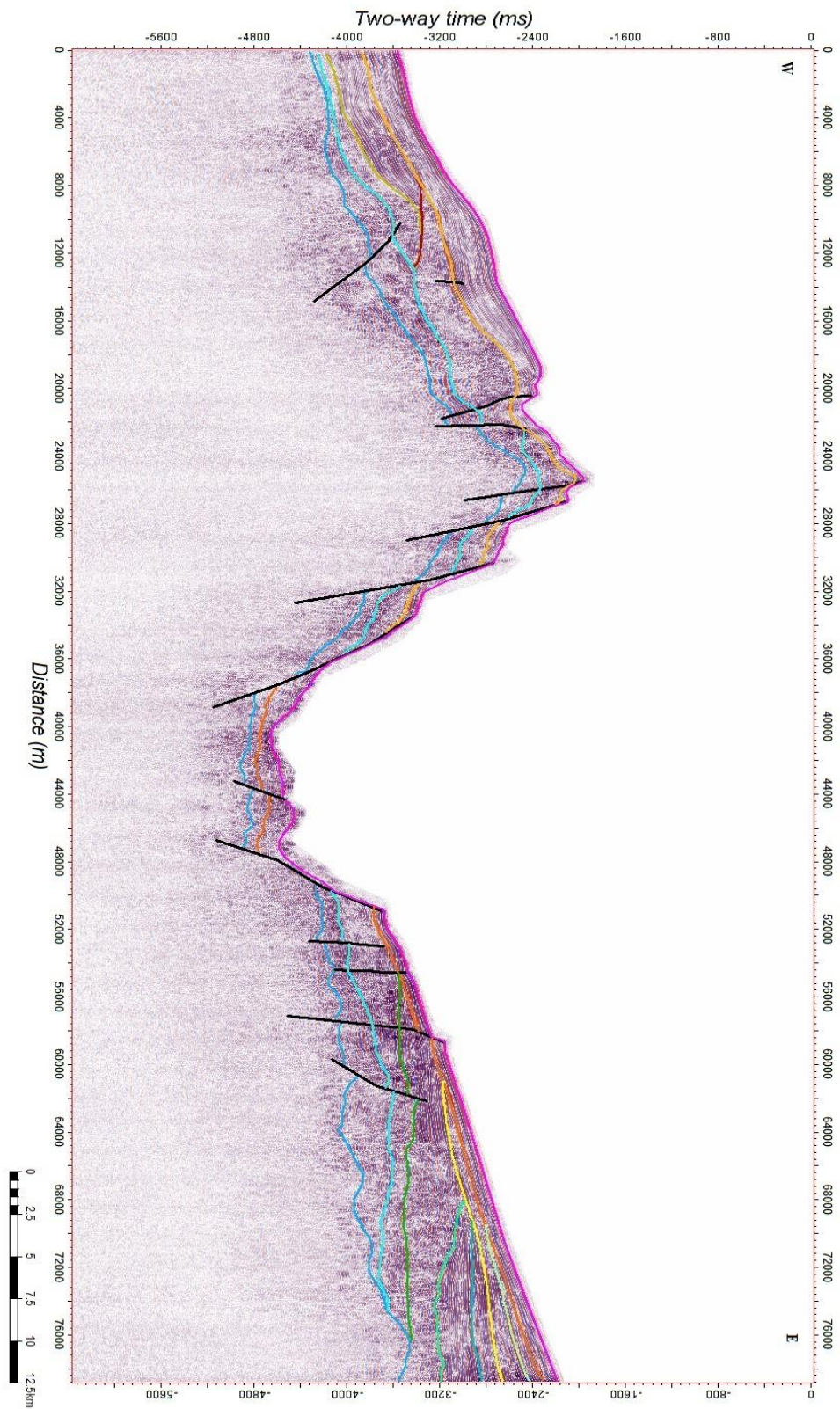
Figure 5.18: Interpreted PETREL profile for line 5

Line 5 (Fig. 5.18) is the southernmost of the five ESE-WNW – trending lines from the 1999-data.

Sediment accumulation and seismic interpretation

Basement in this line has many similarities to that of line 4. The western ridge has a lower relief by comparison, but it is lower than that of line 1. The change in depth is gradual and close to linear from the edge of the profile to the ridge apex, decreasing from 4200ms to 2500ms. Few faults are found creating heave in the basement. The few present are normal faults having less than 200ms heave and trending both westwards and eastwards. From the ridge apex to the rift basin itself, four normal faults trending east create a total difference in basement depth of 2250ms. The rift basin basement is relatively flat, but discerning the depth is difficult. A large fault separates the rift basin from the eastern flank, where the basement has a relatively linear increase in two-way-time depth from 4200ms to 3500ms. Although a few westward trending normal faults are present on the eastern flank, it is highly possible that there are more. Weak and indiscernible reflectors below 1500ms of sediment cover is the primary cause.

On the western flank, the sedimentary thickness is between 1000ms and 750ms. The sediments are divided into five units. The lowermost unit 1 has high amplitude variations, but is otherwise chaotic. The second lowermost unit 2 has the same chaotic characteristics to that of unit 1, but it expresses a less prominent internal amplitude variation, as well as undulating reflectors. Unit 2 is chaotic in its internal structure, and is buried under units 3 and 4. The two upper units 4 and 5 are well laminated and homogenous in thickness. An important observation is the way units 2 and 3 are cut by unit 4 (Fig. 5.18). Unit 3 and 4 have a lateral extension of only 10km, and are assumed to be buried drift-structures by Kvarven (2009). Another explanation is gravity-movements, however this is unlikely due to the geological structure around this unit, as well as the well preserved internal structures within this unit. Unit 5 is, with its well laminated and homogenous structures, assumed to be of hemi-pelagic origins. A small graben is found at 20km into the profile. This could be a tectonic event, causing unit 4 tp overlap unit 2 and 3. The ridge apex carries around 500ms of sedimentary cover, consisting of units 1, 2 and 5. Its apex is at a depth of 1900ms TWT, which is around 1400m by using 1.48 km/s as the sonic speed in seawater.

The western rift basin flank from the ridge apex to the rift basin itself has two terraces with sedimentary cover, offset by eastward trending normal faults with around 600-700ms heave. While discerning both basement and sedimentary boundaries is difficult, it appears that these terraces have similar sedimentary units to that of the ridge apex itself. The internal structures appear to be mostly intact, pointing to post-depositional faulting.

The rift basin is interpreted to have a sedimentary cover varying between 500ms and 300ms. Due to the high levels of noise present near the basement, discerning both the basement and sedimentary boundaries is difficult.

On the eastern flank, the sedimentary accumulation is higher, ranging from 500ms close to the rift basin, to a thickness of 1300ms at the eastern edge of the profile. A total of eight units have been interpreted here. These are related either to pre-glacial, syn-glacial or post-glacial sedimentation. The units are numbered from the lowermost. Unit 1 is continuous throughout most of the eastern flank, varying in thickness up to 300ms. Faleide et al. (1996) defines this unit as a pre-glacial mega-sequence G0, deposited before the start of the last glacial periods starting at 2.5Ma. The boundary defining the start of the glacial periods could both be at the top of unit 1 and 2, as these two units have similar characteristics; undulating and at times chaotic and distorted reflectors. However, Faleide et al. (1996) interpretes unit 2 to be of glacial origins, deposited after the initiation of the last glacial periods. This is supported by Kvarven (2009). Unit 3 has some characteristics shared with the two underlying units, and could possibly be merged with unit 2. However, it has a more defined lamination and its internal structures are better preserved than that of unit 2. Units 2 and 3 are by Faleide et al. (1996) defined as mega-sequence GI, deposited before the rise in sedimentary influx at 1Ma. Units 4, 5, 6 and 7 have similar geological features. They are well laminated, and are confined to the eastern parts of the flank. Unit 6 appears to represent the upper erosional contact for units 4 and 5, and it has a larger lateral extent than the ~10km observed for units 4, 5 and 7. These units are defined by Faleide et al. (1996) to be mega-sequence GII, deposited between 1 - 0.44Ma. Unit 8 is draped on top of all units on the flank. This unit is most likely of hemi-pelagic origin, deposited after mega-sequence GII.

Basin Modeling
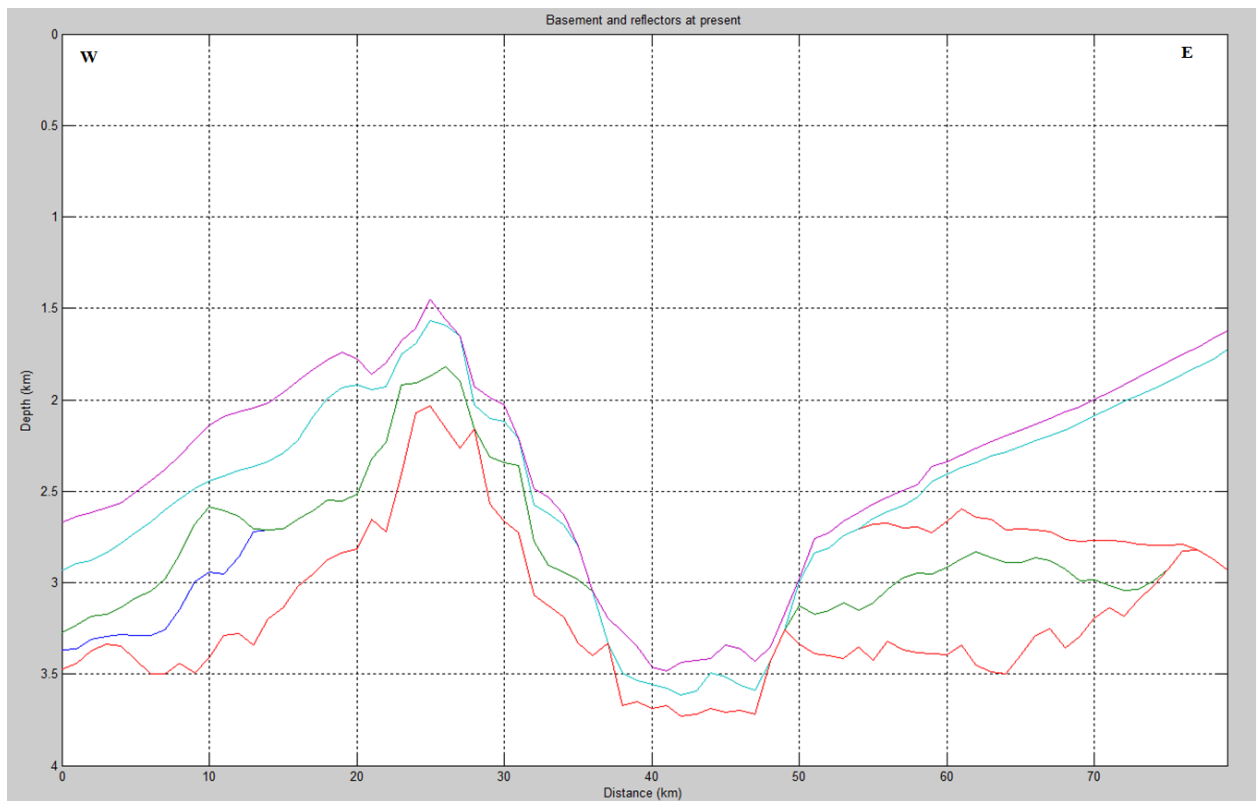
Figure 5.19: Depthconverted from TWT line 5 picked with 1km intervals. Velocities are taken from Faleide et al. (1996), Ljones et al. (2004) and Kandilarov et al. (2008).
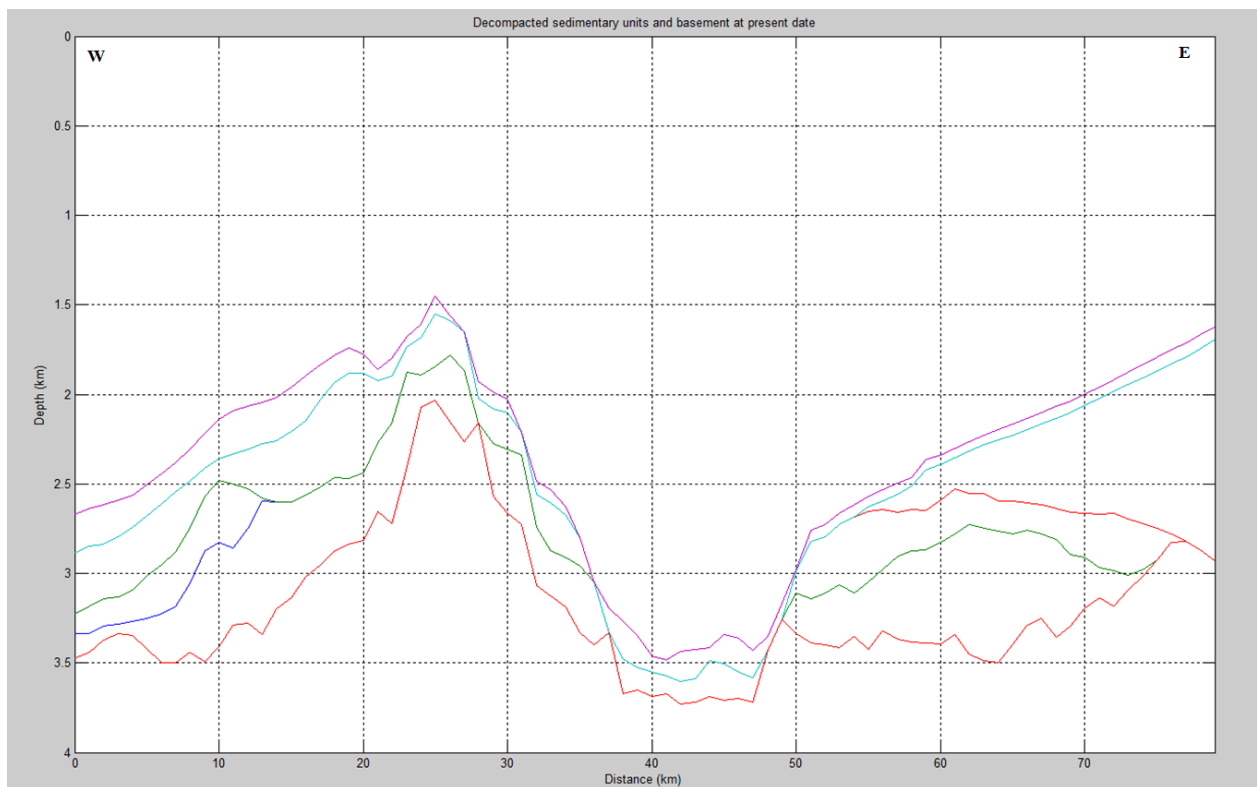
Fig 5.20: Line 5 with all sedimentary units decompacted
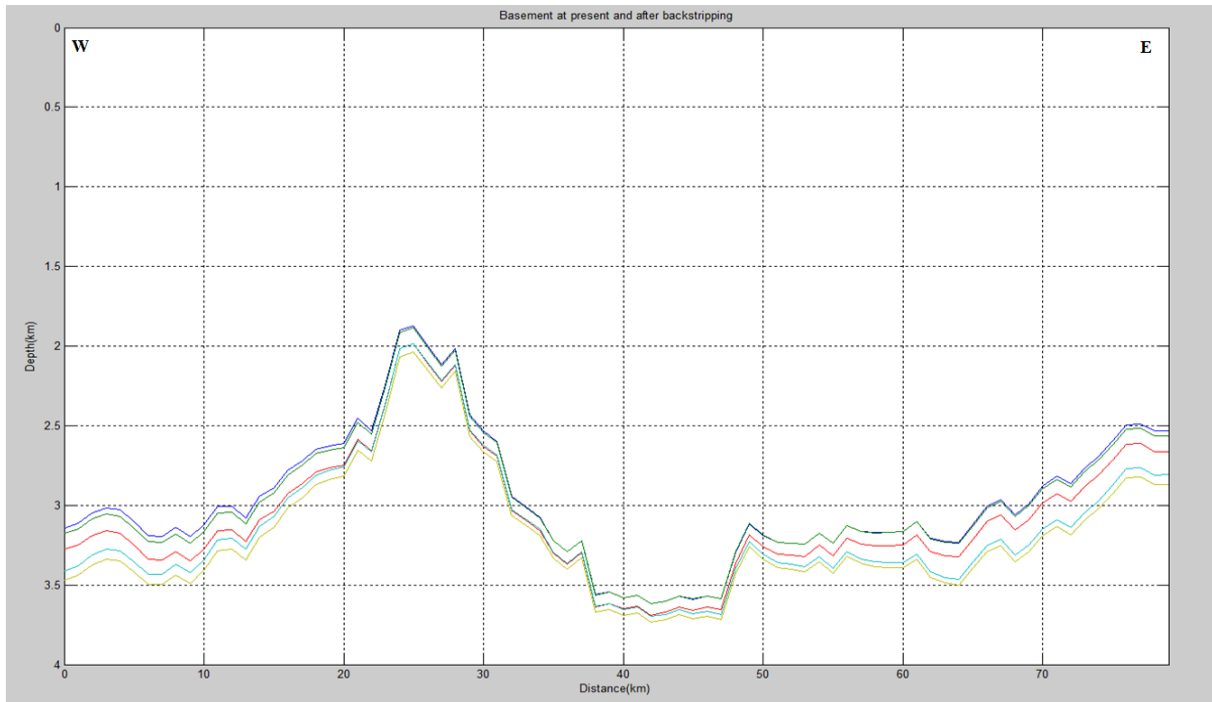
Figure 5.21: Basement modeled after removal of successive sedimentary units for line 5. The bottom, yellow line is the original basement depth, lime green is basement depth with the first sedimentary unit backstripped, red is basement depth with the second sedimentary unit backstripped, dark green is basement with the third unit backstripped and the blue line is the final basement depth with all sedimentary units removed
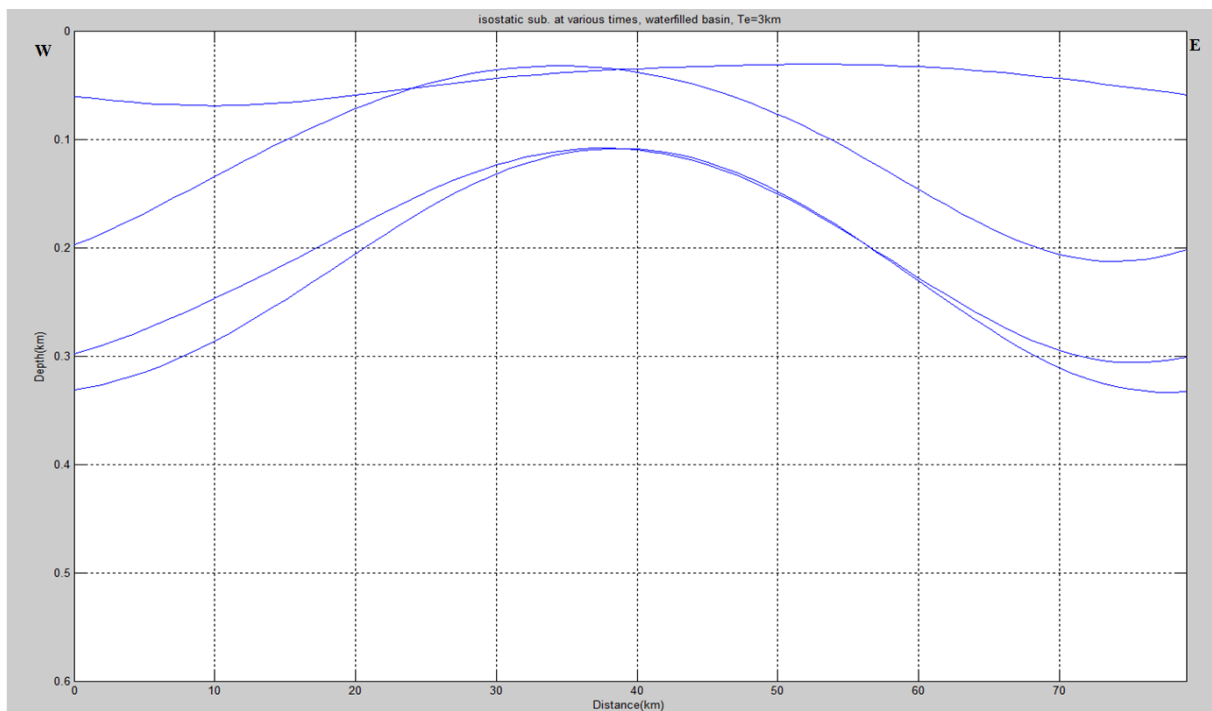
Figure 5.22: Modeled basement depth Δd, isostatic rebound after backstripping for line 5. The upper line is the change in basement depth with one sedimentary unit backstripped, the second and third lines show the change in basement with two and three units backstripped respectively. The lowermost line is the total change in basement depth with all sedimentary units backstripped.

Using the PETREL-data, twt-traveltimes are extracted and compiled into a datasheet. These times are depthconverted (Fig. 5.19) using the average seismic P-wave velocity compiled in previous studies (Faleide et al., 1996, Ljones et al., 2004 and Kandilarov et al., 2008). The data are then processed in Matlab to yield a modeled basement with no sediment cover. Faults are treated as static basement, and basement has a fixed elastic thickness *Te* of 3km.

When depthconverted, the profile yields thick sediment accumulations on both the eastern and western flank basins. They are attempted classified into the four megasequences where the two lowermost units are G0, the third unit is GI, the fourth and fifth units are GII and GIII respectively. On the western flank, it ranges from 800m to 1300m in thickness. Past 20km into the profile, the sedimentary thickness is reduced to 400m to 700m in thickness on the western ridge crest and rift basin. From 50km into the profile, the eastern flank basin is found, with sediment accumulations of 1000m to 1350m. As expected, the deeper and thicker decompacted units show a larger change in original depositional depth of up to 175m at the thickest parts of the profile (Fig. 5.20).

Backstripping each unit successively yields curves of basement (Fig. 5.21). The lowermost interface is the basement at present day, while the interfaces above showe changes to basement depth when sedimentary units are successively removed. The total isostatic rebound is shown in Figure 5.22. Backstripping the fifth and upper unit, estimated to be megasequence GIII yields a small isostatic rebound of 50m +/- 20m. It is relatively homogenous, although smaller within the rift basin. Further backstripping of the fourth unit yields an isostatic rebound of 200m at both the western and eastern flank basins. At 35km into the profile, the isostatic rebound is less than 40m. The thinner sedimentary accumulation within the rift basin is the cause of the lower isostatic rebound. Due to the backstripping of thick sediment accumulations on both flanks, the isostatic rebound within the rift basin is at times negative. When the third unit is backstripped, the result is 300m cumulative isostatic rebound at both ends of the profile. Within the rift basin this value is smaller, around 115m at its lowest value. A complete backstrip yields a basement rebound of up to 330m within the eastern and western flank basins, and a lower value of 115m within the rift basin.

5.2.5   Line 7a
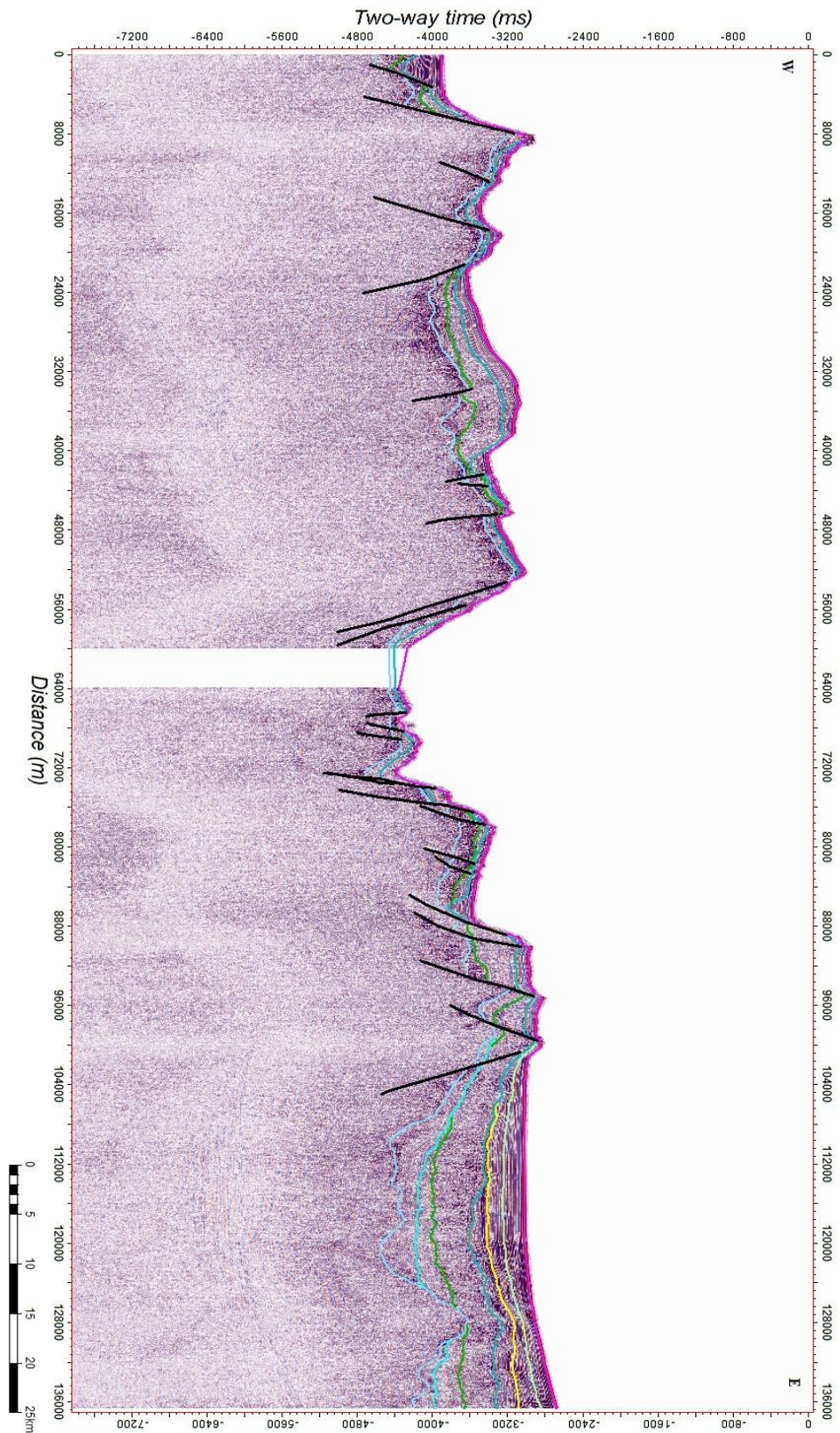
Figure 5.23: Interpreted PETREL profile for line 7.

Line 7a is the southernmost of the five ESE-WNW – trending lines from the 1999-data. It has no lines crossing or tying it to the grid of lines further north. It was acquired paralell to the other lines, but it is located 150km further south at the mouth of Bellsundet.

Sediment accumulation and seismic interpretation

The basement in line 7a (Fig 5.23) has little resemblance to that of the southernmost lines in the grid further north. On the other hand, it shares characteristics with the northernmost lines, having no prominent rift basin flank apex with a large relief. No point on the ridge flanks is located above 3000ms. Only the eastern flank basin has a TWT depth of less than 3000ms, although it is relatively flat at about 2700ms. Faulting is prominent throughout the profile and with few exceptions, the faults are normal faults. The majority are trending towards the rift basin, although a few large offset faults located around 50km to the west of the rift basin trend away from the rift axis. At the start of the profile, parts of a basin is found. The basement is interpreted to be located at 3600ms TWT. Two faults create a small peak in bathymetry, at its apex basement is located at 3200ms. Between 8km and 53km into the profile, a relatively flat basin is found. Faults with less than 300ms heave create horst and graben structures. The depth of the basement varies between 3500ms and 4000ms within this part of the profile, with a gradual rise to 3200ms at the ridge crest apex. At the edge of the rift axis basin, two faults with a combined heave of 1400ms are found. The basement is interpreted to be located at around 4600ms within the rift axis basin. Several faults trending westward are present on the western flank of the rift axis basin. These create a slightly rotated terrace with a basement depth of around 3800ms. A horst about 100km into the profile mark the start of a deeper sedimentary basin on the eastern flank. The basement varies in depth, reaching 4600ms at its deepest.

At the westernmost basin, 700ms of sediment cover is found. While the extent of this basin is small, it is expected that it is the edge of a larger sedimentary basin stretching further westwards. Three distinct units are found here. The lowermost unit 1 is characterized by strong, but undulating and chaotic reflectors. Unit 2 is more transparent than unit 1, but is also chaotic, although with traces of internal structures. This could be a result of gravity movements, conserving some of the internal lamination. Unit 3 is very well laminated and drapes onto unit 2. It is assumed to be of hemi-pelagic origins. An important observation is the increased unit thickness at the start of the basin found to the far west. This could be a

result of this unit being deposited post-faulting, where oceanic drifts deposit sediments into the calmer, deeper parts of rotated fault blocks. Units 1 and 2 appear to have the same thickness and lie concordant on top of the basement. Only 200ms to 300ms of sediments cover the bathymetric high between 8 and 22 km into the profile. These sediments are divided into two units, the upper having well laminated structures, while the lower being more distorted and chaotic. A small basin is present between 22 and 52 km into the profile. There, 300ms to 500ms of sedimentary accumulation is present, with the three units having similar characteristics to that of the far western basin. The two lower units have distorted and chaotic reflectors, an the upper unit has more laminated structure. The rift axis basin carries around 400ms of sediments. Apart from the uppermost 50ms thick top unit, the reflectors are highly distorted, most likely due to the faults present, causing diffraction, as well as the generally distorted sedimentary deposits.

The eastern flank terraces carry sediments with properties similar to the basin on the western flank. They vary in thickness between 300ms and 600ms and appear to be slightly rotated, most likely due to the faulting in this area. The eastern flank basin carries a significantly thicker load of sediments. It ranges between 900ms and 1500ms at its thickest. These sedimentary accumulations are divided into six units. The two lowermost units 1 and 2 are highly distorted, but have reflectors with strongly varying amplitude present. Unit 2 contains a more distinct internal layering than that of unit 1. These two units drape the basement of the basin. Unit 1 is most likely mega-sequence G0, deposited before the start of the last large glacial periods. While the basement has a large variation in depth, the upper boundary of unit 2 has a more planar surface. Unit 3 has characteristics similar to that of units 1 and 2, but expresses less traces of reflectors and internal structuring. It is 400ms thick throughout the basin and drapes onto units 1 and 2. Units 2 and 3 are assumed to be mega-sequence G1, deposited at the start of the last glacial periods, up to 1Ma. Units 4 and 5 drape onto unit 3, pinching out towards the west and increasing in thickness towards the east. These units are well laminated and are most likely of glacio-marine origin. The units most likely belong to mega-sequence GII deposited between 1 - 0.44Ma. At the top, unit 6 is found, representing a well laminated and continuous unit. It is interpreted to be of hemi-pelagic origin, deposited as mega-sequence GIII after 0.44Ma.

Basin Modeling

65
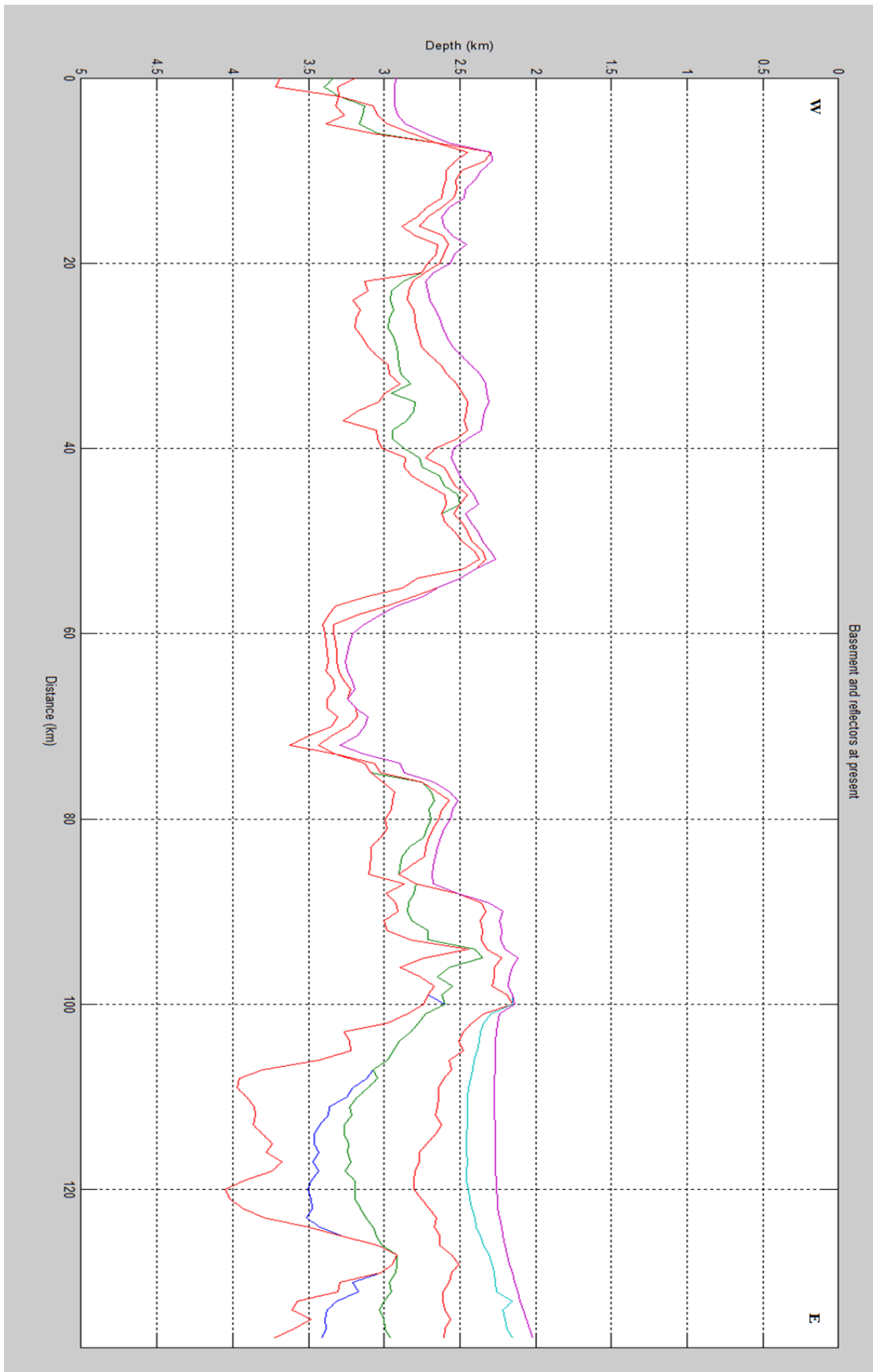
Figure 5.24: Depth-converted from TWT line 7a picked with 1km intervals Velocities are taken from Faleide et al. (1996), Ljones et al. (2004) and Kandilarov et al. (2008).
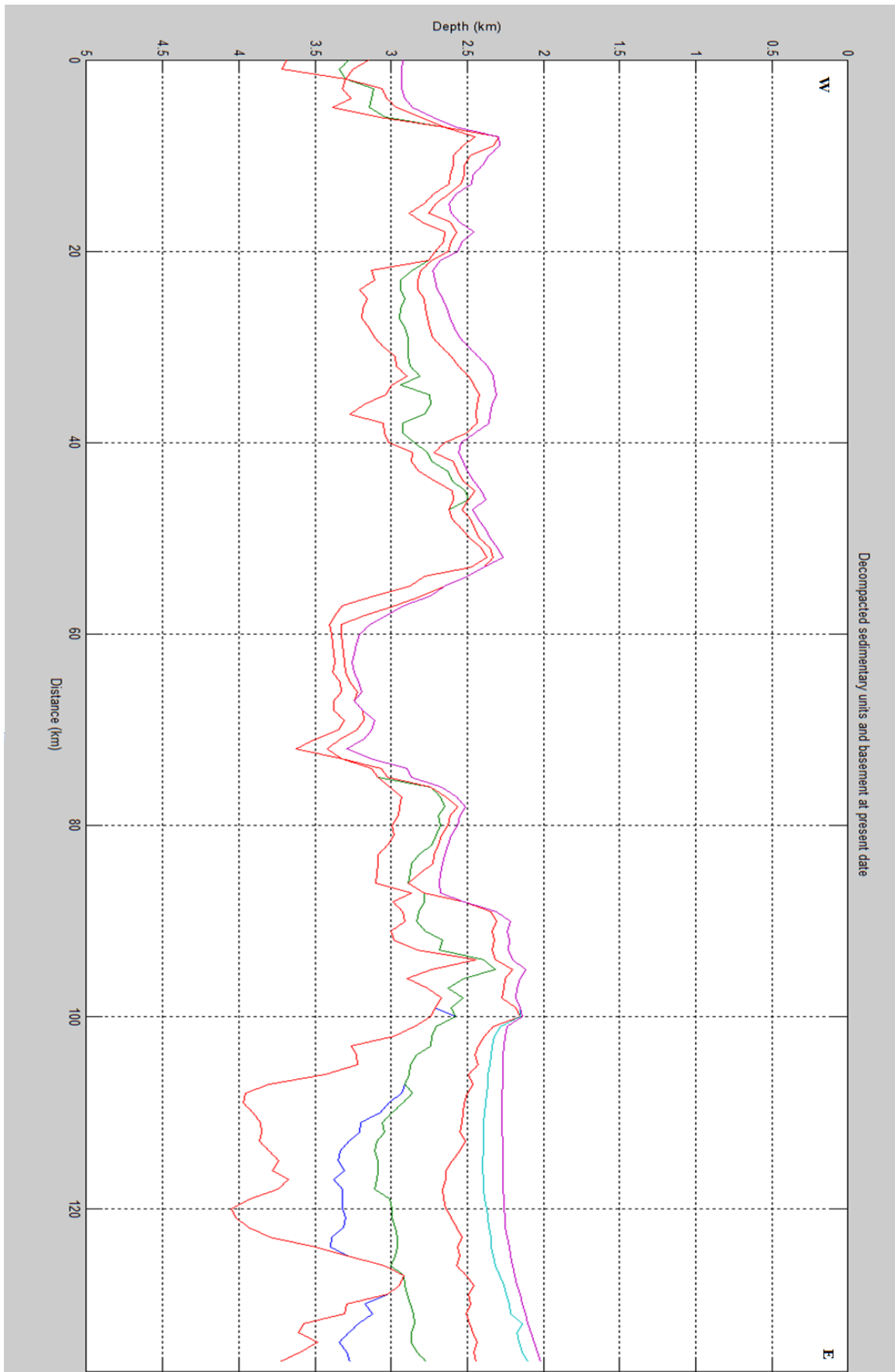
Figure 5.25: Line 7a with all sedimentary units decompacted.
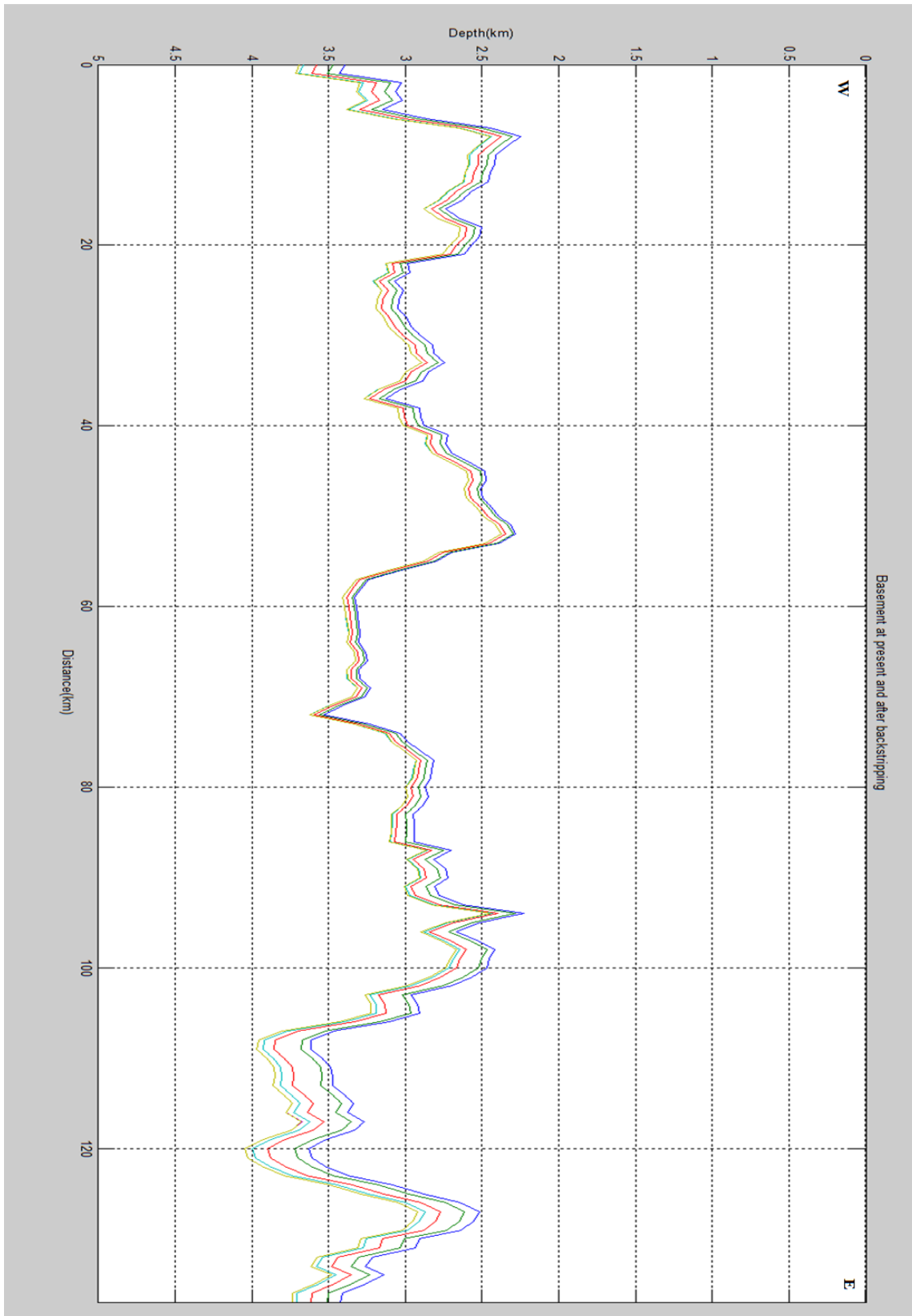
Figure 5.26: Basement modeled after removal of successive sedimentary units for line 7a. The bottom, yellow line is the original basement depth, lime green is basement depth with the first sedimentary unit backstripped, red is basement depth with the second sedimentary unit backstripped, dark green is basement with the third unit backstripped and the blue line is the final basement depth with all sedimentary units backstripped.
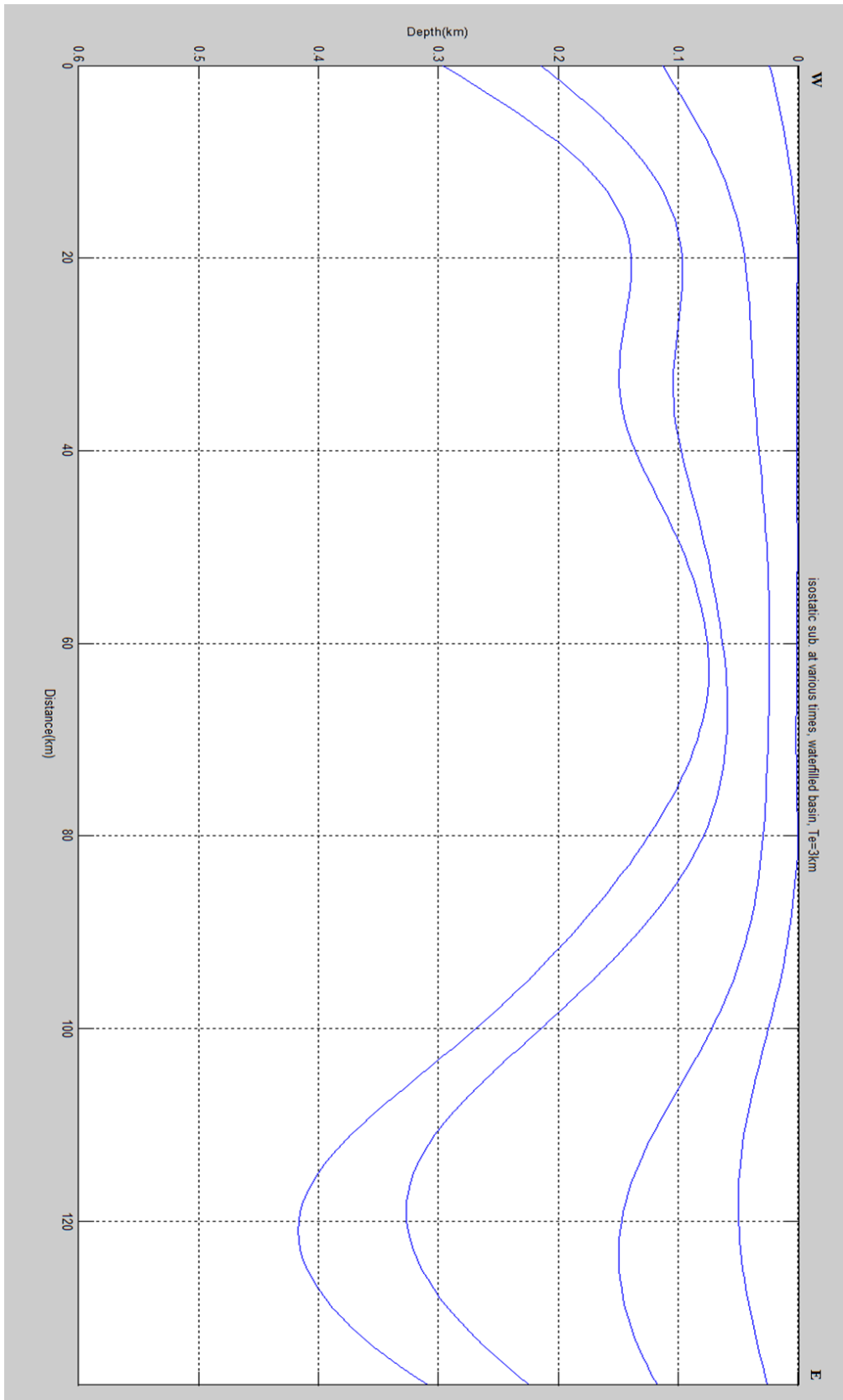
Figure 5.27: Modeled basement depth Δd, isostatic rebound after backstripping for line 7a. The upper line is the change in basement depth with one sedimentary unit backstripped, the second and third lines show the change in basement with two and three units backstripped respectively. The lowermost line is the total change in basement depth with all sedimentary units backstripped.

69

Using the PETREL-data, twt-traveltimes are extracted and compiled into a datasheet. These times are converted to depth (Fig. 5.24) using the average seismic P-wave velocity compiled in previous studies (Faleide et al., 1996, Ljones et al., 2004 and Kandilarov et al., 2008). The data are then modeled to yield a modeled basement with no sediment cover. Faults are treated as static basement. Dividing the units into the megasequences G0-GIII is attempted. The depthconverted profile has several sedimentary basins on the western flank. At the edge of the profile, a sedimentary thickness of between 500-800m is calculated. The sedimentary basin from 20 to 40km into the profile also has substantial sedimentary cover, between 500-1000m. The western ridge crest as well as inside the rift basin, only a calculated sedimentary thickness of 200-300m is found. There are two smaller terraces to the east of the rift basin, carrying around 500m of sediment, while the eastern flank basin has a substantial sedimentary cover. Is calculated thickness is up to 1800m thick. When decompacted (Fig. 5.25), There are only smaller changes of less than 50m to the original depositional thickness and depth, apart from the eastern flank basin. The deeper, older units have an original depositional depth of up to 220m higher than the calculated present depth.

The modeled basement (Fig. 5.26) is shown after successive back-stripping of each sedimentary unit. The lowermost interface is the basement at present day, while the interfaces above show changes to basement depth when sedimentary units are successively backstripped. Figure 5.27 show the total isostatic rebound when sedimentary units are backstripped. As this profile is substantially longer compared to the other lines of the 1999-dataset, the calculated basement and isostatic rebound is different from the other lines. The sinusoid graphs of isostatic rebound are no longer found. There are clear similarities to the other profiles however. The isostatic rebound is substantially larger at both ends of the profile, while being lower closer to and within the rift basin. This also shows on the modeled basement after backstripping (Fig. 5.26). Backstripping the first unit, estimated to be megasequence GIII, result in minor changes in isostasy. The rebound is only around 25m at the western edge of the profile, while being 50m within the eastern flank basin. The change in the middle of the profile is negligible. Backstripping the estimated GII result in a isostatic rebound of 115m at the western edge of the profile, around 30-40m in the middle basin and rift axis, and up to 150m at the eastern flank basin. When the estimated megasequence GI is backstripped, the isostatic rebound is substantial. At the western edge of the profile, it is calculated to be up to 215m, 100m within the middle basin at 30km into the profile, 60m at the rift axis and up to 330m at the eastern flank basin. The complete backstrip yields the final

isostatic rebound of the basement. It is 290m at the western edge of the profile, 150m at the middle basin, as low as 75m at the rift axis and up to 425m at the eastern flank basin. While the other profiles show good modeled results, this profile is important due to the length compared to the others. As the modeling limits the sediments to within the profiles, but calculates with a limitless simulation of the crust, a longer profile yields better results. This will be discussed further in the next chapter.

5.3   2004 - Data

5.3.1   Line 24
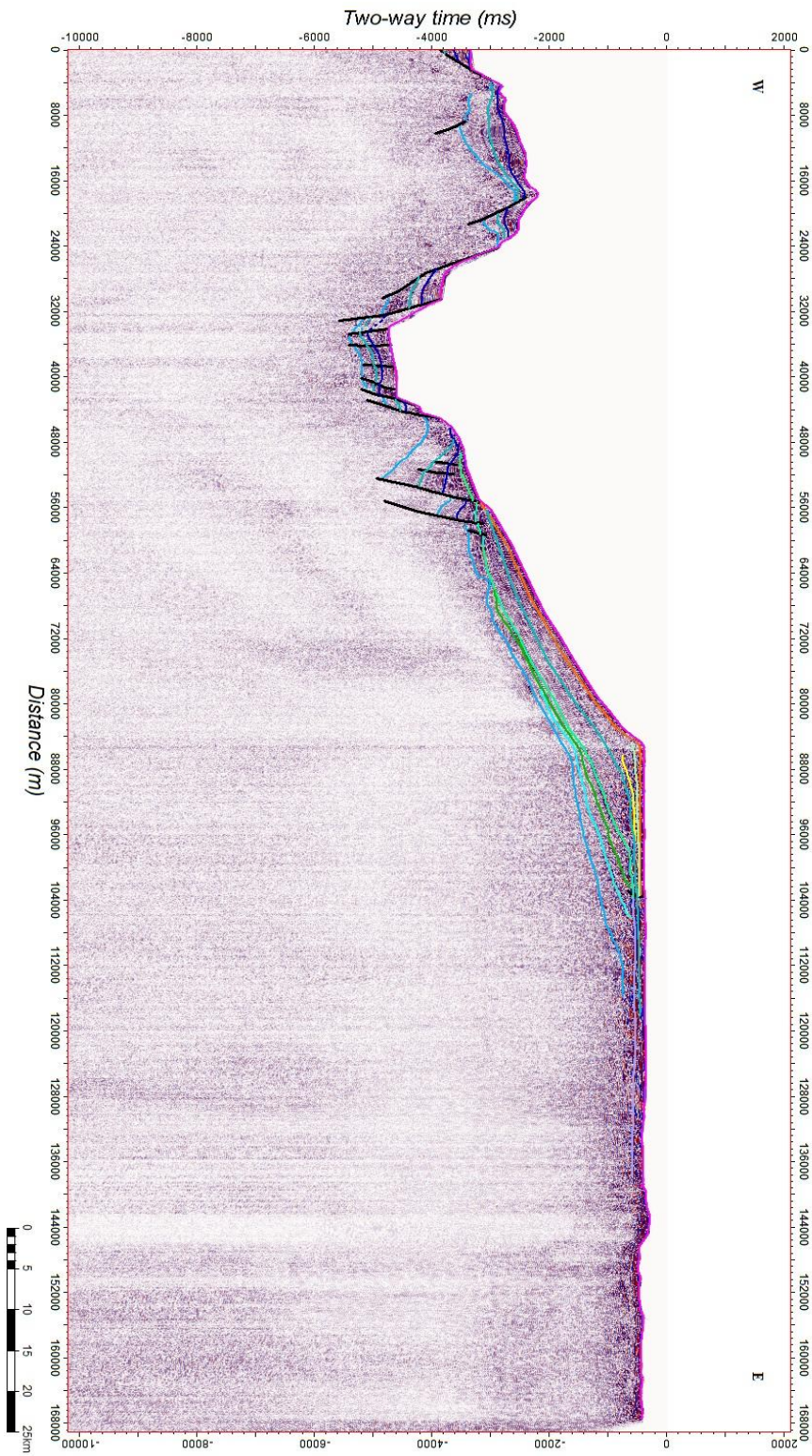
Figure 5.28: Line 26 from PETREL interpretation

Line 24 is the southernmost of the lines collected in the 2004-data (Fig 5.1). It follows an E-W trend from the sedimentary basin to the west of the knipovich ridge to the continental shelf close to Isfjorden on Svalbard. It is the longest line of all used in this thesis at 171,5km in length and is the only one used that has the entire eastern sedimentary basin as well as continental rise and shelf.

Sediment accumulation and seismic interpretation

At the western edge of the profile (Fig. 28), the edge of a sedimentary basin is found. Basement is located at 4700ms, where a fault with 1700ms heave shifts the basement to 3000ms depth. From 8km to 26km into the profile, a small sedimentary basin is found. Here, basement has a TWT depth ranging from 3500ms to 2600ms. This also is noted as the western ridge cresting the rift axis. A large normal fault offset basement to a small terrace at 4800ms, before a second, smaller fault with a heave of 800ms leaves basement at 5600ms in the rift basin. While the low resolution of the profile makes it difficult to discern the transition from sediments to magmatic basement, it is interpretated to be rising slightly in TWT depth from 5600ms to 5250ms. At 46km into the profile, a westward trending fault ends the rift basin, and basement is found at 4200ms. From 48km to 60km into the profile, two smaller sedimentary basins are found. Basement appears as rotated normal fault blocks. From 60km into the profile, basement has a steady rise in TWT depth from 3400ms, to 600ms at 110km into the profile. This is around 20km into the continental shelf at Isfjorden.

The sediments are well laminated throughout this profile, none of the units are chaotic in structure, apart from the thin covers above large faults. The far western basin contains up to 1300ms of sedimentary cover, divided into three units. These sediments are well laminated, but some internal clinoform structures are found. The sedimentary basin on top of the ridge crest has a thickness ranging between 500ms and 1000ms. These units are well laminated, with no other internal structures. A small terrace 5km in length is found on the western edge of the rift basin. It has a total thickness of 1100ms and has three units with similar structures to the units further west. The lowermost of the three units on this terrace has stronger amplitude variations, indicating a change in the depositional regime. Transitioning into the rift basin is what appears as a chaotic side infill. Within the rift basin itself, the sedimentary cover

73

is substantial and relatively uniform in thickness, around 700-900ms. While some intra-sedimentary faults are found, this accumulation is well laminated. It is difficult to correlate to other sedimentary units. The eastern rift basin terrace has increasing sedimentary thickness towards the east from 500ms to 2000ms in thickness. These are homogenous and well laminated, although thickness increases towards the west. A thin unit of glacimarine sediments are deposited on top. A large fault at 57km into the profile initiate the continental rise. 700-1000ms of sediment accumulations are found. These units are well laminated and interpretated largely to be of glacial marine origins. The sedimentary thickness is uniform at around 900ms up to the continental shelf, where the thickness gradually decreases to 200ms towards the eastern end of the profile

Basic Modeling
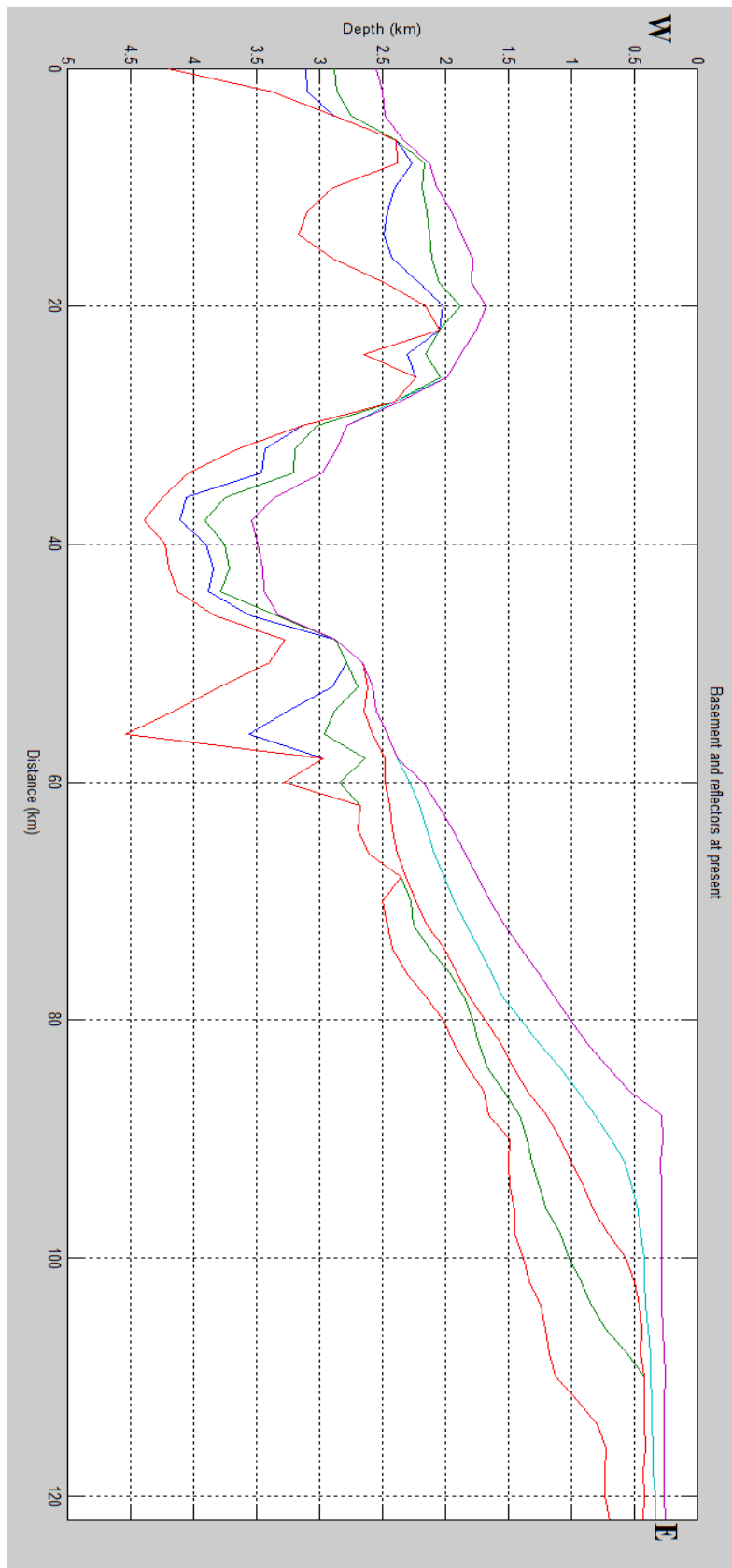
Figure 5.29: Depth-converted from TWT line 24 picked with 1km intervals Velocities are taken from Faleide et al. (1996), Ljones et al. (2004) and Kandilarov et al. (2008).
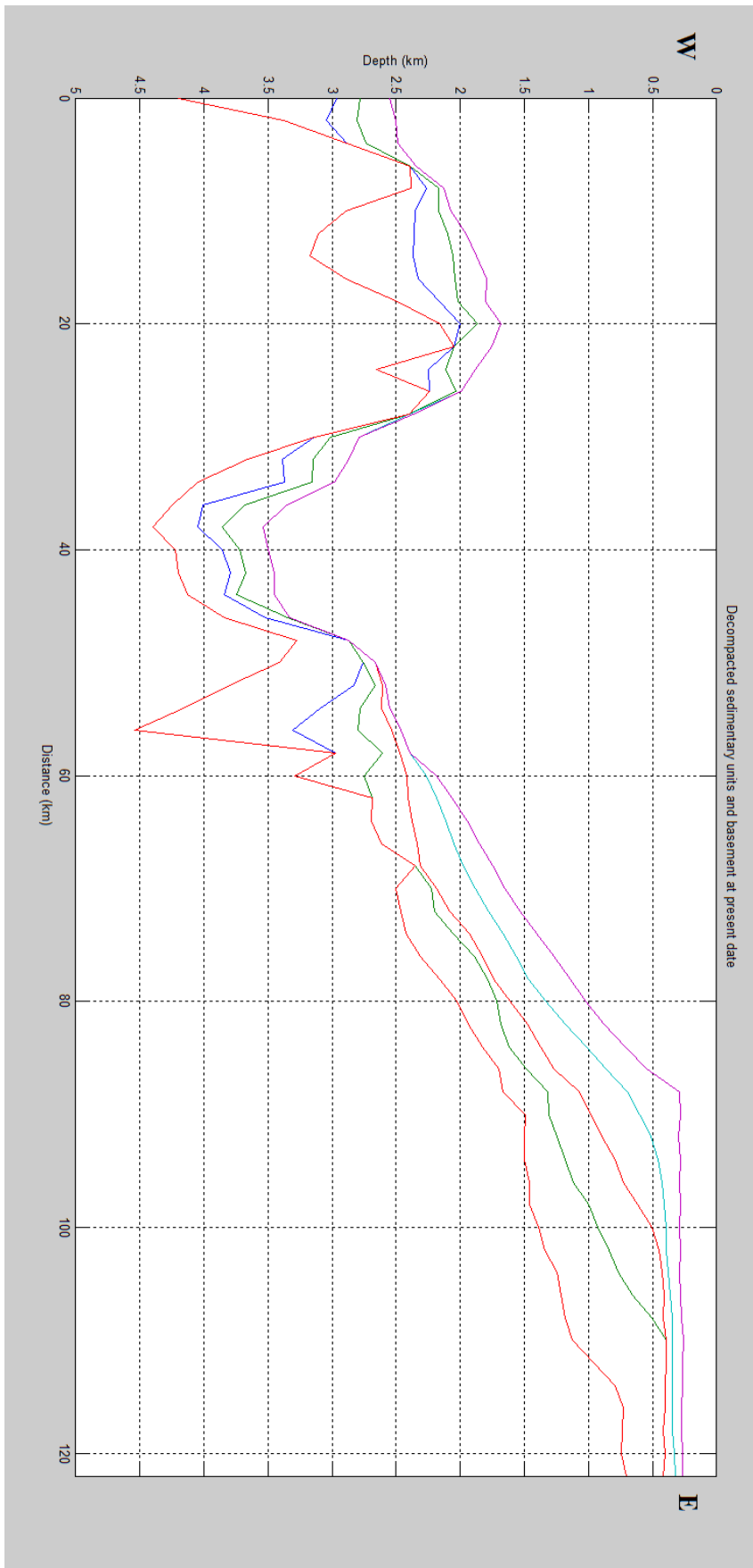
Figure 5.30: Line 24 with all sedimentary units decompacted.

76
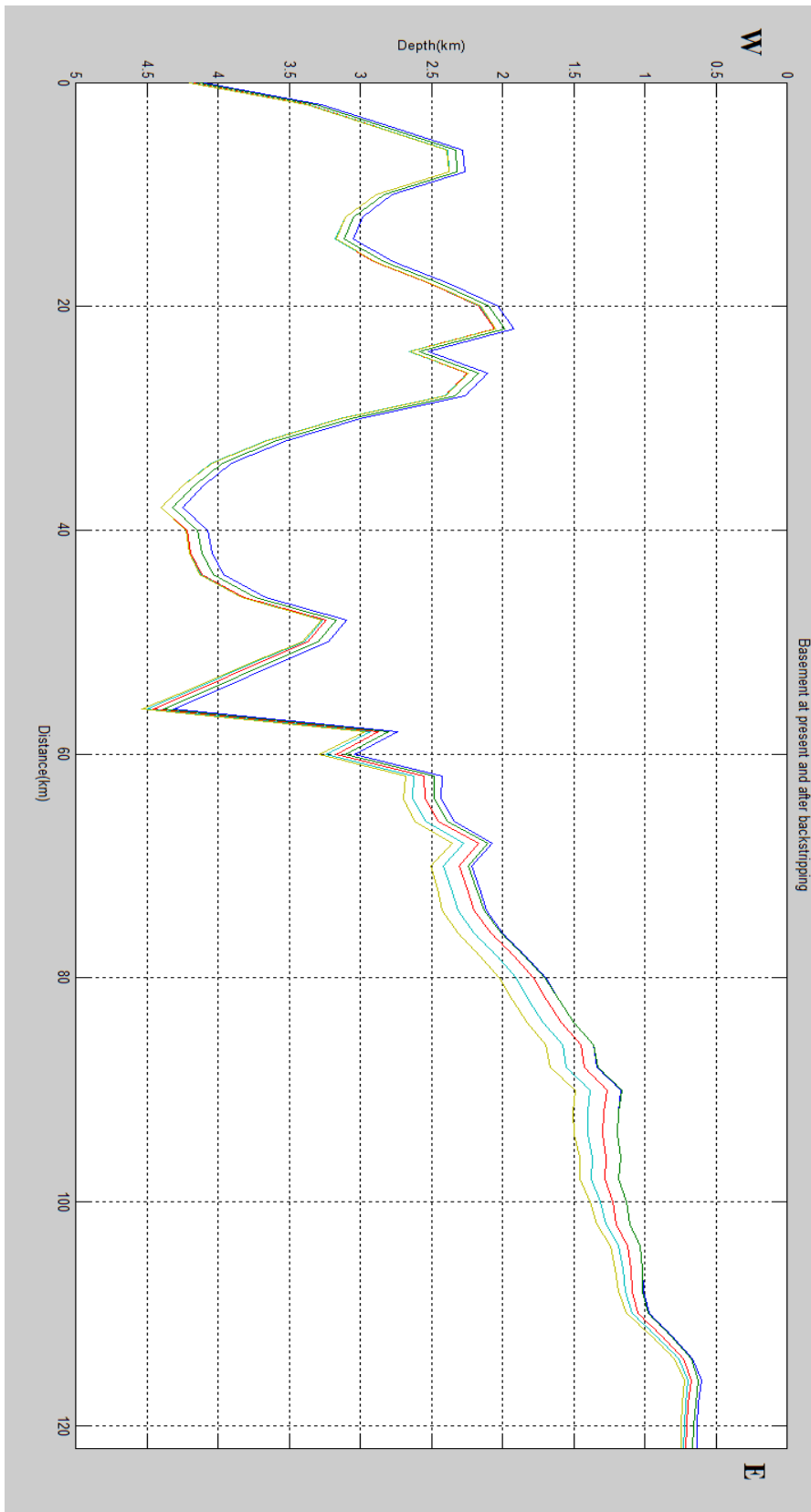
Figure 5.31: Basement modeled after removal of successive sedimentary units for line 24. The bottom, yellow line is the original basement depth, lime green is basement depth with the first sedimentary unit backstripped, red is basement depth with the second sedimentary unit backstripped, dark green is basement with the third unit backstripped and the blue line is the final basement depth with all sedimentary units backstripped.
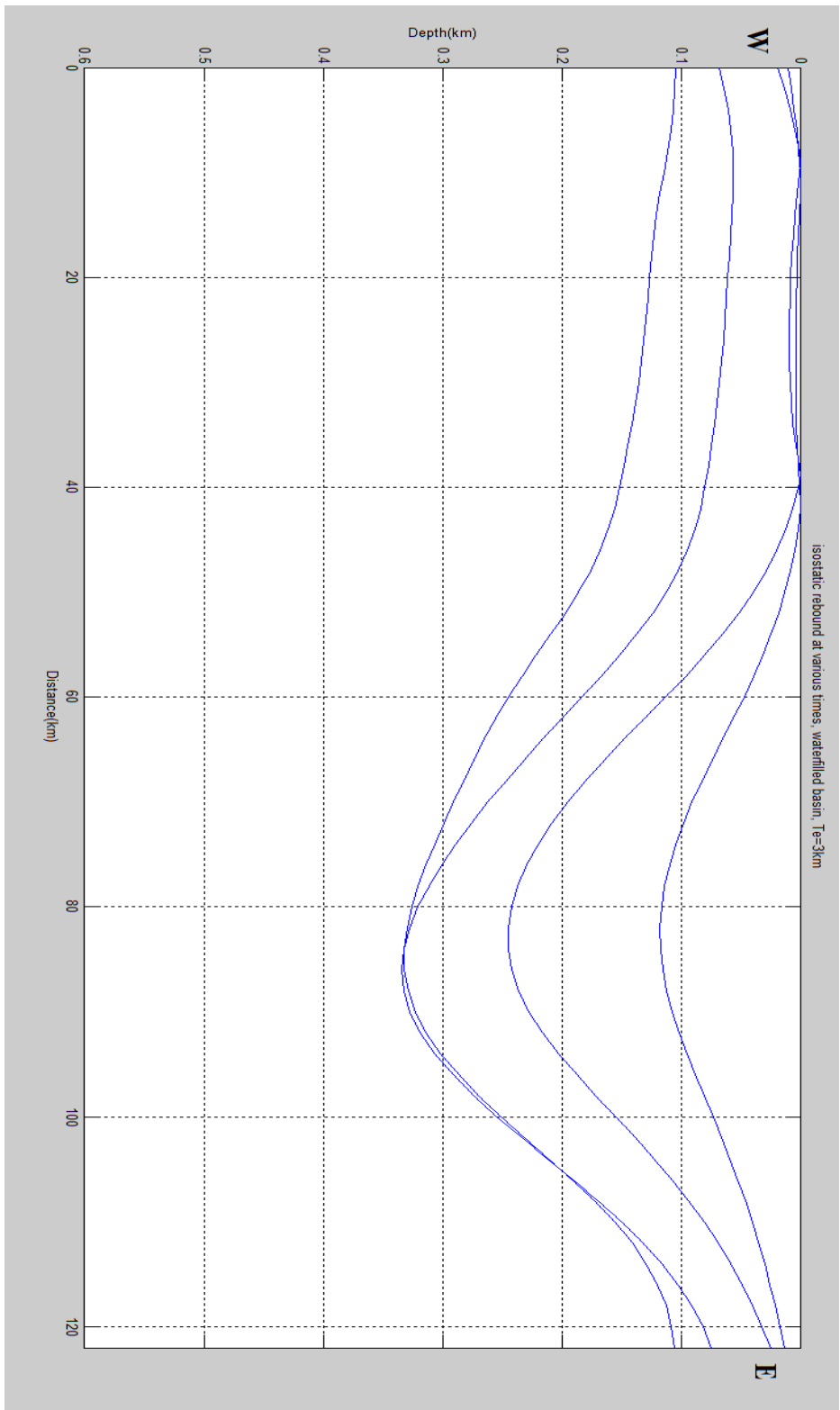
Figure 5.32: Modeled basement depth Δd, isostatic rebound after backstripping for line 24. The upper line is the change in basement depth with one sedimentary unit backstripped, the second and third lines show the change in basement with two and three units backstripped respectively. The lowermost line is the total change in basement depth with all sedimentary units backstripped.

Using the twt-traveltimes extracted and compiled PETREL-data, a datasheet is created (Appendix). These times are depthconverted (Fig. 5.29) using the average seismic P-wave velocity compiled in previous studies (Faleide et al., 1996, Ljones et al., 2004 and Kandilarov et al., 2008). The data are then processed in Matlab to yield decompacted sediment deposition depths and a modeled basement with no sediment cover. Faults are treated as static basement, and basement has a fixed elastic thickness Te of 3km. Around 40 km of continental shelf was not included in the model due to the relatively thin and uniform distribution of sediments, and to enhance data quality.

Line 24 is the only line in this study containing the entire continental rise and shelf. It is therefore the only line with a complete eastern flank sedimentary basin. The modeled data from this line is the most complete and relevant of all lines. The depth-converted line reveals a total sedimentary thickness of 1500m at the far western sedimentary basin. As a side note, having a complete mapping of this basin would benefit the modeling greatly, due to the boundary conditions of the modeling software. The 8km long sedimentary basin on top of the western ridge has varying sedimentary cover thicknesses, from 400m up to 1400m at its thickest. Close to the faults of the horst-formation that defines the basement, it appears that the magmatic basement could be exposed. Within the rift basin, the sediment thickness is higher towards the western edge of the basin, at 1000m in thickness. Towards the eastern edge of the basin, this thickness gradually decreases towards 500m. Within the rotated basement fault block at the eastern end of the rift basin, sediment thickness increases to 1950m at the eastern edge of the rotated block. The continental rise and shelf has a substantial sedimentary cover, ranging from 1000m close to the rift basin, to 1550m at the start of the continental shelf. At the eastern edge of the profile, on the continental shelf, sediment thickness is calculated to be around 550m. The decompacted sediment thicknesses (Fig. 5.30) show that the deeper, older units estimated to be G0 and GI show the largest changes of up to 150m, although this only is the case in sedimentary basins with substantial thicknesses.

Using the modeled magmatic basement depths (Fig 5.31) after backstripping of successive units in conjunction with the total isostatic curves (Fig 5.32), it is apparent that the presence of the full continental shelf has yielded better modeling results. Backstripping of the first unit, estimated to be megasequence G1 yields close to no isostatic rebound to the west of the rift basin. The small changes here could be related to the wavelength of the profile used in the modeling. At 85km into the profile, the largest isostatic rebound is calculated at 125m. It decreases gradually towards the continental shelf and is calculated to be 25m at the eastern

edge of the profile. Further backstripping of the second unit yields similar results to that of backstripping the first unit. There are no changes to the west of the rift basin, but isostatic rebound peaks at 245m at the same location as the first backstripped unit, 85km into the profile. On the continental shelf, at the eastern end of the profile, this rebound is 40m. Backstripping the third unit yields a more uniform isostatic rebound and changes to basement depth. To the west of the rift axis, the total isostatic rebound is 60+/-15m. At 85km into the profile, the total isostatic rebound is 340m. Backstripping the final unit, largely confined to the western parts of the profile, yields a total isostatic rebound from 100m at the western edge of the profile, 150m at the rift axis, 340m in the middle of the continental rise and 110m at the continental shelf.

6   Discussion

6.1   Values and sources of error

Seismic interpretation is a matter of opinion. Interpretation is done from an inverse point of view, as there is no solid information to tie the information tothe results directly. One of the legs of the Ocean Drilling Program has conducted a survey on the Svalbard Margin between lines 5 and 7b, however it cannot be used to tie the present results together, although information could be used to further enhance future studies. Seismic acquisition as the one used to acquire the data for this study is based on reflection of sonic waves from interfaces between different sedimentary units and strata. The resolution is based on the frequencies created by the source array, as well as significant changes in acoustic impedance in the medium surveyed (Keary et al., 2002). Furthermore, the medium depth, absorption and source frequencies affect resolution. A higher frequency yields better resolution, but is absorbed before penetrating deeper. So the choice of source either has to sacrifice penetration depth or resolution. The key is to find the right balance. Data used in this survey are generally of good quality, albeit with some noise due to sideswipes, as well as strong multiples on lines 26 and 7b. Estimates from a dominating frequency of 10Hz and velocity within the medium of 3,5km/s yields a wavelength of 350m and a resulting resolution- of 43,75m to 87,5m in deeper parts of the sedimentary units.

The basement reflector is at times difficult to interpret. This is a result of a few factors in particular. At some locations, the large burial depth makes it difficult to detect the transition from sediment cover to magmatic rocks. Although the interface should have a change in acoustic impedance leading to a strong reflector, massive sediment cover can absorb much of the energy in a sonic signal. Noise is the second factor, and is present in many forms. Within the rift basins, the newly formed crust contains a large number of smaller and larger faults, dispersing and diffracting the sonic energy from the source, even if the basement is buried under a thin layer of sediment. Diffraction and sideswipes from large faults also cause issues with discerning this interface.

When converting from TWT to depth, values has been chosen from previous studies to perform this conversion (Table 6.1).

Table 6.1: Regional speeds within the different megasequences

Sequence	Kandilarov et al., (2008)	Ljones et al., (2004)	This study
GIII	1.60 - 1.70 km/s	1.75 - 1.90 km/s	1.70 km/s
GII	2.00 - 2.18 km/s	2.00 - 2.35 km/s	1.90 - 2.20 km/s
GI	2.30 - 3.20 km/s	2.23 - 2.85 km/s	2.70 km/s
G0	2.95 - 3.33 km/s	2.90 - 4.15 km/s	3.00 km/s

While the values used are well within estimates provided from previous studies, if values used are changed slightly, the depth can change significantly. As picking a value from the upper or lower limits of a study can result in a vertical change of up to 50%, a value around half has been used as the average velocity.

Using Matlab, a few variables has been used (Allen and Allen, 2013, Dick et al., 2003 and Austegard, pers. comm. 2014). They are for porosity curves fitting sediments dominated by sand, but with smaller grain inclusions, as well as density and strain values for the mantle, crust and sediments. They are used as the values fit closely to that of a thin oceanic crust at a slow spreading ridge. These are used to complete formulas discussed in chapter 4. For:

$$\phi = \phi_0{}^{-cy}$$

ϕ_0=0.56 and c=0.39;

And for backstripping formulas:

ρ_m=3300 kg/m^3
ρ_g=2685 kg/m^3
ρ_w=1030 kg/m^3
Te=3000 m

Youngs Modulus and Poissons Ration:

v=0.25
E=60000000000 (6*10^9)

While these values are used with confidence, using a larger value of Te, Elastic Thickness, will cause the removal of a load from one point of the crust to have significance to a greater lateral extent. 3000m is used, as it is tied to a thin crustal thickness at slow spreading ridges.

6.2 Sediment distribution and bathymetry

The Knipovich ridge has been extensively studied, both in terms of sediment buildup and distribution (e.g. Kandilarov et al., 2008, Faleide et al., 1996, Hjelstuen et al., 2007), as well as tectonic and magmatic development and structure (e.g. Crane et al., 2001, Ljones et al., 2004). As this area is relatively young in geological terms, it is possible to estimate the depositional environments of all sediment buildup in this area. The most likely major sources of sedimentation are gravity movements from the Svalbard shelf, hemipelagic and glacial marine sedimentation as well as drift movements such as contourites. Some units have an apparent dominating depositional factor, while others have a combined factor of these three major depositional methods.

All lines interpreted in PETREL, with the exception of line 02, have significant sediment buildup on both the eastern and western flank basins. In general, there appears to be a relatively uniform basin at the western edge of the profiles with 700-1000m of sediment cover. The western basin, transitioning to the continental shelf has a sediment thickness ranging from 1500m to over 2000m. There are large variations within the rift basin itself. Line 1 appears to have little or no sediment cover, while other lines appear to have several hundred meters of sediment cover.
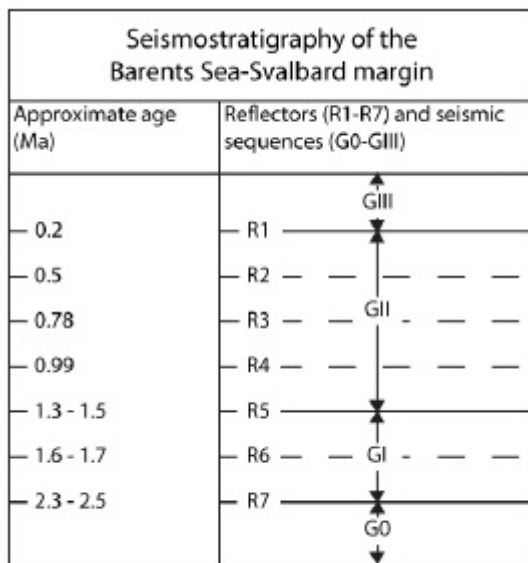
Figure 6.1: Sediment stratigraphy of the Barents Sea – Svalbard Margin (Faleide et al., 1996).

The sediments have been classified into four mega-sequences in previous studies (Fig 6.1). These are classified according to the time of deposition in relation to the last glacial era initiated at around 2,5Ma. G0 has no maximum classified age, but is a classification of the sediment deposited before the glacial era. In general, few traces of mega-sequence G0 is found within the rift basin, but is present on both flanks.

The middle mega-sequences GI and GII are glacial marine sediments deposited during the last glacial era, when the sediment input from the Svalbard region was at its highest. These deposits are characterized by homogenous, well laminated and continuous reflectors on seismic profiles (Hjelstuen et al., 2007). These units are more massive on the eastern sedimentary basins, the continental shelf, with some exceptions. Lines 1 and 2 (Fig 5.3 and 5.8) have a significant buildup of sediment from these mega-sequences within a wedge-shaped structure close to and within the rift basin. This is likely due to the large influx of sediments from the Bellsund and Isfjorden fan system. A typical glacimarine sedimentation rate is in the order of 2-7 cm/ky in the Barents Sea region (Elverhøi, 1984). However, when calculated from the values extracted from Line 24 (Fig. 5.30), the resulting sedimentation rate is 51cm/ky. A high rate of sedimentation over a time span of 2Ma can only be related to a large glacial factor. This is related partly to unstable sediments on the Svalbard margin, resulting in turbidite flows or slumping (Hjelstuen et al., 2007). There are differences from the 1999 to the 2004 lines found here. While the 1999-system has chaotic internal structure, especially within GI and early GII units, sediment units in the 2004-dataset appear more laminated and homogenous. The chaotic internal structures are consistent with gravity-driven mass movements such as turbidite flows, while the well laminated GI and GII units provides questions. It is debated if this is a result of sediment input from the debris-rich ice at the bottom of the glacier, either as till or sediment rich melt during periods of deglaciation (Hambrey, 1994). The presence of all mega-sequences are found on the western flank basins, although mega-sequences GI and GII varies in thickness and significance. Line 5 (Fig. 5.18) has interpretations with all lines present, while other lines such as 24 (Fig 5.28) and 1 (Fig 5.2) only have G1 present as well as traces of the younger parts of GII. Sediment transport across the rift axis is possible as long as key aspects are preserved. The capacity of the sediment flows from the Svalbard margin has to be high enough for sediments to be carried over the axial ridges. This will also limit the sediment grain size in accordance with the capacity of sediment flows at that given time. The elevation if the axial ridge is also a key

factor, as a higher axial ridge will limit or prevent sediment transportation to the western basins.
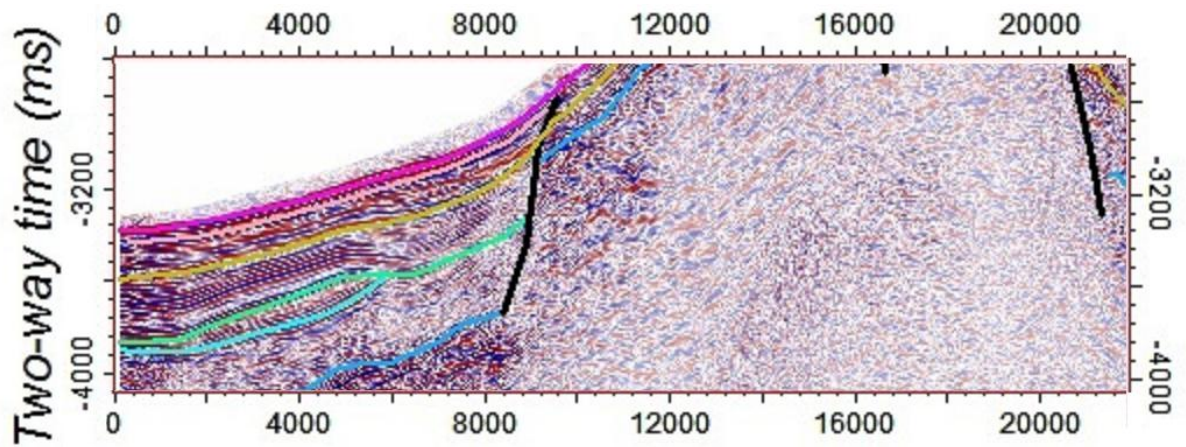
Figure 6.2: Contourite deposits between cyan and green lines on line 1

A feature found within the western sedimentary basins is the presence of contourites (Fig 6.2). Contourites are a result of deep ocean currents creating either onlapped units with migration in depositional direction or convex shaped units with layering differing from sediment deposits below. A unit 100-400ms in thickness, modeled to have a thickness of 100-400m in thickness is found with varying thicknesses on all 1999 ESE-WNW trending lines. These deposits are a result of the opening of the Fram Strait at around 9,8Ma (Engen et al., 2008).

6.3 Basement and faulting

The Knipovich Ridge is defined by Dick et al., (2003) as a first order supersegment spreading ridge without transform faulting with a total length of 550km. Crane et al., (2001) found that the Knipovich ridge shows individual segments of magmatic and tectonic activity of 50-100km in length. While several studies have been conducted to study segment variations and the processes involved in the accretion of oceanic crust at magma-poor spreading ridges, this is still an under-studied subject (Standish and Simms, 2010). The basement age has been studied through magnetic anomalies, but due factors such as high sediment loading, low magmatic activity and high heat flow, this has proved difficult (Engen et al. 2003). In this study, the top magmatic crustal formation is referred to simply as basement.

Basement is found at 4000-4500ms TWT-depth on all profiles that has the far western sedimentary basin present within the profiles. This is calculated to depths between 3500m and 3300m across all profiles. The value of 4500m on line 24 is due to an error, and has a corrected value of 3500m. Basement has different gradients and fault systems towards the western ridge high on different profiles, where some differ from the general structure.

Lines 1, 4, 5, 7a and 24 all have pronounced ridge systems to the west of the rift axis (Fig 6.3). On line 1, a single, large westward trending fault is found in the transition from the western basin to the western ridge axial high (Fig 5.2). Basement has a slight positive gradient as well towards the east, and at the top of the ridge, basement is estimated to be found at 1600ms. When modeled, this corresponds to a basement depth rise of 2200m over 20km (Fig 5.3). Line 4 appears to have no large faults from the western basin to the ridge high, but basement has a positive gradient towards the east. Basement depth changes from 3500m to 1575m over a 20km distance in this profile. This equals a 9,6% gradient average from the western basin to the axial high (Fig 5.14). Line 5 shares many similarities to that of line 4, as there are faults present from the western flank basin to the ridge. The faults are small, owing the changes in basement depth to the steady gradient (Fig 5.19). The difference in depth between these two locations along the profile is however less, at 1475m over a 25km distance.

Line 7a is significantly longer compared to other lines in the 1999-dataset. Its biggest advantage to this study is the larger coverage of the western flank of the ridge. While the other lines only contain less than 20km of data of the western flank, this line has over 50km of data from the western flank. Basement here is a part of several faults and fault systems. The most notable is the horst structure from 8-24km into this profile. The western fault of this horst structure has a 1400ms throw fault, from 4600ms to 3200ms TWT, while the corresponding fault on the eastern side has a throw of 400ms. Calculated basement depth is 3800m at the western basin and 2500 at the horst. Over the next 30km, basement has smaller variations in TWT, but has a gradual rise from 3200m to 2400m at the western rift basin high. Line 24 has a horst structure in the western part of the profile, where basement depth changes from an estimated 3500m at the start of the profile to 2400m at the top of the horst. There is a sedimentary basin within the horst, where it is calculated that basement reaches a depth of 3200m before rising to 2000m at the rift high.

Lines 2 and 3 have a less pronounced rift high (Fig 5.7 and 5.12 respectively). Line 2 appears to be the most symmetrical of the lines acquired in terms of both basement and

bathymetric profile. Although it has an elongated horst-profile on the western flank, basement changes only slightly between 2800m and 3250m the first 30km of this profile (Fig 5.8). There are seven faults penetrating from the sediments into the basement in this area. They make up the dual horst structure on the western flank. Other faults appear to be intra-sedimentary only. Line 3 is very short and due to this, it will not be used in the discussion, apart from the general remarks concerning the basement similarities to line 2.

Within the rift basin, lines 1, 3, 4 and 5 have a rotated fault block at the western edge of the rift basin of varying length from 5km on line 1 and 3 to 2km on lines 4 and 5. All lines except line 1 have sediment cover within the rift basin.
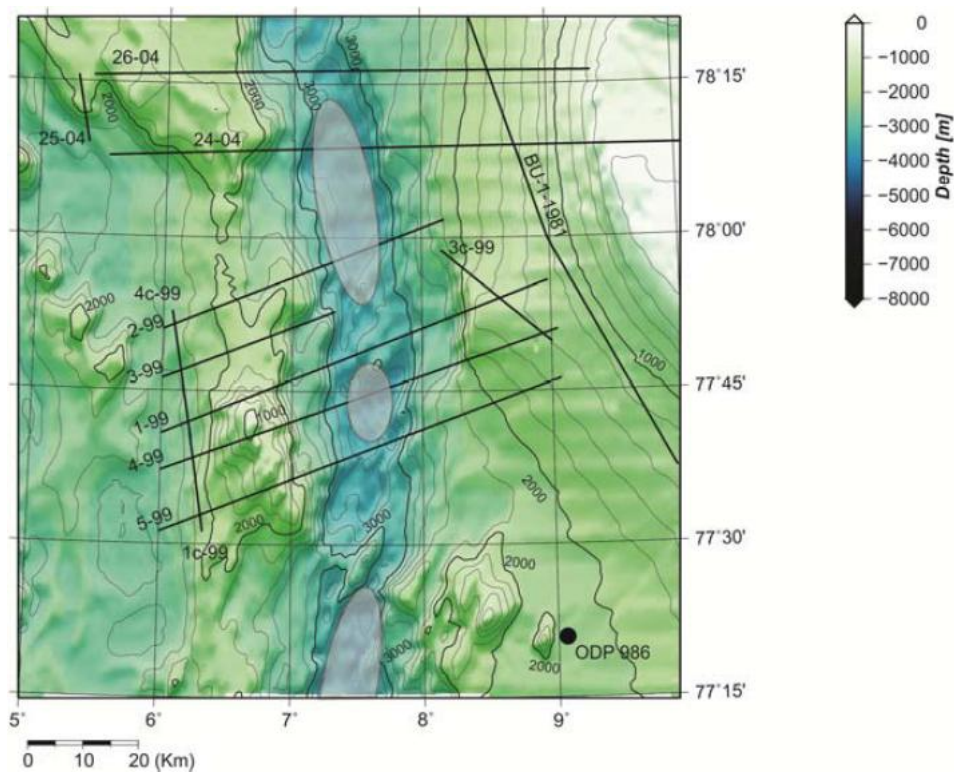
Figure 6.3: Bathymetric map of the survey area with all lines except 7 included. The semi-gray areas mark the areas dominated by tectonic activity by Crane et al., 2001 (Kvarven et al., 2014).

The areas with sediment cover are dominated by tectonic activity (Crane et al., 2001), while line 1 is the only profile with little or no sediment cover and is assumed to be dominated by magmatic activity (Fig 6.4). Basement is located at 3200m on line 1, and deeper on other lines in this study: Calculated at around 4000m for line 2 and 4, 3750m for line 5 and

7a and 4290m for line 24. The magmatic activity at line 1 is assumed by Crane et al., (2001) to divide two smaller segments of the Knipovich ridge.
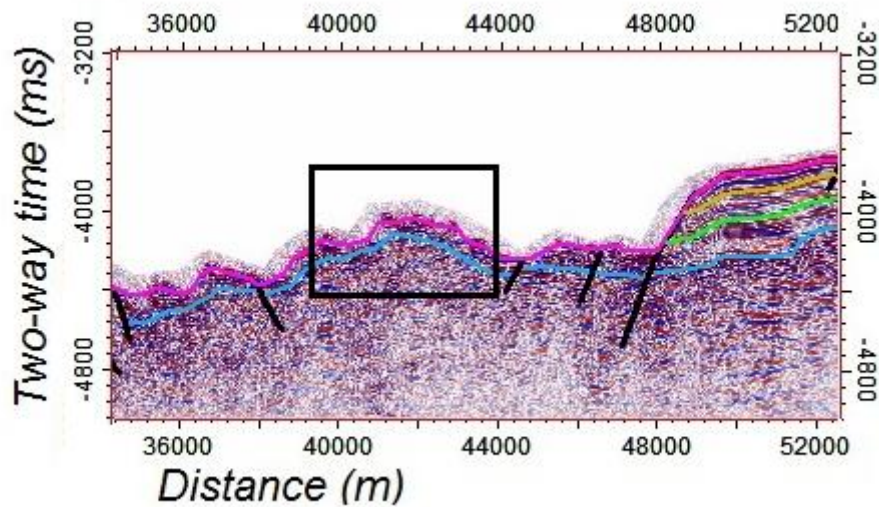
Figure 6.4: Rift basin from line 1. The black square marks the estimated magmatic rift axis.

The eastern flank has a rotated fault block creating a terrace structure on all lines, although the magnitude of faulting, length and rotation varies greatly from only slightly on line 5, to a separate terrace on line 1 and 4, to greatly rotated fault blocks on lines 7a and 24, where they have a throw of 700m and 1500m respectively.

The eastern basin has variations in its features as well. Its transition to the rift basin has a lower relief compared to the western side, and has less variation in depth, from 1900m to 2500m. Lines 2, 5 and 24 all have basement buried under at least 700m of sediment cover at the edge of the rift basin before the basement transitions into the eastern flank basin itself. While line 2 (Fig 5.8) only has a small length of the eastern basin as a part of the data recorded, lines 5 (Fig 5.19) and especially 24 (Fig 5.29) contain more data of this area. Line 5 has 30km of the continental rise within the profile. Basement is relatively horizontal at around 3200m within the first 25km before reaching 3000m at the eastern end of the profile. Line 24 is the most complete line in terms of data covering the continental rise and shelf. While the seafloor has a steady gradient towards the continental shelf from around 50km into the profile, basement is buried as a rotated fault block at this location, and is found at depths of up to 4500m. From 57km into the profile, basement has a positive gradient towards the continental shelf, reaching a final depth of 750m at the eastern end of the profile.

88

6.4   Basin modeling

As the final goal for this thesis is to model basement based backstripping sedimentary units, it relies on as much information as possible from the lines studied. One problem with a number of these lines is the incomplete mapping of the sedimentary basins on both sides of the rift basin. Lines 7a and 24 are by far the most suited, as they are long enough to thoroughly map either the western and eastern sides of the rift basin, respectively.

A tie to the seismic lines and their interpretations as megasequences and reflectors from these sequences has been attempted at best, although some changes has been made to ensure modeling without crashes or errors (Fig 6.1).

When modeling the lines, no boundary conditions were chosen, as it is hard to predict the exact sediment thickness past the recorded data. This results in boundary values of isostatic rebound being less than what is expected if the lines either were longer, or boundary conditions are used. Line 24 is the only line with a complete mapping of the continental shelf, and line 7a (Fig 5.27) has more data from the basin towards Greenland. This is reflected in the modeled results, where the isostatic rebound on line 24 (Fig. 5.32) is at its highest at the middle of the continental shelf, then becoming progressively smaller towards and onto the continental shelf. The result here is between 300-400m total isostatic rebound on the eastern flank and continental rise, while the western flank has a total isostatic rebound of 100-150m. The isostatic rebound of the basement is relatively homogenous across the western basin on line 7a is relatively homogenous as well, while the eastern side has a stronger peak and gradient towards its maximum. This result is significant, but does not completely explain the lack of symmetry along this ridge. Other lines produce curves of a more sinusoid shape, where the maximum values are relatively similar on both sides, with a minimum value within the rift basin. Due to the short length of these lines (1, 2, 4 and 5), they produce biased results. While the end points of the profiles in question have typical isostatic rebound of 300-400m, that value is based on a less than 10km long sedimentary basin on one or both sides.

As an active divergent boundary, there is a constant development at this ridge, and the modeling does not account for this. Assuming a constant rate of spreading of 11mm/yr over the last 2Ma, the profiles are 22km longer today. This is roughly the equivalent of the rift basin at present date (Fig 6.5).
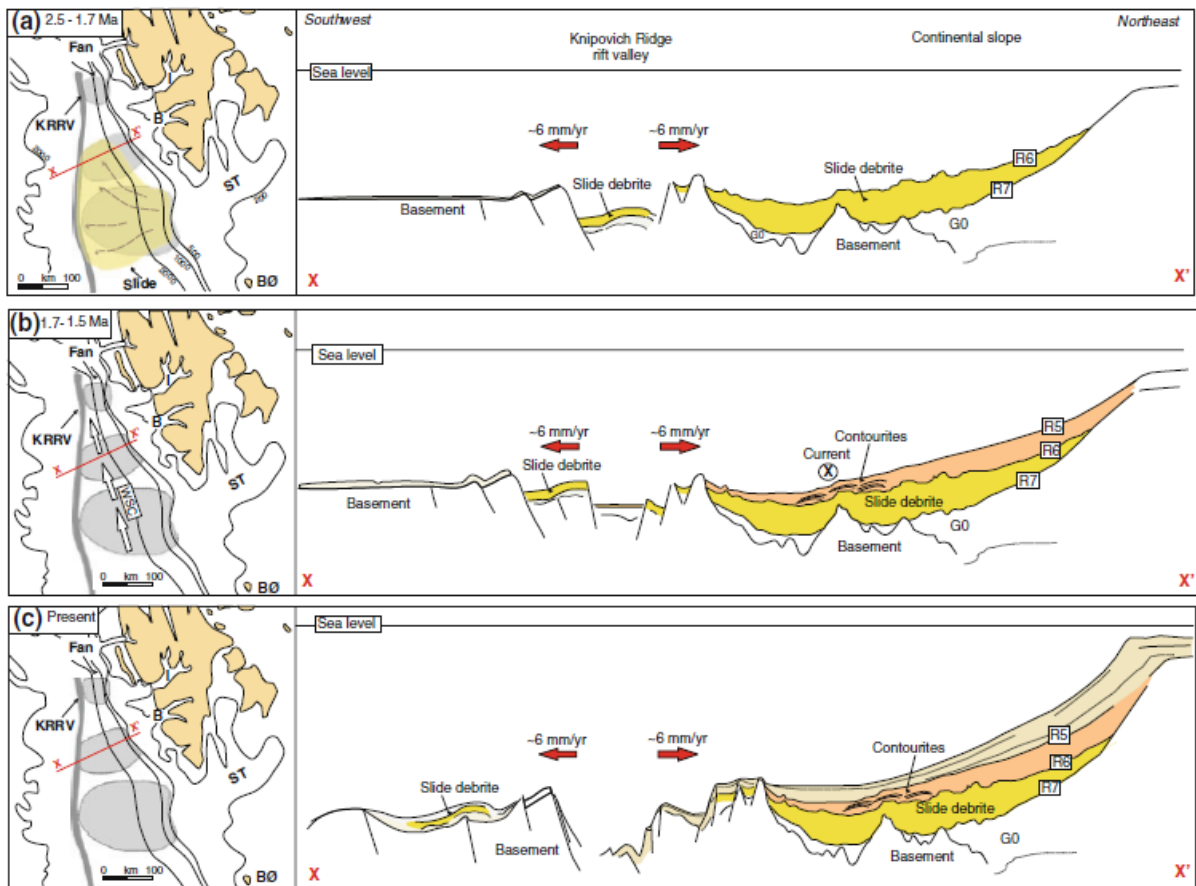
Figure 6.5: Maps and profiles showing the margin and ridge configuration off Western Svalbard at a) 2.5-1.7Ma, b) 1.7-1.5Ma and c) Present date. Half spreading rates from Kandilarov et al., (2008) KRRV=Knipovich Ridge Rift Valley, ST=Storfjorden Trough, BØ= Bear Island, WSC=West Spitsbergen Current, B=Bellsund, I=Isfjorden (Amundsen et al., 2011)

An enhancement to the modeling would be to properly incorporate this rifting, removing the appropriate length of crust between each iteration. Figure 6.5 shows a reconstruction by Amundsen et al., (2011) across line 7, where seafloor spreading has been accounted for. It also reconstructs sedimentary input and faulting processes across the rift axis.

Furthermore, the thermal evolution of the Knipovich Ridge can come into play, as according to theories by Airy and McKenzie, backstripping where tectonic uplift is the result such as this study, it will result in thickening of the crust. This relates strongly to the rate of spreading and the amount of time since rifting was initiated. A geothermal gradient too high due to rifting will over time settle to its initial and stable state, allowing the crust to thicken. As a significant thickness of sedimentary cover is removed, this will also have an effect, as it

changes the geothermal gradient, and this combined with a change in geothermal gradient as a result of either stretching or rifting, yields changes to basement depth if modeled (Watts, 2001)..
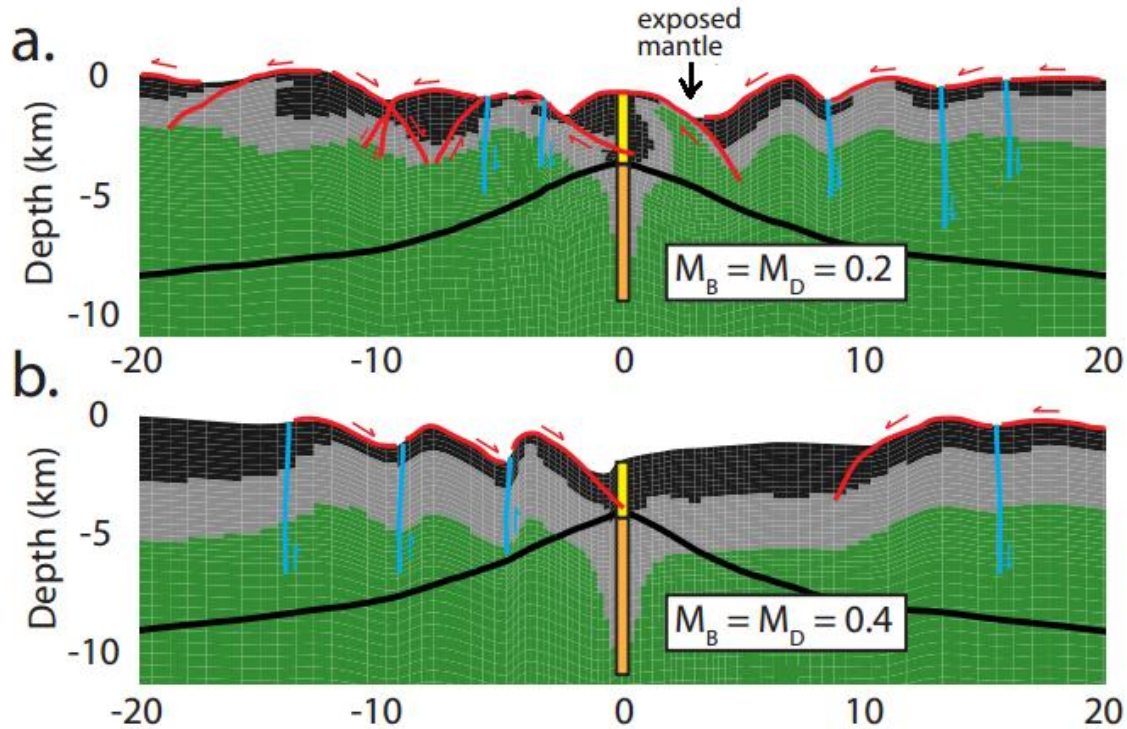
Figure 6.6: Modeled extensional plate after 1.5Ma where the accommodated magmatic fraction in relation to the total effect of extension is set at a) 0.2 and b) 0.4. The black line is the 600°C isotherm. Green: Mantle, Gray: Diorite, Black: Gabbro M=Magmatic fraction within brittle and ductile sections. (Olive et al., 2010)

Backstripping alone does not explain the non-symmetrical profile of the Knipovich Ridge. Several publications show that core complexes are important in the creation and development of slow and ultra-slow spreading ridges (e.g Cannat et al., 1995, Smith et al., 2008). The core complex is a type of rifting created from several detachment faults that over time expose tracts of gabbro from the crust and serpentinized peridotite from the upper mantle (Fig 6.6). This is suggested by modeling studies to happen only if the total magmatic fraction driving the rifting process is only 30 – 50% of the total extensional force (Olive et al., 2010). While oceanic core complexes first were thought to form entirely at magmatic-starved spreading ridges (Tucholke and Lin, 1994), recent studies show that they are virtually absent from the ultra-slow class of spreading ridges that are magma-starved (Tucholke, 2008). This

91

suggests that at least some fraction of the spreading force must be derived from magmatic activity. While the Knipovich Ridge is assumed to have magmatic activity at selected locations (Fig 6.4), it is largely dominated by tectonic activity (Crane et al., 2001 and Fig 6.3). The development of a core complex has a chance of exposing the upper mantle peridotite rocks (Fig 6.6). Serpentinized peridotite is the result of water intruding into the buried or exposed upper mantle olivine rocks (Fowler, 2005). On the Knipovich Ridge, the current rift basin is relatively uniform and most likely any exposed rocks will consist of magmatic extrusions of basaltic origin. However, faults with a throw high enough to expose the upper mantle rocks might be found, especially the faults from the western ridge crest towards the rift basin. They have a modeled throw at line 24 of 2,2km (Fig. 5.29), and if accounting for the angle of faulting, the total displacement is higher, as the throw is 2,5km. The result is 3,3km of the crust is found in this fault. While not proven, the non−symmetrical shape could be a result of the formation of a core complex (Fig 6.7).
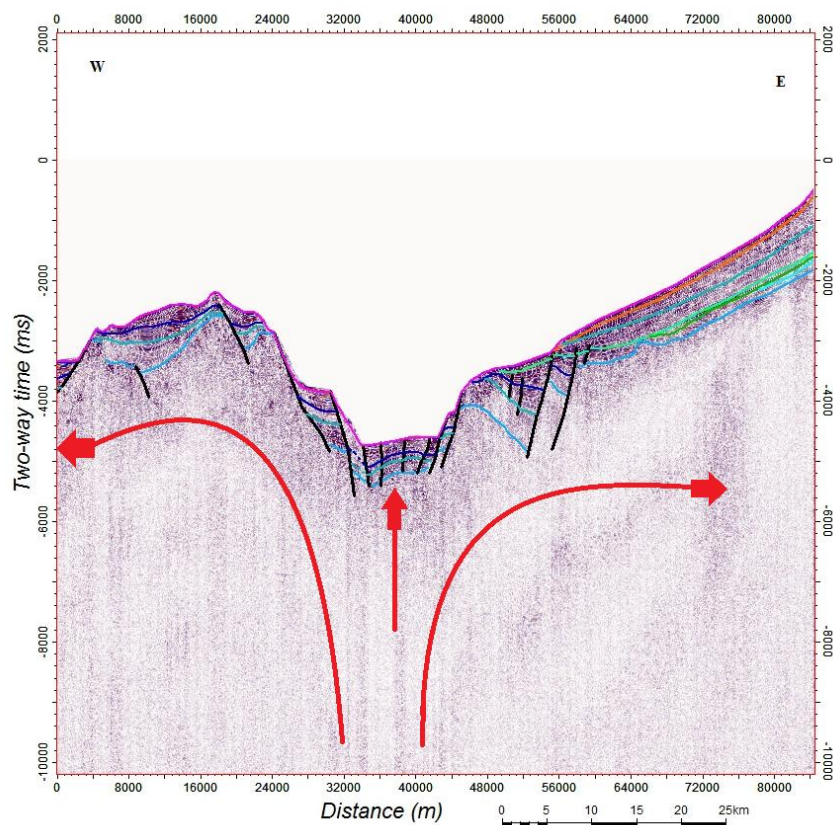
Figure 6.7: Cartoon displaying possible crustal movement at line 24.

While no traces of serpentinized peridotite were found during two scientific surveys in 2000 and 2002 where scraping of the basement was performed on both flanks and rift axis (Hellevang, 2003), the sediments covering the system could be a contributing factor to the reason why no traces of serpentinized peridotite were found. These samples were taken at around the same location as line 24, and this location might not be representative for the entire rift system.

7   Conclusion and closing remarks

A total of 11 seismic lines has been interpretated from both the 1999- and 2004-datasets. Six have been modeled to perform backstripping. The interpretation has been performed to yield results used in the modeling. Modeling of decompaction and backstripping of sedimentary units across profiles with good data quality as well as significant length was performed to investigate if the differences in sediment loading is the cause for the non-symmetrical shape of this ridge system.

The sedimentary units have been interpreted to best fit the regional megasequences (Fig 6.1) classified in relation to the last glacial era initiated at 2,5Ma. Their form, geometry and facies have been used to classify them into these categories. Basement was difficult to discern at some locations due to high levels of noise, as well as a deep burial depth. The ridge appears to be largely tectonically dominated and buried beneath sediments, although line 1 (Fig 6.2) is magmatically dominated. The axial high appears to be exposed, and is interpreted as an active magmatic ridge. There are horst and graben structures on all lines on the western flank, while the eastern flank varies between a large horst structure (Line 7a) or rotated fault blocks.

Modeling the basement has concluded that while sediment loading has a large impact on the development of the ridge system and has caused a higher grade of subsidence along the eastern flank, no clear conclusion can be drawn from this. The main cause is the lack of seismic data beyond the ridge highs on each side. Only 20km is present on most lines with the exception of lines 7a and 24. These two lines provided a good image of the sediment loading along the western flank basin and continental shelf respectively, and may be used to understand this problem. Further insight into the complex nature of this ridge system could be derived by further modeling the tectonics and rifting of the system.

References

Allen, P.A., Allen, J.R., (2013), Basin Analysis: Principles and Application to Petroleum Play Assessement, 3rd Edition Wiley-Blackwell LTD: ISBN: 978-1-118-45030-7

Amundsen, I.M.H., Blindnova, M., Hjelstuen, B., Mjelde, R., Haflidason, H., (2011). The Cenozoic western Svalbard margin; sediment geometry and sedimentary processes in an area of ultraslow oceanic spreading, Marine Geophysical Research

Austegard, A., Sundvor, E., (2000). The Svalbard Continental Margin: Crustal Structure from analysis of deep seismic profiles and gravity. Seismo-series 53: University of Bergen

Bradley, M.E., (1985). Practical Seismic Interpretation. Springer. ISBN-10: 9027721009

Cannat, M., Mevel, C., Maia, M., Deplus, C., Durand, C., Gente, P., Agrinier, P., Belarouchi, A., Dubuisson, G., Humler, E., Reynolds, J., (1995). Thin crust, ultramafic exposures, and rugged faulting patterns at the Mid-Atlantic Ridge 22-25oN. Geology, January v23: 49-52

Cannat, M., Sauter, D., Mendel, V., Ruellan, E., Okino, K., Escartin, J., Combier, V., and Baala, M., (2006), *Modes of seafloor generation at a melt-poor ultraslow-spreading ridge: Geology, v. 34: 605–608*

Cande, S. C., Kent, D. V., (1995). Revised Calibration of the Geomagnetic Polarity Timescale for the Late Cretaceous and Cenozoic. Journal of Geophysical Research 100(B4), 6093, 6095

Crane, K., Doss, H., Vogt, P., Sundvor, E., Cherkassov, G., Proshina, I., Joseph, D., (2001). The role of Spitsbergen Shear Zone in determining morphology, segmentation and evolution of the Knipovich Ridge. Marine Geophysical Researches 22: 153-205

DeMets, C., Gordon, R.G., Argus, D.F., (2010), Geologically current plate motions. Geophysics J. Int. 181: 1-80.

Dergunov, N., Roslov, Y., Kudineko, N., Tikhonova, I., (2004). Report of MCS data processing along lines 01-05, 01c, 03c, 04c, 06, 07a, 07b, SVALEX-1999. Sevmorgeo state company (Unpublished)

Dick, H.J.B., Lin, J., Schouten, H., (2003). An ultraslow-spreading class of oceanic ridge, Nature v426: 405-412

Dick, H.J.B., Natland, J.H., Ildefonse, B., (2006). Past and Future Impact of Deep Drilling in the Oceanic Crust and Mantle, Oceanography v19-4: 72-80

Elverhøi, A., (1984). Glacigenic and associated marine sediments in the Weddel Sea, fjords of Spitsbergen and the Barents Sea: A review. Marine Geology 57: 53-88

Engelder, T., (1993). Stress Regimes in the Lithosphere. *Princeton University Press, Princeton, New Jersey, USA;.* 447p

Engen, Ø., Eldholm, O., Bugnum, H., (2003). The Arctic plate boundary, *J Geophysics Res 108(B2):2075. doi: 1029/2002JB001809*

Engen, Ø., Hirth, G., Evans, B., (2008). Opening of the Fram Strait gateway: A review of plate tectonic constraints. *Techtonophysics 450: 51-69*

Faleide, J.I., Solheim, A., Fiedler, A., Hjelstuen, B.O., Andersen, E.S., Vanneste, K., (1996). Late Cenozoic evolution of the Western Barents Sea – Svalbard continental Margin. *Global and Planetary Change 12: 53-74*

Fowler, C.M.R, (2005) The Solid Earth, *Cambridge University Press, ISBN:0-521-89307-0*

Hambrey, M., (1994). Glacial Envirnoments. *UCL Press, ISBN:1-85728-005-9*

Hellevang, B., Pedersen, R.B., (2005). Magmatic segmentation of the Northern Knipovich Ridge: Evidence for high-pressure fractination at an ultraslow spreading ridge. *Geochemistry, Geophysics, Geosystems, volume 6 issue 9*

Hess, H.H., (1962). History of Ocean Basins. *Petrologic Studies, 11.1962: 599-620*

Hjelstuen, B.O., Eldholm, O., Faleide, J.I., (2007). Recurrent Pleistocene mega-failures on the SW Barents Sea Margin. *Earth and Planetary Science Letters 258: 605-618.*

Kandilarov, A., Mjelde, R., Okino, K., Murai, Y., (2008). Crustal structure of the ultra-slow spreading Knipovich Ridge, North Atlantic, along a presumed ridge segment center. *Marine Geophysical Researches, Volume 29, Issue 2:109-134*

Keary P., Brooks M., Hill I., (2002). An Introduction to Geophysical Exploration 3rd Edt, *Blackwell Publishing. ISBN-13: 978-0-632-04929-5*

Kvarven, T., (2009). Tolkning av multikanals refleksjonsseismikk fra Svalbardmarginen og Knipovichryggen. *University of Bergen*

Kvarven, T., Hjelstuen, B.O., Mjelde, R., (2014) Tectonic and sedimentary processes along the ultraslow Knipovich spreading ridge. *Marine Geophysical Research 35, Issue 2: 89-103*

Lundin, E., Dore, A.G., (2002). Mid-Cenozoic post-breakup deformation in the passive margins bordering the Norwegian-Greenland Sea. *Marine and Petroleum Geology 19: 79-93*

Ljones, F., Kuwano, A., Mjelde, R., Breivik, A., Shimamura, H., Murai, Y., Nishimura, Y., (2004). Crustal transect from the North Atlantic Knipovich Ridge to the Svalbard Margin west of Hornsund. *Tectonophysics 378: 17-41*

MacDonald, K. C., (2001). Mid-Oceanic ridge tectonics, volcanism and geomorphology, *Science v3: 1798-1813*

MacDonald, K. C., Scheirer, D. S., Carbotte, S. & Fox, P. J., (1993). It's Only Topography, Parts 1 and 2. *GSA Today*

Marshak, S., (2005). Earth: Portrait of a Planet, Second Edition. *W.W. Norton & company LTD. ISBN: 0-393-92502-1 (paperback).*

Michael, P.J., Langmuir, C.H., Dick, H.J.B., Snow, J.E., Goldstein, S.L., Graham, D.W., Lehnert, K., Kurras, G., Jokat, W. and Muhre, R., (2003). Magmatic and amagmatic seafloor generation at the ultraslow-spreading Gakkel Ridge, Artic Ocean. *Nature v432: 956-961*

Mjelde, R., Johansen, T. A., (1999). GFJ294 Cruise report, *Department of Earth Science, University of Bergen (Unpublished)*

Mjelde, R., (2004). GEOL201 Cruise report, *Department of Earth Science, University of Bergen (Unpublished)*

Mosar, J., Torsvik, T. H., BAT Team, (2002). Opening of the Norwegian and Greenland Seas; plate tectonics in Mid Norway since the Late Permian. *In: Eide EA (ed) BATLAS-Mid Norway plate reconstructions atlas with global and Atlantic perspectives, Geological Survey of Norway: pp 28-59*

Olive, J.A., Behn, M.D., Tucholke, B.E., (2010). The structure of oceanic core complexes controlled by the depth distribution of magma emplacement. *Nature Geoscience 3: 491-495*

Sheriff, R. E., Geldart L. P., (1995). Exploration Seismology 2nd edt, *Cambridge University Press: ISBN-13: 978-0521468268*

Smith, D.K., Escartin, J., Schouten, H., Cann, J.R., (2008). Fault rotation and core complex formation: Significant processes in seafloor formation at slow-spreading mid-oceanic ridges (Mid-Atlantic Ridge, 13°-15°N). *Geochemistry, Geophysics, Geosystems v9 issue 3.*

Solheim, A., Faleide, J.I., Andersen, E.S., Elverhøi, A., Forsberg, C.F., Vanneste, K., Uenzelmann-Neben, G., Channel, J.E.T., (1998). Late Cenozoic seismoc stragegraphy and glacial geological deveopement of the East Greenaldn and Svalbard-Barents sSea continental margins. *Quarternary Science Reviews v17: 155-184*

Standish, J.J., Sims, K.W., (2010). Young off-axis volcanism along the ultraslow-spreading Southwest Indian Ridge. *Nature Geoscience 3 (4): 286-292*

Stanley, S.M., (2009). Earth System History, Marshall: ISBN-10: 1-4292-0520-2

Steckler, M.S., Watts, A.B., (1978). Subsidence of the Atlantic-Type Continental Margin off New-York. Earth and Planetary Science Letters, 41: 1-13

Stewart, J., Watts, A.B. & Bagguley, J., 2000. Three-dimensional subsidence analysis and gravity modelling of the continental margin offshore Namibia, *Geophys. J. Int., 141: 724–746*

Timoshenko, S., Woinowsky-Krieger, S., (1959). Theory of Plates and Shells. McGraw-Hill Book Company Inc. ISBN:0-07-064779-8

Tucholke, B.E., Lin, J. A, (1994). Geological model for the structure of ridge segments in slow spreading ocean crust. *Journal of Geophysical Research, 99(B6): 11937–11958*

Tucholke, B.E., Behn, M.D., Buck, W.R., Lin, J., (2008). Role of melt supply in oceanic detachment faulting and formation of megamullions. *Geology, 36(6): 455–458*

Van Der Plujim, B.A., Marshak, S., (2004). Earth Structure, 2nd Edition, Norton: ISBN-10:0-393-92467-X

Watts, A.B., Torné, M., (1992). Subsidence History, Crustal Structure, and Thermal Evolution of the Valencia Trough: A Young Extensional Basin in the Western Mediterranean. Journal of Geophysical Research vol 97, No B13: 20021-20041

Watts, A.B., (2001). Isostacy and Flexure of the Lithosphere. Cambridge University Press: ISBN:0-521-62272

Appendix

Line 24, TWT data

(km)		Two way travel time (ms)					
Distance x	Trace	Basement	Reflector 1	Reflector 2	Reflector 3	Reflector 4	Seafloor
0.00	1.00	4574.00	4574.00	4310.00	4183.00	3900.00	3900.00
1.00	21.00	4621.00	4621.00	4387.00	4303.00	3910.00	3910.00
2.00	41.00	4300.00	4300.00	4326.00	4300.00	3911.00	3911.00
3.00	61.00	4250.00	4250.00	4108.00	4055.00	3910.00	3910.00
4.00	81.00	4200.00	4200.00	4111.00	4019.00	3882.00	3882.00
5.00	101.00	4271.00	4271.00	4111.00	3942.00	3814.00	3814.00
6.00	121.00	3964.00	3964.00	3934.00	3732.00	3632.00	3632.00
7.00	141.00	3518.00	3518.00	3518.00	3518.00	3439.00	3439.00
8.00	161.00	3200.00	3200.00	3200.00	3061.00	3061.00	3061.00
9.00	181.00	3274.00	3274.00	3274.00	3103.00	3051.00	3051.00
10.00	201.00	3376.00	3376.00	3376.00	3281.00	3144.00	3144.00
11.00	221.00	3392.00	3392.00	3392.00	3333.00	3205.00	3205.00
12.00	241.00	3430.00	3430.00	3430.00	3350.00	3290.00	3290.00
13.00	261.00	3444.00	3444.00	3444.00	3371.00	3297.00	3297.00
14.00	281.00	3572.00	3572.00	3572.00	3480.00	3428.00	3428.00
15.00	301.00	3655.00	3655.00	3655.00	3588.00	3491.00	3491.00
16.00	321.00	3747.00	3747.00	3747.00	3643.00	3475.00	3475.00
17.00	341.00	3632.00	3632.00	3632.00	3469.00	3404.00	3404.00
18.00	361.00	3466.00	3466.00	3466.00	3403.00	3278.00	3278.00
19.00	381.00	3499.00	3499.00	3499.00	3458.00	3378.00	3378.00
20.00	401.00	3560.00	3560.00	3560.00	3490.00	3414.00	3414.00
21.00	421.00	3650.00	3650.00	3650.00	3632.00	3572.00	3572.00
22.00	441.00	3970.00	3970.00	3784.00	3725.00	3634.00	3634.00
23.00	461.00	3970.00	3970.00	3856.00	3750.00	3620.00	3620.00
24.00	481.00	4042.00	4042.00	3859.00	3756.00	3602.00	3602.00
25.00	501.00	3982.00	3982.00	3819.00	3700.00	3547.00	3547.00
26.00	521.00	4000.00	4000.00	3840.00	3686.00	3509.00	3509.00
27.00	541.00	4000.00	4000.00	3840.00	3672.00	3486.00	3486.00
28.00	561.00	3945.00	3945.00	3796.00	3642.00	3442.00	3442.00
29.00	581.00	3905.00	3905.00	3763.00	3612.00	3397.00	3397.00
30.00	601.00	3837.00	3837.00	3735.00	3542.00	3327.00	3327.00
31.00	621.00	3752.00	3752.00	3699.00	3451.00	3240.00	3240.00
32.00	641.00	3717.00	3717.00	3662.00	3385.00	3157.00	3157.00
33.00	661.00	3635.00	3635.00	3582.00	3309.00	3105.00	3105.00
34.00	681.00	3726.00	3726.00	3691.00	3268.00	3100.00	3100.00
35.00	701.00	3720.00	3720.00	3542.00	3231.00	3079.00	3079.00
36.00	721.00	3837.00	3837.00	3560.00	3247.00	3119.00	3119.00

37.00	741.00	3917.00	3917.00	3608.00	3266.00	3140.00	3140.00
38.00	761.00	3770.00	3770.00	3693.00	3244.00	3147.00	3147.00
39.00	781.00	3797.00	3797.00	3724.00	3338.00	3266.00	3266.00
40.00	801.00	3813.00	3813.00	3703.00	3518.00	3393.00	3393.00
41.00	821.00	3693.00	3693.00	3629.00	3587.00	3410.00	3410.00
42.00	841.00	3669.00	3669.00	3580.00	3449.00	3367.00	3367.00
43.00	861.00	3605.00	3605.00	3467.00	3407.00	3336.00	3336.00
44.00	881.00	3502.00	3502.00	3421.00	3357.00	3280.00	3280.00
45.00	901.00	3378.00	3378.00	3315.00	3255.00	3207.00	3207.00
46.00	921.00	3366.00	3366.00	3297.00	3297.00	3175.00	3175.00
47.00	941.00	3436.00	3436.00	3436.00	3366.00	3287.00	3287.00
48.00	961.00	3401.00	3401.00	3401.00	3295.00	3236.00	3236.00
49.00	981.00	3328.00	3328.00	3328.00	3250.00	3175.00	3175.00
50.00	1001.00	3269.00	3269.00	3269.00	3210.00	3136.00	3136.00
51.00	1021.00	3174.00	3174.00	3174.00	3125.00	3069.00	3069.00
52.00	1041.00	3129.00	3129.00	3129.00	3091.00	3023.00	3023.00
53.00	1061.00	3271.00	3271.00	3271.00	3194.00	3194.00	3194.00
54.00	1081.00	3594.00	3594.00	3594.00	3336.00	3336.00	3336.00
55.00	1101.00	3741.00	3741.00	3741.00	3535.00	3535.00	3535.00
56.00	1121.00	4000.00	4000.00	4000.00	3721.00	3657.00	3657.00
57.00	1141.00	4264.00	4264.00	4264.00	3956.00	3888.00	3888.00
58.00	1161.00	4369.00	4369.00	4369.00	4205.00	4040.00	4040.00
59.00	1181.00	4456.00	4456.00	4456.00	4386.00	4178.00	4178.00
60.00	1201.00	4464.00	4464.00	4464.00	4407.00	4274.00	4274.00
61.00	1221.00	4460.00	4460.00	4460.00	4404.00	4300.00	4300.00
62.00	1241.00	4456.00	4456.00	4456.00	4401.00	4323.00	4323.00
63.00	1261.00	4452.00	4452.00	4452.00	4400.00	4346.00	4346.00
64.00	1281.00	4459.00	4459.00	4459.00	4386.00	4328.00	4328.00
65.00	1301.00	4402.00	4402.00	4402.00	4345.00	4285.00	4285.00
66.00	1321.00	4381.00	4381.00	4381.00	4289.00	4255.00	4255.00
67.00	1341.00	4447.00	4447.00	4447.00	4322.00	4322.00	4322.00
68.00	1361.00	4423.00	4423.00	4423.00	4249.00	4249.00	4249.00
69.00	1381.00	4336.00	4336.00	4336.00	4219.00	4142.00	4142.00
70.00	1401.00	4390.00	4390.00	4390.00	4285.00	4172.00	4172.00
71.00	1421.00	4554.00	4554.00	4554.00	4418.00	4241.00	4241.00
72.00	1441.00	4708.00	4708.00	4708.00	4535.00	4385.00	4385.00
73.00	1461.00	4386.00	4386.00	4386.00	4386.00	4186.00	4186.00
74.00	1481.00	4098.00	4098.00	4098.00	4041.00	3857.00	3857.00
75.00	1501.00	4046.00	4046.00	4046.00	3988.00	3820.00	3820.00
76.00	1521.00	3835.00	3835.00	3643.00	3643.00	3562.00	3562.00
77.00	1541.00	3725.00	3725.00	3550.00	3514.00	3429.00	3429.00
78.00	1561.00	3706.00	3706.00	3500.00	3415.00	3351.00	3351.00
79.00	1581.00	3735.00	3735.00	3551.00	3475.00	3400.00	3400.00
80.00	1601.00	3772.00	3772.00	3548.00	3500.00	3418.00	3418.00
81.00	1621.00	3782.00	3782.00	3585.00	3551.00	3471.00	3471.00

82.00	1641.00	3825.00	3825.00	3620.00	3584.00	3504.00	3504.00
83.00	1661.00	3901.00	3901.00	3712.00	3617.00	3534.00	3534.00
84.00	1681.00	3914.00	3914.00	3762.00	3627.00	3551.00	3551.00
85.00	1701.00	3937.00	3937.00	3789.00	3727.00	3570.00	3570.00
86.00	1721.00	3958.00	3958.00	3810.00	3810.00	3575.00	3575.00
87.00	1741.00	3742.00	3742.00	3684.00	3684.00	3566.00	3566.00
88.00	1761.00	3755.00	3755.00	3616.00	3361.00	3361.00	3361.00
89.00	1781.00	3628.00	3628.00	3567.00	3128.00	3079.00	3079.00
90.00	1801.00	3591.00	3591.00	3545.00	3077.00	2954.00	2954.00
91.00	1821.00	3668.00	3668.00	3528.00	3120.00	2985.00	2985.00
92.00	1841.00	3628.00	3628.00	3428.00	3100.00	2967.00	2967.00
93.00	1861.00	3518.00	3518.00	3429.00	3111.00	2975.00	2975.00
94.00	1881.00	3169.00	3169.00	3134.00	3067.00	2942.00	2942.00
95.00	1901.00	3335.00	3335.00	3050.00	2937.00	2828.00	2828.00
96.00	1921.00	3512.00	3512.00	3271.00	3000.00	2875.00	2875.00
97.00	1941.00	3431.00	3431.00	3345.00	3006.00	2900.00	2900.00
98.00	1961.00	3344.00	3344.00	3255.00	3019.00	2908.00	2908.00
99.00	1981.00	3368.00	3368.00	3303.00	2911.00	2869.00	2869.00
100.00	2001.00	3481.00	3389.00	3389.00	2982.00	3945.00	2854.00
101.00	2021.00	3531.00	3451.00	3451.00	3106.00	3048.00	2987.00
102.00	2041.00	3654.00	3515.00	3515.00	3193.00	3113.00	3006.00
103.00	2061.00	3862.00	3571.00	3571.00	3257.00	3138.00	3014.00
104.00	2081.00	3863.00	3648.00	3648.00	3286.00	3150.00	3019.00
105.00	2101.00	3868.00	3680.00	3680.00	3258.00	3161.00	3023.00
106.00	2121.00	4035.00	3735.00	3735.00	3360.00	3187.00	3025.00
107.00	2141.00	4300.00	3812.00	3812.00	3343.00	3194.00	3025.00
108.00	2161.00	4413.00	3852.00	3798.00	3399.00	3214.00	3027.00
109.00	2181.00	4444.00	3936.00	3864.00	3437.00	3228.00	3028.00
110.00	2201.00	4419.00	3982.00	3926.00	3442.00	3236.00	3028.00
111.00	2221.00	4405.00	4074.00	3977.00	3447.00	3243.00	3027.00
112.00	2241.00	4400.00	4077.00	3964.00	3461.00	3243.00	3027.00
113.00	2261.00	4415.00	4125.00	4001.00	3421.00	3241.00	3026.00
114.00	2281.00	4382.00	4154.00	4009.00	3465.00	3245.00	3025.00
115.00	2301.00	4342.00	4157.00	3990.00	3523.00	3249.00	3024.00
116.00	2321.00	4376.00	4146.00	4006.00	3577.00	3250.00	3022.00
117.00	2341.00	4306.00	4166.00	3987.00	3570.00	3242.00	3020.00
118.00	2361.00	4358.00	4154.00	4019.00	3600.00	3245.00	3019.00
119.00	2381.00	4477.00	4178.00	3964.00	3610.00	3244.00	3016.00
120.00	2401.00	4554.00	4193.00	3964.00	3606.00	3225.00	3009.00
121.00	2421.00	4528.00	4169.00	3953.00	3557.00	3216.00	3003.00
122.00	2441.00	4455.00	4148.00	3913.00	3503.00	3201.00	3000.00
123.00	2461.00	4343.00	4154.00	3868.00	3444.00	3178.00	2981.00
124.00	2481.00	4131.00	4085.00	3823.00	3457.00	3165.00	2969.00
125.00	2501.00	3969.00	3969.00	3791.00	3417.00	3135.00	2959.00
126.00	2521.00	3779.00	3779.00	3754.00	3407.00	3108.00	2940.00

127.00	2541.00	3650.00	3650.00	3650.00	3318.00	3063.00	2923.00
128.00	2561.00	3658.00	3658.00	3637.00	3262.00	3031.00	2902.00
129.00	2581.00	3718.00	3718.00	3645.00	3311.00	3013.00	2875.00
130.00	2601.00	3915.00	3860.00	3680.00	3323.00	2998.00	2850.00
131.00	2621.00	3926.00	3836.00	3674.00	3361.00	2989.00	2827.00
132.00	2641.00	4104.00	3932.00	3698.00	3348.00	2863.00	2805.00
133.00	2661.00	4143.00	3987.00	3727.00	3341.00	2939.00	2776.00
134.00	2681.00	4042.00	3979.00	3693.00	3291.00	2915.00	2747.00
135.00	2701.00	4116.00	3974.00	3685.00	3327.00	2892.00	2721.00
136.00	2721.00	4197.00	3982.00	3650.00	3324.00	2849.00	2689.00

Line 24, depth-converted data

Calculated Depth (km)						(km)
Basement	Layer 1	Layer 2	Layer 3	Layer 4	Seafloor	Distance x
3.69	3.69	3.33	3.19	2.93	2.93	0.00
3.71	3.71	3.40	3.31	2.93	2.93	1.00
3.30	3.30	3.33	3.30	2.93	2.93	2.00
3.32	3.32	3.13	3.07	2.93	2.93	3.00
3.26	3.26	3.14	3.04	2.91	2.91	4.00
3.38	3.38	3.17	2.98	2.86	2.86	5.00
3.08	3.08	3.04	2.82	2.72	2.72	6.00
2.65	2.65	2.65	2.65	2.58	2.58	7.00
2.45	2.45	2.45	2.30	2.30	2.30	8.00
2.53	2.53	2.53	2.34	2.29	2.29	9.00
2.59	2.59	2.59	2.49	2.36	2.36	10.00
2.59	2.59	2.59	2.53	2.40	2.40	11.00
2.61	2.61	2.61	2.52	2.47	2.47	12.00
2.62	2.62	2.62	2.54	2.47	2.47	13.00
2.72	2.72	2.72	2.62	2.57	2.57	14.00
2.78	2.78	2.78	2.71	2.62	2.62	15.00
2.88	2.88	2.88	2.77	2.61	2.61	16.00
2.79	2.79	2.79	2.61	2.55	2.55	17.00
2.65	2.65	2.65	2.58	2.46	2.46	18.00
2.65	2.65	2.65	2.61	2.53	2.53	19.00
2.71	2.71	2.71	2.63	2.56	2.56	20.00
2.76	2.76	2.76	2.74	2.68	2.68	21.00
3.13	3.13	2.88	2.81	2.73	2.73	22.00
3.11	3.11	2.96	2.84	2.72	2.72	23.00
3.21	3.21	2.96	2.85	2.70	2.70	24.00

3.16	3.16	2.94	2.81	2.66	2.66	25.00
3.19	3.19	2.97	2.80	2.63	2.63	26.00
3.19	3.19	2.98	2.79	2.61	2.61	27.00
3.14	3.14	2.94	2.77	2.58	2.58	28.00
3.11	3.11	2.92	2.75	2.55	2.55	29.00
3.05	3.05	2.91	2.70	2.50	2.50	30.00
2.97	2.97	2.90	2.63	2.43	2.43	31.00
2.96	2.96	2.89	2.58	2.37	2.37	32.00
2.89	2.89	2.82	2.52	2.33	2.33	33.00
3.00	3.00	2.95	2.48	2.33	2.33	34.00
3.04	3.04	2.80	2.45	2.31	2.31	35.00
3.18	3.18	2.81	2.46	2.34	2.34	36.00
3.27	3.27	2.85	2.47	2.36	2.36	37.00
3.05	3.05	2.95	2.45	2.36	2.36	38.00
3.04	3.04	2.94	2.52	2.45	2.45	39.00
3.02	3.02	2.87	2.66	2.54	2.54	40.00
2.86	2.86	2.77	2.73	2.56	2.56	41.00
2.87	2.87	2.75	2.60	2.53	2.53	42.00
2.82	2.82	2.64	2.57	2.50	2.50	43.00
2.71	2.71	2.60	2.53	2.46	2.46	44.00
2.60	2.60	2.52	2.45	2.41	2.41	45.00
2.59	2.59	2.50	2.50	2.38	2.38	46.00
2.62	2.62	2.62	2.54	2.47	2.47	47.00
2.60	2.60	2.60	2.48	2.43	2.43	48.00
2.54	2.54	2.54	2.45	2.38	2.38	49.00
2.49	2.49	2.49	2.42	2.35	2.35	50.00
2.41	2.41	2.41	2.35	2.30	2.30	51.00
2.37	2.37	2.37	2.33	2.27	2.27	52.00
2.48	2.48	2.48	2.40	2.40	2.40	53.00
2.79	2.79	2.79	2.50	2.50	2.50	54.00
2.88	2.88	2.88	2.65	2.65	2.65	55.00
3.11	3.11	3.11	2.80	2.74	2.74	56.00
3.32	3.32	3.32	2.98	2.92	2.92	57.00
3.37	3.37	3.37	3.19	3.03	3.03	58.00
3.41	3.41	3.41	3.33	3.13	3.13	59.00
3.39	3.39	3.39	3.33	3.21	3.21	60.00
3.39	3.39	3.39	3.32	3.23	3.23	61.00
3.38	3.38	3.38	3.32	3.24	3.24	62.00
3.37	3.37	3.37	3.31	3.26	3.26	63.00
3.38	3.38	3.38	3.30	3.25	3.25	64.00
3.33	3.33	3.33	3.27	3.21	3.21	65.00
3.32	3.32	3.32	3.22	3.19	3.19	66.00
3.38	3.38	3.38	3.24	3.24	3.24	67.00
3.38	3.38	3.38	3.19	3.19	3.19	68.00
3.31	3.31	3.31	3.18	3.11	3.11	69.00

3.35	3.35	3.35	3.24	3.13	3.13	70.00
3.50	3.50	3.50	3.35	3.18	3.18	71.00
3.62	3.62	3.62	3.43	3.29	3.29	72.00
3.33	3.33	3.33	3.33	3.14	3.14	73.00
3.13	3.13	3.13	3.07	2.89	2.89	74.00
3.09	3.09	3.09	3.02	2.87	2.87	75.00
3.01	3.01	2.75	2.75	2.67	2.67	76.00
2.93	2.93	2.69	2.65	2.57	2.57	77.00
2.95	2.95	2.67	2.57	2.51	2.51	78.00
2.95	2.95	2.70	2.62	2.55	2.55	79.00
3.00	3.00	2.69	2.64	2.56	2.56	80.00
2.98	2.98	2.72	2.68	2.60	2.60	81.00
3.02	3.02	2.74	2.70	2.63	2.63	82.00
3.09	3.09	2.83	2.73	2.65	2.65	83.00
3.09	3.09	2.88	2.74	2.66	2.66	84.00
3.09	3.09	2.89	2.83	2.68	2.68	85.00
3.10	3.10	2.90	2.90	2.68	2.68	86.00
2.86	2.86	2.79	2.79	2.67	2.67	87.00
2.99	2.99	2.80	2.52	2.52	2.52	88.00
2.92	2.92	2.84	2.36	2.31	2.31	89.00
2.91	2.91	2.85	2.33	2.22	2.22	90.00
3.00	3.00	2.82	2.37	2.24	2.24	91.00
2.98	2.98	2.71	2.35	2.23	2.23	92.00
2.83	2.83	2.71	2.36	2.23	2.23	93.00
2.45	2.45	2.40	2.33	2.21	2.21	94.00
2.73	2.73	2.35	2.22	2.12	2.12	95.00
2.90	2.90	2.57	2.28	2.16	2.16	96.00
2.76	2.76	2.65	2.28	2.18	2.18	97.00
2.67	2.67	2.55	2.29	2.18	2.18	98.00
2.71	2.71	2.62	2.19	2.15	2.15	99.00
2.74	2.60	2.60	2.15	3.07	2.14	100.00
2.85	2.73	2.73	2.35	2.29	2.24	101.00
2.98	2.78	2.78	2.42	2.35	2.25	102.00
3.26	2.82	2.82	2.48	2.37	2.26	103.00
3.23	2.90	2.90	2.50	2.38	2.26	104.00
3.22	2.94	2.94	2.48	2.38	2.27	105.00
3.43	2.98	2.98	2.57	2.41	2.27	106.00
3.80	3.07	3.07	2.55	2.41	2.27	107.00
3.96	3.12	3.04	2.60	2.43	2.27	108.00
3.97	3.21	3.11	2.64	2.44	2.27	109.00
3.91	3.25	3.18	2.64	2.45	2.27	110.00
3.86	3.36	3.23	2.65	2.45	2.27	111.00
3.85	3.37	3.21	2.66	2.45	2.27	112.00
3.86	3.43	3.26	2.62	2.45	2.27	113.00
3.80	3.46	3.26	2.66	2.46	2.27	114.00

3.74	3.46	3.23	2.72	2.46	2.27	115.00
3.78	3.43	3.24	2.77	2.46	2.27	116.00
3.68	3.47	3.22	2.77	2.45	2.27	117.00
3.74	3.44	3.25	2.79	2.46	2.26	118.00
3.93	3.48	3.19	2.80	2.46	2.26	119.00
4.05	3.51	3.20	2.80	2.44	2.26	120.00
4.02	3.48	3.19	2.76	2.43	2.25	121.00
3.94	3.48	3.16	2.71	2.42	2.25	122.00
3.79	3.51	3.12	2.66	2.40	2.24	123.00
3.50	3.43	3.07	2.67	2.39	2.23	124.00
3.29	3.29	3.05	2.64	2.37	2.22	125.00
3.05	3.05	3.01	2.63	2.35	2.21	126.00
2.92	2.92	2.92	2.55	2.31	2.19	127.00
2.95	2.95	2.92	2.51	2.29	2.18	128.00
3.02	3.02	2.92	2.56	2.27	2.16	129.00
3.29	3.21	2.96	2.57	2.26	2.14	130.00
3.31	3.17	2.96	2.61	2.26	2.12	131.00
3.57	3.31	3.00	2.61	2.15	2.10	132.00
3.61	3.38	3.03	2.60	2.22	2.08	133.00
3.48	3.39	3.00	2.56	2.20	2.06	134.00
3.60	3.38	2.99	2.60	2.19	2.04	135.00
3.73	3.41	2.96	2.60	2.15	2.02	136.00